A CALIBRATION NEUTRON MONITOR FOR LONG-TERM COSMIC RAY MODULATION STUDIES

H. KRÜGER M.Sc.

Thesis accepted for the degree Doctor of Philosophy
in Physics
at the North-West University

Promotor: Prof. H. Moraal

January 2006
Potchefstroom Campus

ABSTRACT

The propagation of high-energy cosmic rays is influenced by the time-varying heliospheric magnetic field embedded in the solar wind, and by the geomagnetic field. To penetrate through this geomagnetic field, they must have a rigidity that exceeds the geomagnetic cutoff rigidity for a given position on the earth. In the atmosphere, the primary cosmic rays interact with atmospheric nuclei, to form a cascade of secondary particles. Neutron monitors record these secondary cosmic rays, mainly the neutrons, with energies about a decade higher than detected by most spacecraft.

Since neutron monitors are integral detectors, each with its own detection efficiency, energy spectra cannot readily be derived from their observations. One way to circumvent this is by conducting latitudinal surveys with mobile neutron monitors. Another way is to use the worldwide stationary neutron monitor network, but then the counting rates of these monitors must be normalised sufficiently accurate against one another. For this reason two portable calibration neutron monitors were built at the Potchefstroom campus of the North-West University and completed in 2002.

To achieve sufficient calibration accuracy, several properties of the calibrator are investigated in this work. Effects such as atmospheric pressure variations, diurnal variations, short-term scintillations, and multiplicity, contribute to the fluctuations of the counting rate of a neutron monitor. Due to these effects, the coefficient of variation of the calibrator is determined to be ~40% larger than the Poisson deviation. The energy response of the calibrator over the cutoff rigidity interval from the poles to the equator is investigated, with the result that it is almost 4% larger than that of a standard 3NM64 neutron monitor. It is also determined that not only the calibrator, but also the stationary NM64 and IGY neutron monitors, have fairly large instrumental temperature sensitivity, which must be accounted for in calibration procedures. Furthermore, the calibrator has a large sensitivity to the type of surface beneath it, influencing its counting rate by as much as 5%. This investigation is incomplete and requires further experimentation before the calibration of the stationary neutron monitors can start.

When calibrations of a significant number of the worldwide neutron monitors are done, their intensity spectra as derived from differential response functions, will provide experimental data for modulation studies at rigidities above 1 GV.

Keywords: cosmic rays, cutoff rigidity, neutron monitor, differential response function.

OPSOMMING

'n Kalibrasie-neutronmonitor vir langtermyn modulasiestudies van kosmiese strale

Die voortplanting van hoogenergieke kosmiese strale word deur die tydsafhanklike heliosferiese magneetveld in die sonwind, sowel as die geomagnetiese veld, beïnvloed. Om hierdie geomagnetiese veld binne te dring, moet hulle 'n groter styfheid as die geomagnetiese afsnystyfheid vir 'n gegewe posisie op die aarde hê. Wanneer hulle die atmosfeer binnedring, tree hierdie primêre kosmiese strale in wisselwerking met atmosferiese kerne, om 'n kaskade van sekondêre deeltjies te vorm. Neutronmonitors registreer hierdie sekondêre kosmiese strale, veral die neutrone, met energieë wat ongeveer 'n dekade hoër is as wat deur meeste ruimtetuie waargeneem kan word.

Aangesien neutronmonitors integrale detektore is, elkeen met sy eie waarnemings-doeltreffendheid, kan energiespektra nie geredelik afgelei word nie. Een manier om dit te omseil is deur breedtegraadsreise met 'n mobiele neutronmonitor te onderneem. 'n Ander manier is deur van die wêreldwye netwerk van stasionêre neutronmonitors gebruik te maak, maar dan moet die teltempo's van hierdie monitors akkuraat teenoor mekaar genormaliseer word. Hiervoor is twee draagbare kalibrasie-neutronmonitors by die Potchefstroomse kampus van die Noordwes-Universiteit gebou en in 2002 voltooi.

Verskeie eienskappe van die kalibrator word in hierdie werk ondersoek, om sodoende voldoende kalibrasie-akkuraatheid te verkry. Effekte soos atmosferiese drukvariasies, daaglikse variasies, korttermyn flitsings en multiplisiteite, dra tot die fluktuasies van die neutronmonitor se teltempo by. As gevolg van hierdie effekte, word gevind dat die koëffisiënt van variasie ~40% groter as die Poisson-afwyking is. Die energie-respons van die kalibrator oor die afsnystyfheidsgebied van die pole tot die ewenaar, word ook ondersoek en dit is byna 4% groter as dié van 'n standaard 3NM64. Daar word ook bepaal dat nie net die kalibreerder nie, maar ook die stasionêre NM64 en IGJ neutronmonitors, 'n redelike groot instrumentele temperatuursensitiwiteit het, wat met die kalibrasieproses in ag geneem moet word. Verder blyk dit dat die kalibreerder 'n groot sensitiwiteit vir die tipe oppervlak onder hom het, wat sy teltempo met soveel as 5% beïnvloed. Hierdie probleem verg verdere ondersoek, voordat met die kalibrasie van die stasionêre neutronmonitors begin kan word.

Wanneer kalibrasies van 'n betekenisvolle aantal van die wêreldwye neutronmonitors gedoen is, sal hulle intensiteitspektra, afgelei van die differensiële responsfunksie, eksperimentele data vir modulasiestudies by afsnystyfhede groter as 1 GV verskaf.

Sleutelwoorde: kosmiese strale, afsnystyfheid, neutronmonitor, differensiële responsfunksie.

TABLE OF CONTENTS

Chapter 1
Introduction

Cosmic rays are high-energy (kinetic energy > 1MeV) atomic nuclei produced mainly in the galaxy, and transported through the heliosphere to reach the earth. The propagation of these particles is influenced by the time-varying magnetic field embedded in the solar wind, and by the geomagnetic field. They must have a rigidity (momentum per unit charge) that exceeds the so-called geomagnetic cutoff rigidity for a given position. After penetrating the geomagnetic field, these primary cosmic rays interact with the nuclei in the atmosphere, to form a cascade of secondary particles.

In order to record these secondary cosmic rays, mainly the neutrons, J.A. Simpson started to develop the neutron monitor in 1948, and the first one was installed in 1951. Neutron monitors proliferated to a network of more than 100 by the end of the 1960s. Presently there are still approximately 50 neutron monitors operating.

The year 1957 saw the beginning of space experiments. These experiments have the twofold advantage above neutron monitor measurements that the primary cosmic rays are detected directly, and that they measure the intensity at much lower energies, where variations due to solar/heliospheric modulation are much larger. A third advantage is that their detectors measure intensities in pre-determined energy intervals, from which cosmic ray energy spectra can be constructed. On the contrary, neutron monitors are integral instruments, because they record all the particles above a specific rigidity. In addition, each neutron monitor has a different design and efficiency, which makes it impossible to reconstruct such spectra from integral measurements.

Due to these distinct advantages, space experiments to study the solar/heliospheric modulation of the cosmic ray intensity have become preferential to neutron monitor experiments.

On the other hand, neutron monitors have advantages, such as high counting rates leading to statistical accuracy. They also detect particles with energies about a decade higher than possible with most spacecraft, and they can therefore measure small effects in detail.

In view of such considerations, an ISSI workshop was held in 1999, as compiled by Bieber *et al.* (2000), at which the contributions of the neutron monitor network and its future relevance were discussed. Two other distinct advantages of the neutron monitor network is that it provides a long-term, continuous and stable baseline of the cosmic ray intensity, and that the annual maintenance of the network only amounts to a few percent of the cost of a single space mission. It was also mentioned at this workshop (Moraal *et al.*, 2000) that the concept of Spaceship Earth is complementary to space experiments to measure the anisotropic transport of solar cosmic rays in so-called ground level enhancements (GLEs). This Spaceship Earth consists of a network of neutron monitors with narrow cones of acceptance, that are placed at high latitudes in order to provide a directional view of cosmic ray intensity around the equator.

At this workshop the idea was also raised that with modern technology it should be practically possible to derive energy spectra from neutron monitors on a continuous basis.

There are two ways to derive spectra from neutron monitor data. The existing one is by conducting latitudinal surveys, where a neutron monitor is transported through a range of cutoff rigidities. The drawback here is that these surveys do not take place on a continuous and regularly base.

Spectra can also be derived, in principle, from the counting rates of the worldwide neutron monitor network. However, in practice, this is not possible, because the efficiency of each monitor is different and thus the counting rates cannot be compared. Therefore, to investigate the energy dependence of the modulation of cosmic rays requires that the counting rates must be normalised sufficiently accurate against one another. From these considerations, the need for a calibration neutron monitor, an instrument that can be transported to stationary neutron monitors for intercalibration, was identified.

Two such calibration neutron monitors were built at the Potchefstroom campus of the North-West University, and completed in September 2002. These calibrators are much smaller in size than stationary monitors and therefore easy to transport. They are designed to provide an intercalibration between the 50-odd neutron monitors around the world, in order to calculate energy/rigidity spectra from them.

To achieve sufficient calibrating accuracy, the following properties of the calibrator must be known:

1) its energy response relative to that of stationary monitors;
2) its temperature sensitivity;
3) its environmental sensitivity.

In view of the development of such a calibrator, this thesis consists of two parts, viz. a general background of neutron monitor measurements of the cosmic radiation, and then the design of the calibrator and experiments that have so far been conducted to investigate its properties.

Chapter 2 gives an overview of the basic features of the transport of cosmic rays through the galaxy, the heliosphere and the atmosphere. Solar modulation, solar energetic particles, and the equation of the transport of cosmic rays in the heliosphere, are briefly described.

The geomagnetic field influences the trajectories of the cosmic rays. Chapter 3 gives an overview of the mathematical model used to describe the trajectories of cosmic rays in this field, and the calculations of the so-called cutoff rigidities.

Chapter 4 describes the development and design of neutron monitors, focusing on the detection efficiency of the two main types, and as background material for the design of the calibrator.

The relation between the primary intensity spectra and the neutron monitor response functions is discussed in Chapter 5. Latitudinal surveys have been conducted in order to study the neutron monitor differential response function as derived from latitudinal dependence. The obvious drawback is that these differential response functions are not continuously available. This leads to the need of a calibrator for spectral studies.

The subsequent chapters are about the calibrator and its performance tests, starting with Chapter 6, which is a summary of the design and specifications of the two calibrators.

One of the calibrators was sent together with the US / Australian 3NM64 on three sea voyages between the USA and Antarctica. The purpose was to investigate the energy response of the calibrator by comparing the variation in counting rate of the two types of neutron monitors as a function of cutoff rigidity. These results were compared with a theoretical simulation, done with a so-called Monte Carlo technique. These surveys and their results are described in Chapter 7.

Chapter 8 describes the effects that cause fluctuations in the counting rate of neutron monitors. Based on this, reliability considerations for calibration were investigated.

The second calibrator was taken to Sanae, Antarctica, to calibrate the Sanae neutron monitor. A larger than expected instrumental temperature effect on the calibration monitor was found during this experiment. Consequently, more extensive temperature tests were done, also on stationary neutron monitors. These experiments are described in Chapter 9.

In addition, the sensitivity of the calibrator to its environment, in particular to different ground surfaces, was investigated and discussed in Chapter 10. It seems that this surface effect may become the determined factor for the success of the calibration.

In the last chapter, Chapter 11, conclusions and recommendations for the calibration procedure are given.

Chapter 2
Transport of Cosmic Rays

2.1 Introduction

Cosmic rays are high-energy particles from outer space (and sometimes from the sun) that can be detected by spacecraft and recorded by detectors on the earth. They are usually charged particles, but neutral particles like neutrons, neutrinos and high-energetic photons are also considered to be cosmic rays.

These particles are produced in the galaxy by processes that are yet not fully understood. The propagation of these particles in the heliosphere (or interplanetary space) is influenced by the magnetic fields in the solar wind and by the magnetosphere of the earth. The properties of these magnetic fields, as well as changes in these fields, can be investigated by recording the fluctuations in cosmic ray intensities. In this chapter the general aspects of transport of cosmic rays will be described.

Victor Hess, an Austrian physicist, discovered cosmic rays when he performed a balloon flight with two ionisation chambers in 1912. He found that the ionisation rate initially decreased up to about 1500 m, and then increased rapidly. At 5000 m it was more than twice the surface rate. He explained the results by postulating that very high-speed penetrating particles from above enter the atmosphere and cause ionisation. Pomerantz (1971) pointed out that Werner Kolhörster, a German physicist, had confirmed the existence of cosmic rays with further flights up to a height of 9.3 km in 1914.

Jacob Clay, a Dutch physicist, observed a latitudinal effect in the intensity of cosmic rays on different voyages between Genoa and Java, and published his results in 1927 and 1928, according to Friedlander (2000). This latitudinal effect indicated a lower intensity of cosmic rays near the equator, where the horizontal component of the geomagnetic field is stronger. This result means that the majority of the primary particles are charged before entering the earth's magnetic field. Arthur Compton confirmed and extended the results of Clay with extended worldwide surveys between 1930 and 1933. Kallenrode (2000) stated that when Størmer's calculations of particle trajectories in the geomagnetic field became available in 1930, it was understood that the latitudinal effect was due to shielding by the geomagnetic field.

According to Schlaepfer (2003), Bruno Rossi showed in 1930 that there should be an east-west effect if the cosmic rays are predominantly of one charge. In 1933 two American groups, Thomas Johnson of the Bartol Research Foundation, and Luis Alvarez and Arthur Compton of the University of Chicago, observed this effect independently, showing that the cosmic radiation is predominantly positively charged. Many studies and surveys followed.

Elements present in the cosmic radiation near the top of the atmosphere are mainly protons (± 93%), followed by helium nuclei (± 6%). The rest are heavier atomic nuclei up to iron (Fe) and electrons (~1%). Neutral cosmic rays, like γ- and X-rays, neutrinos and neutrons, also exist. This information was obtained from balloon and spacecraft observations.

2.2 Energy spectrum of cosmic rays

The majority of information about cosmic rays is extracted from the energy spectrum and its variations. The energy spectrum of cosmic rays recorded at earth is shown in Figure 2.1.

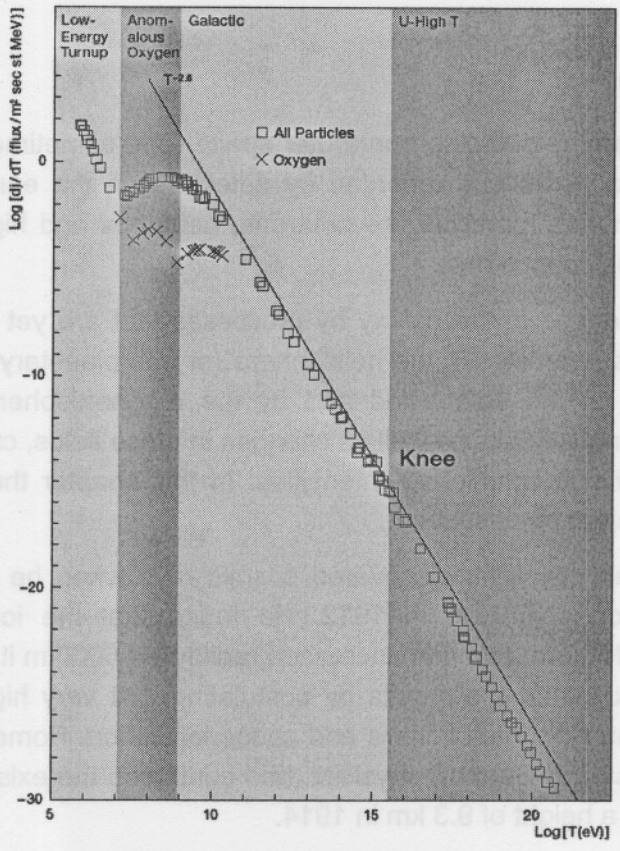

Figure 2.1: The energy spectrum of cosmic rays, measured at the earth. Adapted from Schlaepfer (2003).

This spectrum shows a power-law distribution of the form $T^{-2.65}$, from ~10^{10} eV to ~10^{15} eV. These particles are of galactic origin. There is a knee at ~10^{15} eV, so that at > 10^{15} eV the spectrum is softer, of the form $T^{-3.0}$. Particles with T > ~10^{17} eV are considered of extragalactic origin.

At energies < ~10^{10} eV the galactic particles are influenced by solar modulation (Section 2.4). The oxygen spectrum is also shown, which indicates the presence of so-called anomalous cosmic rays at 10^7 < T < 10^9 eV. These particles are partially ionised interstellar atoms accelerated at the solar wind termination shock. Below 10^7 eV there is a rise in the spectrum, due to particles of solar origin.

2.3 Propagation of cosmic rays

Schlaepfer (2003) stated that the elemental composition of cosmic rays provides information about the nature of the source, as well as on the propagation of cosmic rays in interstellar space. The variation of the charge and mass composition with energy can be related to the acceleration process and to particle transport in the galaxy. With improved measurements at

ultra-high energies it should be possible to determine whether these particles are of galactic or extragalactic origin.

Cosmic rays have to travel through the galaxy, the heliosphere, geomagnetic field, and through the atmosphere before they can possibly be recorded on earth. Each of these propagation media transforms the intensity of cosmic rays and will be described briefly.

A general background on these media and the propagation of cosmic rays therein, can be found in Hayakawa (1969), Pomerantz (1971), Dorman (1974), Wilson (1976), Friedlander (1989, 2000), Hargreaves (1992), Kallenrode (2000), and Schlickeiser (2002).

2.3.1 The galaxy

Our galaxy has the shape of a flat disk, consisting of 10^{11} stars, plus nebulae, dust and gas. The radius is ≈ 15 kpc and it is ≈ 1 kpc thick (1 pc = 3.1×10^{16} m = 3.26 light years). It rotates with respect to its centre of gravity with a period of about 2×10^8 years and forms a spiral structure, as shown in Figure 2.2.

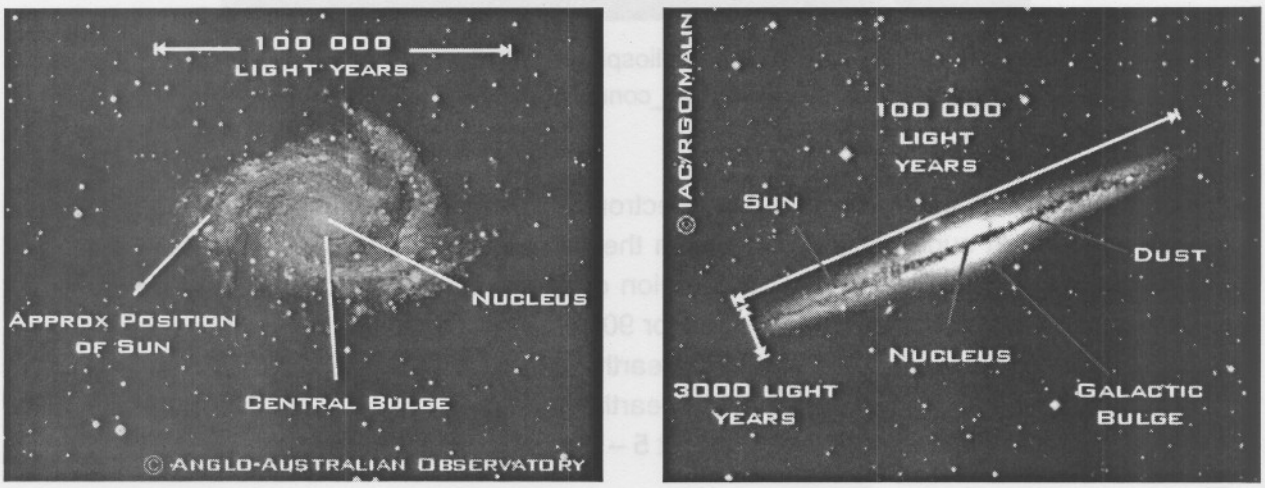

Figure 2.2: The galaxy from above (left) and from the side (right). From http://www.le.ac.uk/physics/faulkes/web/galaxies

The strength of the galactic magnetic field is ~10^{-10} T and is directed along the spiral arms. It is quite regular, with the field lines approximately parallel to the galactic plane.

The temperature and composition properties of the gas in the galaxy are similar to that of the solar corona. It is strongly ionised, and therefore has a high electric conductivity. This gives rise to the freezing-in of the galactic magnetic field in the plasma. Cosmic rays are guided by the galactic magnetic field and its irregularities.

It can be deduced from the gyration radius of the particles that the galactic magnetic field with its irregularities will significantly scatter cosmic ray particles of energies << 10^{17} eV/nucleon. Consequently, the intensity of these cosmic rays will become isotropic and the direction of the source cannot be determined from their arrival direction. Only high energetic particles, with energies > ~10^{19} eV, can possibly give some information about the direction of the source.

2.3.2 The heliosphere

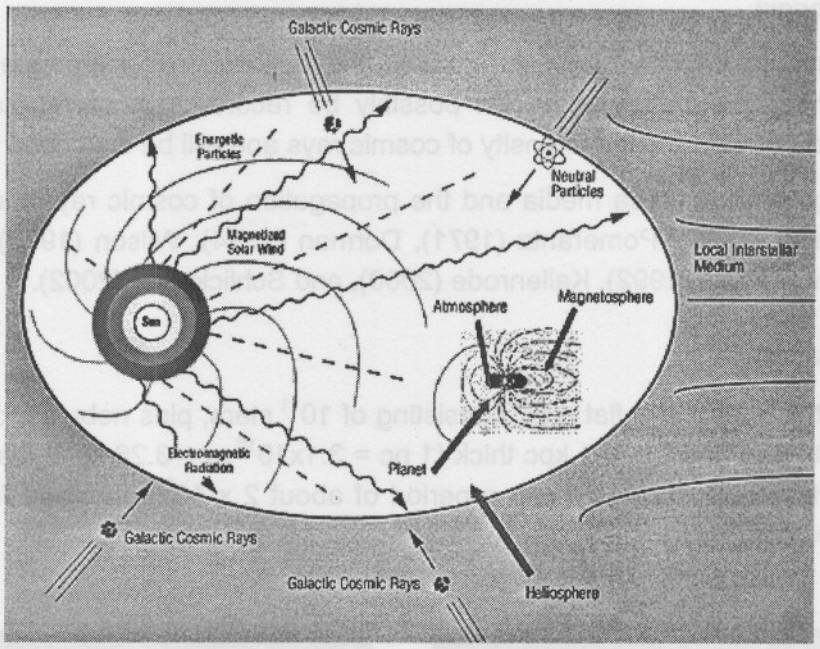

Figure 2.3: A schematic representation of the heliosphere, with the magnetosphere of the earth as an inset. From http://umbra.nascom.nasa.gov/solar_connections/domain.html.

A highly conducting, fully ionised, proton-electron gas plasma, called the solar wind, expands radially outward at supersonic velocity from the corona. This hydrodynamic solar wind was first introduced by Parker (1958a). The region of space influenced by the sun and its solar wind is called the heliosphere, and ranges for 90 – 150 AU (astronomical units, where 1 AU = average distance between the sun and the earth $\approx 1.49 \times 10^8$ km $\approx 5 \times 10^{-6}$ pc), as shown in Figure 2.3. The solar wind sweeps past the earth with a mean velocity of 400 – 500 km/s and a mean proton and electron density of about 5 – 7 particles/cm^3.

The supersonic velocity of the expanding solar wind terminates abruptly with a shock transition into the subsonic state, where the wind speed falls off as $1/r^2$. The spacecraft Voyager 1 reached this boundary between the interplanetary and interstellar regions at 94 AU on 16 December 2004 (Stone *et al.*, 2005).

The solar wind carries the solar magnetic field, rooted at the sun, radially outward into the heliosphere. Since the solar wind consists of fully ionised plasma, it has a high electric, as well as thermal conductivity, so that, according to Lenz's law, the plasma cannot move across the magnetic field lines. The magnetic field is frozen into this plasma and while the magnetic field moves away from the sun with the solar wind, it remains attached to the rotating sun, thus resulting that the field lines form the so-called Archimedean spiral, introduced by Parker (1958a), and it is therefore also called the Parker spiral field. This spiral field is shown in Figure 2.3.

Fisk (1996) introduced a more complex representation of the solar magnetic field, in which extensive excursions of heliospheric magnetic field lines with heliographic latitude are executed. Fisk *et al.* (1999) described this field in detail, where the excursions are caused by

the differential rotation of the photosphere and the consequently different non-radial expansion of the field lines near the sun.

Schlickeiser (2002) stated that there are smaller magnetic field irregularities generated by the turbulence and instabilities in the solar corona and heliosphere. The charged cosmic rays are strongly influenced by this magnetic field as they penetrate from outside into the heliosphere. Since the irregularities are transported outwards with the solar wind speed, the cosmic rays are also convected outwards.

When the radiant output of the sun is at a generally steady level, the sun is relatively calm and it is known as the *quiet sun*. The *active sun* is characterized by the appearance and disappearance of discrete sunspots and by the appearance of solar flares. These *active regions* on the solar surface have lifetimes that may range from one day to three months, or even almost a year. The occurrence of this *solar activity* distinguishes the active sun from the quiet sun, leading to *solar cycles*, with *solar minimum* and *solar maximum* periods, with the average length of a solar cycle of about 11 years, as shown in Figure 2.4. The period from 1755 to 1766 was chosen as solar cycle 1 (Gombosi, 1998). In 1976 solar cycle 21 started, with its maximum in 1979, and ended in 1986. Solar cycle 22 began in 1986, reaching its maximum in 1991, and ending in 1996. The present cycle started at solar minimum in 1996 and reached its maximum in 2001.

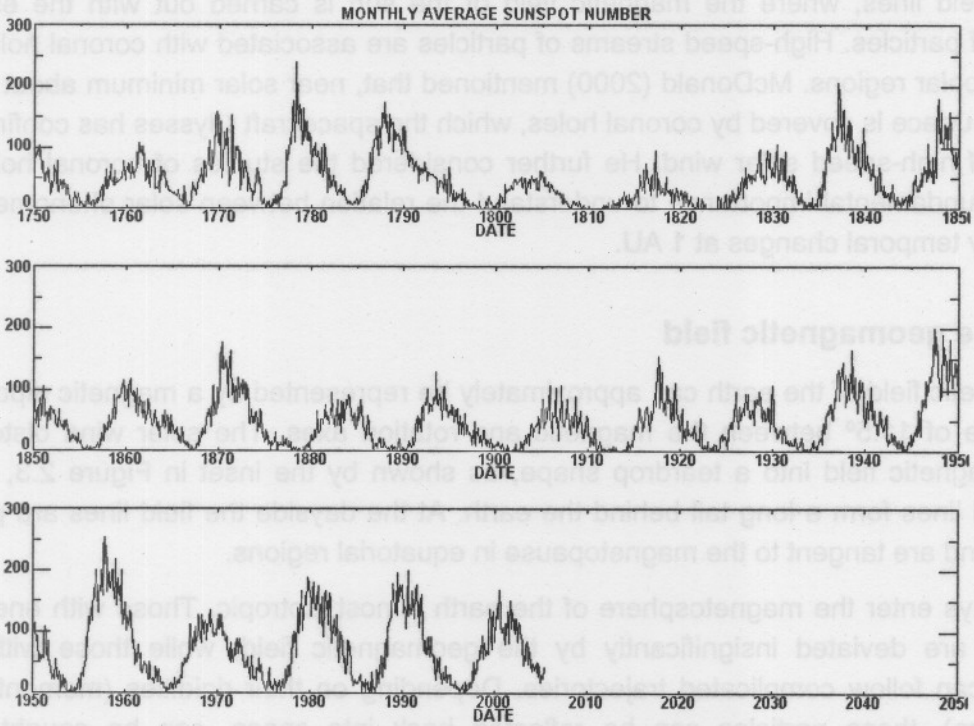

Fig 2.4: Sunspot numbers since 1750. The 11-year periodicity can be seen. From http://science.msfc.nasa.gov/ssl/pad/solar/images/zurich.gif.

Sunspots are dark regions that are 1000 – 1500°C cooler than the surrounding photosphere. Their sizes range from a few hundreds of kilometres to as large as 10^5 km. Strong magnetic fields up to 0.3 T may develop before the spot becomes visible, and may persist afterwards

(Gombosi, 1998). Sunspots rarely occur at latitudes above 40°. Spots in a new cycle (solar minimum) appear at the higher heliographic latitudes (25° – 30°) and the appearances drift toward the equator as solar maximum approaches. They often occur in pairs of opposite polarity. A thin current sheet divides the field in the northern and southern hemispheres of opposite signs. The polarity orientations in the polar regions of the two hemispheres are consistently opposite, and reverse in alternate 11-year cycles. This 11-year reversal of sunspot polarities leads to a 22-year solar magnetic cycle.

Solar flares are a source of solar cosmic rays. A solar flare is an explosive release of energy on the sun in regions of high magnetic fields, mainly in the form of electromagnetic radiation and energetic particles. Sometimes solar particles accelerate to such high energies (> 400 MeV) that neutron monitors can record them. The flare particles are recorded as a sharp increase in cosmic ray intensity, followed by a slower decrease, usually within 24 hours. Major solar flares occur unpredictably, but their frequency follows the sunspot cycle.

Parker (1961) showed that the sun produces blast waves. Such blast waves can also be caused by *coronal mass ejections* (CMEs) from the lower corona, when large amounts of plasmas ($10^{11} – 10^{14}$ kg) are ejected from the sun and compress the heliospheric magnetic field. Energetic blast waves and CMEs cause geomagnetic storms.

Coronal holes are regions of low-density cold plasma in comparison with the hot higher-density plasma of the corona, and of unipolar magnetic fields. Coronal holes are connected to open field lines, where the magnetic field of the sun is carried out with the escaping streams of particles. High-speed streams of particles are associated with coronal holes near the sun's polar regions. McDonald (2000) mentioned that, near solar minimum about 20% of the solar surface is covered by coronal holes, which the spacecraft Ulysses has confirmed as sources of high-speed solar wind. He further considered the studies of coronal holes and CMEs of fundamental importance to understand the relation between solar phenomena and cosmic ray temporal changes at 1 AU.

2.3.3 The geomagnetic field

The magnetic field of the earth can approximately be represented by a magnetic dipole, with a tilt angle of 11.5° between the magnetic and rotation axes. The solar wind distorts the earth's magnetic field into a teardrop shape, as shown by the inset in Figure 2.3, so that some field lines form a long tail behind the earth. At the dayside the field lines are pressed together and are tangent to the magnetopause in equatorial regions.

Cosmic rays enter the magnetosphere of the earth almost isotropic. Those with energies > ~10^{11} eV are deviated insignificantly by the geomagnetic field, while those with lower energies can follow complicated trajectories. Depending on their rigidities (momentum per unit charge), these particles can be reflected back into space, can be caught in the magnetosphere, or can penetrate into the atmosphere of the earth.

The geomagnetic field and the transport of particles in this field are described in more detail in Chapter 3.

2.3.4 The atmosphere

Cosmic rays that enter the atmosphere of the earth are called the primary cosmic rays. They reach the earth almost isotropic, because of their complicated transport and scattering in the galactic, heliospheric and geomagnetic fields. The earth is protected against cosmic radiation by the magnetic field and the atmosphere around the earth.

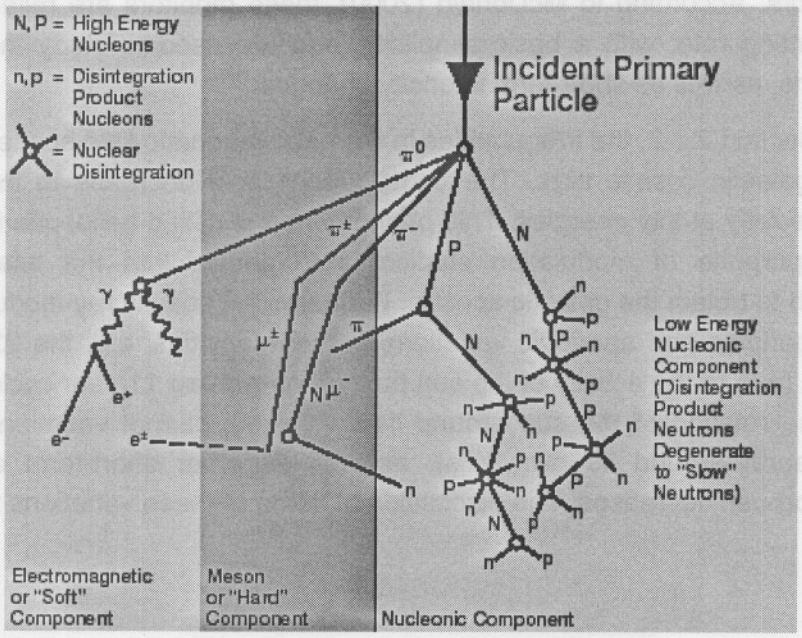

Figure 2.5: A schematic diagram of a cosmic ray cascade. Adapted from Schlaepfer (2003).

Primary cosmic rays, predominantly protons, penetrate the atmosphere and interact with its nuclei, mainly nitrogen and oxygen, producing secondary cosmic rays with lower energy than the primaries. These secondary particles can interact again, and a cascade of secondary particles originates, as shown in Figure 2.5. The number of secondary cosmic rays increases to a maximum and then decreases closer to the ground as the energy dissipates. The more energetic the primary cosmic ray, the deeper into the atmosphere the cascade can be observed. The number of particles in such a cascade shower is approximately proportional to the energy of the original primary particle.

Secondary particles can be divided into three groups, as shown in Figure 2.5:

- the nucleonic component (protons and neutrons),
- the electromagnetic or soft component (electrons, positrons, gamma rays), and
- the hard component (mainly muons).

Since cosmic rays lose energy in the atmosphere, not all secondary cosmic rays reach the ground. If the primary cosmic ray has energy > ~500 MeV, some secondary particles can reach the earth's surface and can be detected, e.g. by neutron monitors. The average propagation direction of the secondary particles is more or less the same as the incidence direction of the primary particle.

2.4 Solar modulation and observations with neutron monitors

Neutron monitors, described in Chapter 4, record mainly the energetic neutrons of the secondary shower. Information about the interactions of galactic cosmic radiation with the plasmas and magnetic fields in the heliosphere, as well as the production of energetic cosmic rays at the sun, can be obtained by detection of cosmic rays by a worldwide network of neutron monitors. According to McDonald (2000), these monitors are reliable, sensitive, have a high counting rate, with a basic simplicity, and are used to study the longer-term temporal variations, as well as short-term intensity changes.

As described in Section 2.3.2, the irregularities in the solar magnetic field scatter and convect the penetrating galactic cosmic rays. The consequence is a decrease in the intensity of cosmic rays, especially at low energies. This phenomenon is called heliospheric modulation. The underlying purpose of modulation studies is to demodulate the intensity spectra measured at earth to obtain the galactic spectra. Furthermore, cosmic ray modulation studies have to explain periodic and aperiodic variations in the intensities, e.g. the 22-year period, the 11-year cycle (due to the activity of the sun that varies with an 11-year cycle), the 27-day period (due to the rotation of the sun around its own axis), diurnal variations (due to the rotation of the earth around its own axis), as well as other short-term and aperiodic variations, e.g. Forbush decreases. The discussion of some of these variations follows.

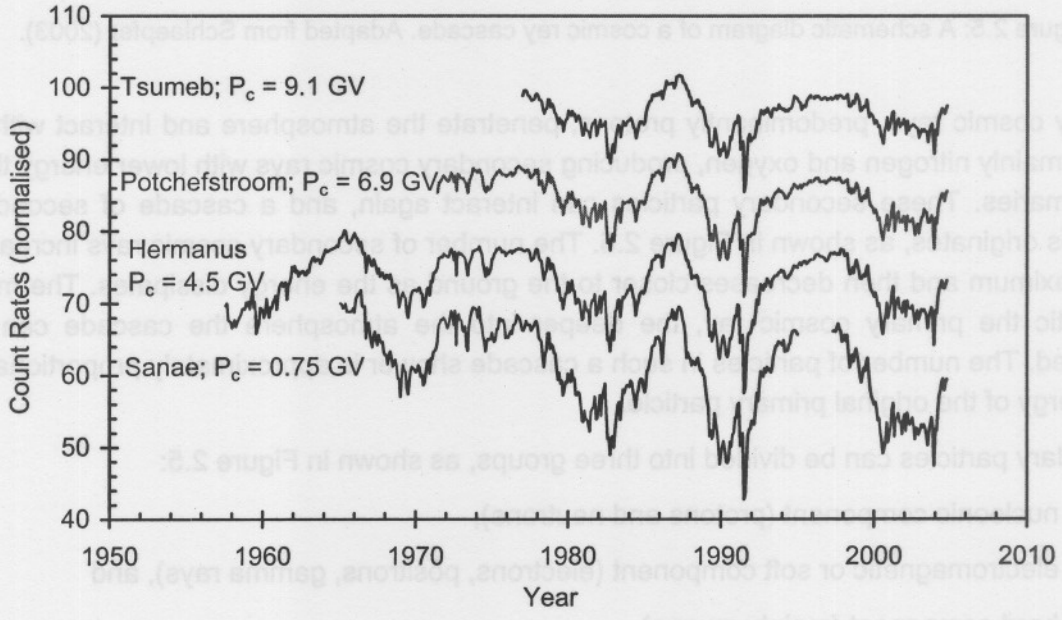

Fig 2.6: The monthly-normalised counting rate of the four neutron monitors at Sanae, Hermanus, Potchefstroom and Tsumeb.

Figure 2.6 shows the monthly average measurements of the four neutron monitors under the authority of the Unit for Space Physics at the North-West University in Potchefstroom, South Africa, i.e. at Sanae (Antarctica), Hermanus, Potchefstroom and Tsumeb (Namibia). The 11-

year solar cycle can be clearly seen by looking at the counting rates, with the highest amplitude at Sanae that has the lowest cutoff rigidity.

There is an anticorrelation between the intensity of cosmic rays and solar activity. Figure 2.7 illustrates this anti-phase relation between solar activity, as indicated by the 11-year sunspot cycle, and the cosmic ray intensity 11-year cycle. There is a decrease in intensity of cosmic rays as solar activity increases, and vice versa. Forbush (1954) was the first person to describe this anticorrelation. This observed anticorrelation of the cosmic ray intensity with solar activity explains the concept of heliospheric modulation, which was originally developed by Parker (1955). Schlickeiser (2002) remarked that the total reduction from solar minimum to solar maximum is typically about 20% for nucleons at neutron monitor energies.

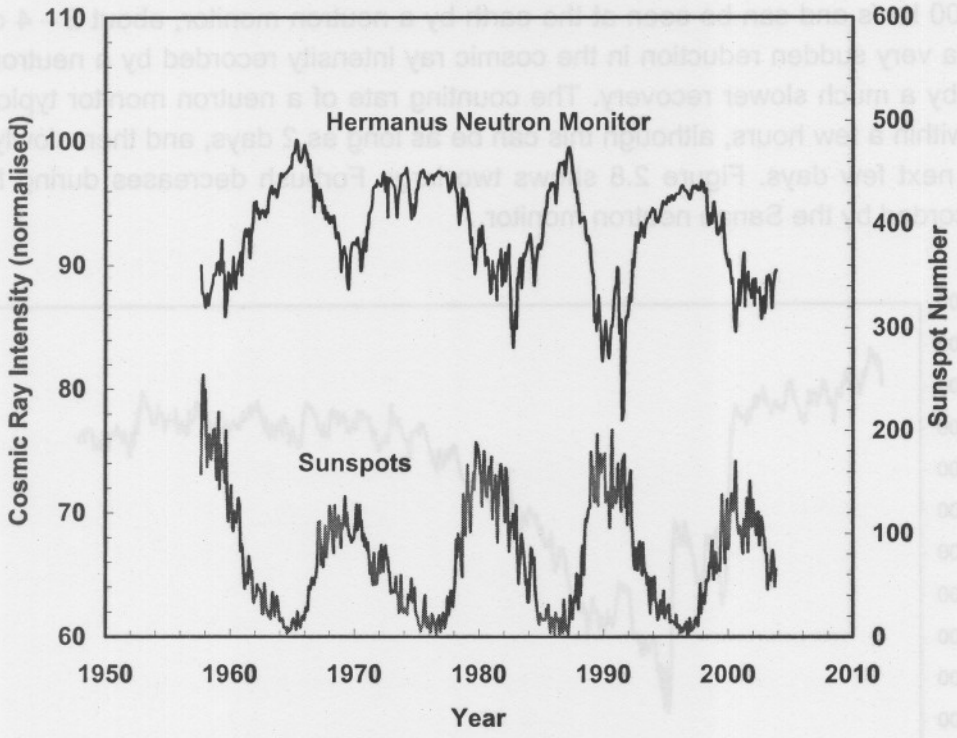

Figure 2.7: The relation between solar activity, indicated by sunspot numbers, and cosmic ray intensity, indicated by the counting rate of the Hermanus neutron monitor. The sunspot numbers peak every 11 years when the sun is most active.

Figures 2.6 and 2.7 show that the cosmic ray intensity also has a 22-year modulation. Every second peak between consecutive solar cycles has more or less the same shape, differing from adjacent peaks. It can be seen how sharp the modulation profile was around minimum modulation in 1965, and again in 1987, in contrast to what happened during minimum modulation in 1975 – 77 and in 1996 – 97. The existence of this 22-year modulation in cosmic rays was observed by Nagashima and Morishita (1980) with neutron monitor data. The reason for this 22-year cycle is due to the polarity reversal of the large-scale magnetic field of the sun near the time of maximum activity in every solar cycle. Drift effects play an important role in this phenomenon. When the solar magnetic field is directed outwards from the sun in the northern hemisphere ($qA > 0$), as in ~1970 – 1980 and ~1990 – 2000,

positively charged cosmic rays drift in over the solar poles and out along the heliospheric current sheet. When the solar magnetic fields are directed inwards in the northern region (qA < 0), as in ~1980 –90, the positively charged cosmic rays drift in along the current sheet and out over the poles.

A short-term aperiodic variation detected by neutron monitors is the so-called Forbush decrease. Scott E. Forbush showed that a rapid decrease in cosmic ray intensity correlates with a worldwide change in geomagnetic field intensity, which John Simpson called a Forbush-type decrease (Simpson, 2000). The characteristics of Forbush decreases were summarised, for example, by Lockwood (1971) and Cane (2000).

When the sun releases an exceptional amount of matter and a significant magnetic disturbance takes place, a Forbush decrease occurs. These disturbances travel at speeds of 400 – 1000 km/s and can be seen at the earth by a neutron monitor, about 2 – 4 days later. There is a very sudden reduction in the cosmic ray intensity recorded by a neutron monitor, followed by a much slower recovery. The counting rate of a neutron monitor typically drops by ~5% within a few hours, although this can be as long as 2 days, and then slowly recovers over the next few days. Figure 2.8 shows two large Forbush decreases during November 2004, recorded by the Sanae neutron monitor.

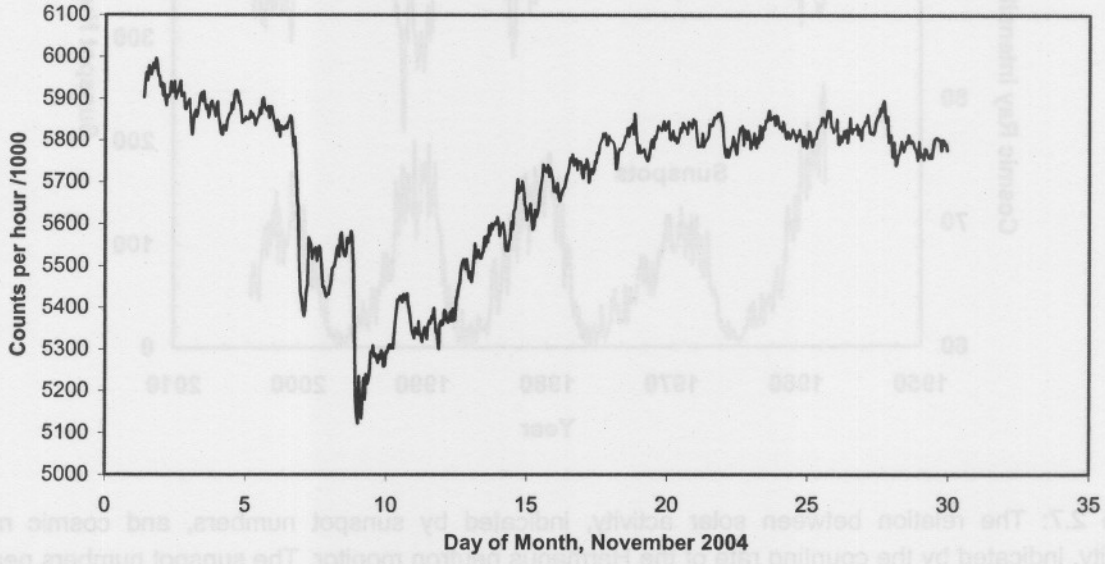

Figure 2.8: Two large Forbush decreases in November 2004, as recorded by the neutron monitor in Sanae, Antarctica. The recovery of the cosmic ray intensity within a few days can clearly be seen.

2.5 Solar cosmic rays

Cosmic rays arriving at the earth are usually of galactic, or even extragalactic, origin. The sun is sometimes, however, also a source of cosmic rays, with energies ranging from a few keV to several GeV. These events are called solar energetic particles (SEP).

Ryan *et al.* (2000) described SEPs as particles contained within the site of solar flares that are responsible for X-ray, γ-ray and neutron emission and particles accelerated at high

coronal altitudes and in interplanetary space by travelling disturbances such as CMEs. About 30% of the CMEs observed in the ecliptic plane have speeds high enough relative to the solar wind to produce shock wave disturbances. These shock waves play an important role in accelerating SEPs. These SEPs, with energies up to ~100 MeV, are frequently observed by spacecraft.

Relativistic solar protons events, with energies > ~450 MeV, can cause sufficiently high-energy secondary nucleons in the atmosphere to be detected by neutron monitors at ground level. According to Stoker (1994), these so-called ground level enhancements (GLEs) occur on average about once a year, much less than the number of SEPs observed in the upper atmosphere or outer space.

GLEs have been recorded since the 1940s, with event number 1 occurring on 28 February 1942. Stoker (1994) analysed recorded GLEs at Sanae in detail. Figure 2.9 shows the large increase of ≈ 200% in the particle flux of event number 69, on 20 January 2005, as seen by the neutron monitor (6NM64) and the neutron-moderated detector (4NMD) at Sanae. This event had a complicated three-peak structure, as Moraal *et al.* (2005) elaborated upon.

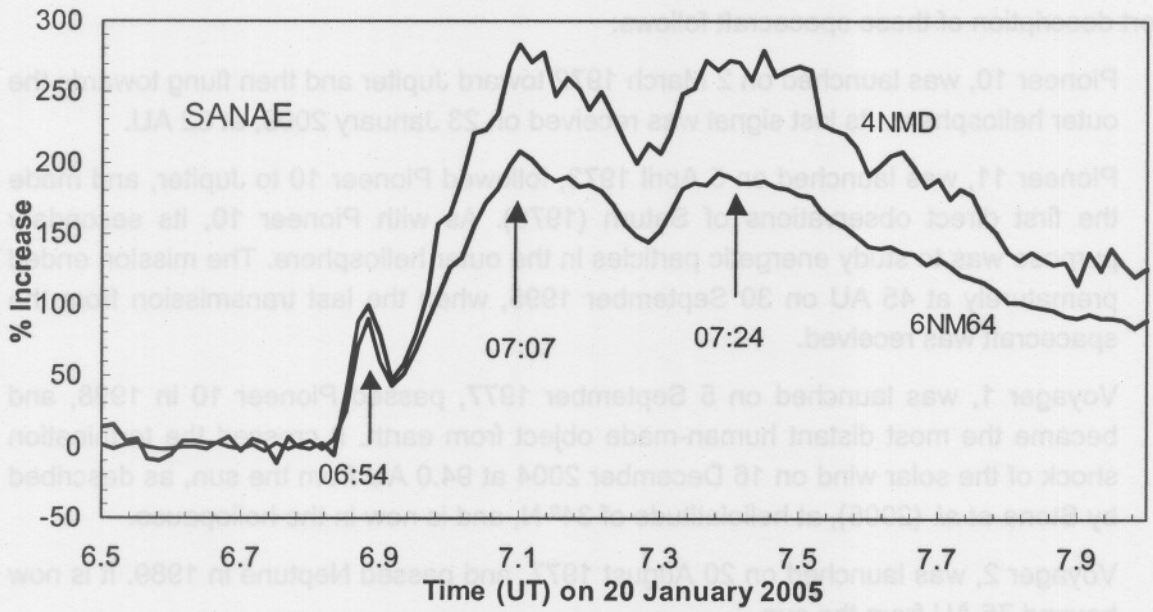

Figure 2.9: A large solar flare recorded by two monitors in Sanae, on 20 January 2005. Adapted from Moraal *et al.* (2005).

Lockwood and Debrunner (1999) discussed methods to use neutron monitors for the study of solar cosmic ray GLEs. They regarded these neutron monitor measurements very useful to understand proton acceleration at or near the sun, as well as solar neutron production. SEPs and GLEs provide important information about the transport of energetic particles in the inner heliosphere.

2.6 Spacecraft observations

With the arrival of the Space Age in 1957, together with the neutron monitor network, the study of cosmic rays has led to a better understanding of the structure of the outer heliosphere, solar modulation, and transport of cosmic rays.

Explorer VI, launched in 1958, and Pioneer V, launched in 1960, were the first spacecraft with instruments to study cosmic rays and magnetic fields at great distances from earth. Large Forbush decreases occurred during the course of both voyages. McDonald (2000) described these spacecraft and neutron monitor observations of Forbush decreases in detail.

The satellite IMP 6 was launched in 1971 and was followed by other spacecraft. With these spacecraft it is possible to continuously monitor galactic and anomalous cosmic rays, as well as SEPs, to energies of a few 100 MeV.

During the past decades, the four spacecraft, Pioneer 10 and 11, and Voyager 1 and 2, on deep space missions, with Ulysses inside of 5 AU, and the satellite IMP 8 at 1 AU, have provided information about energy spectra of cosmic rays throughout the heliosphere. Data obtained by these spacecraft have greatly increased our knowledge and understanding of the heliosphere, as well as effects inferred from neutron monitor data.

A short description of these spacecraft follows:

- Pioneer 10, was launched on 2 March 1972 toward Jupiter and then flung towards the outer heliosphere. Its last signal was received on 23 January 2003, at 82 AU.
- Pioneer 11, was launched on 5 April 1973, followed Pioneer 10 to Jupiter, and made the first direct observations of Saturn (1979). As with Pioneer 10, its secondary purpose was to study energetic particles in the outer heliosphere. The mission ended prematurely at 45 AU on 30 September 1995, when the last transmission from the spacecraft was received.
- Voyager 1, was launched on 5 September 1977, passed Pioneer 10 in 1998, and became the most distant human-made object from earth. It crossed the termination shock of the solar wind on 16 December 2004 at 94.0 AU from the sun, as described by Stone *et al.* (2005), at heliolatitude of 34° N, and is now in the heliopause.
- Voyager 2, was launched on 20 August 1977, and passed Neptune in 1989. It is now beyond 75 AU from the sun.
- The Ulysses spacecraft was launched in October 1990, exploring the regions above the solar poles.

McDonald (2000) considered the complementary relation between neutron monitor studies and space observations. The ground-based neutron monitors have examined in detail cosmic ray variations ranging from the 22-year and 11-year cycles, the 27-day variations, diurnal variations, and Forbush decreases, to high-energy solar particle events. The space observations extend these studies to lower energies that led, for example, to the discovery of the shock acceleration of energetic protons, ions and electrons and of the anomalous cosmic ray component. He mentioned further that it was shown, with the aid of early spacecraft observations, that Forbush decreases are not caused by changes in the geomagnetic field, but by interplanetary disturbances. Parker's concepts of the solar wind and the interplanetary

magnetic field were thereby confirmed. Data of neutron monitors helped in interpreting these results. The identification of coronal holes as the source of high-speed solar wind streams, as well as CMEs that produce interplanetary disturbances and acceleration of solar energetic particles, are obtained from space data together with the interpreting of neutron monitor data.

McDonald (2000) considered that, with new emphasis on carefully intercalibrated networks of neutron monitors and the improved instrumentation for space studies, these complementary relations should extend the understanding of the acceleration and transport of energetic particles in the heliosphere in the future. The calibration neutron monitor of this work represents such an attempt.

2.7 Equation for the transport of cosmic rays in the heliosphere

As described in Section 2.4, cosmic rays move through the heliosphere and are modulated by the heliospheric magnetic field and solar activity. This irregular magnetic field, carried outward from the sun by the solar wind, causes the cosmic rays to have an outward convective flow. This radially outward flow, combined with inward particle diffusion in the irregularities of the heliospheric magnetic field, basically causes the 11-year modulation variation.

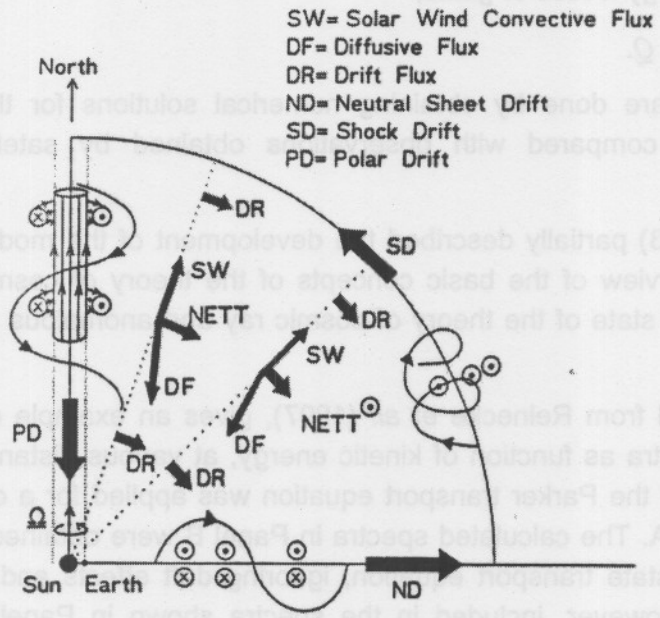

Figure 2.10: The major cosmic ray transport processes, shown in a quarter heliosphere. Adapted from Moraal (1993).

Apart from these diffusion-convection effects, cosmic rays undergo adiabatic energy losses in the outflowing and expanding solar wind. Conversely, compressions and/or shocks in the magnetic field cause adiabatic gains. Furthermore, drift effects, as mentioned in Section 2.4, influence the transport of cosmic rays too. These major basic effects are shown in Figure 2.10.

Parker (1958b) derived an equation for the transport of the cosmic rays through the heliosphere, which included the basic physical processes. The equation was rederived several times, e.g. Gleeson and Axford (1967). Jokipii *et al.* (1977) gave a comprehensive description of the significant contribution of drift effects to cosmic ray modulation. Moraal (1993) gave the transport equation in terms of particle momentum p and the omni-directional distribution function f, which is related to the differential intensity by $j \propto p^2 f$:

$$\frac{\partial f}{\partial t} = \nabla \cdot (\mathbf{K} \cdot \nabla f) - (\mathbf{V} + \mathbf{V}_{drift}) \cdot \nabla f + \frac{1}{3} (\nabla \cdot \mathbf{V}) \frac{\partial f}{\partial \ln p} + Q \,. \qquad (2.1)$$

This Parker transport equation states that the rate of change of cosmic ray intensity with time is caused by:

- inward particle diffusion described by a diffusion tensor **K**, produced by scattering in the irregularities of the interplanetary magnetic field;
- outward convection by the solar wind with velocity **V**;
- gradient and curvature drifts due to the large-scale structure of the heliospheric magnetic field, with velocity $\mathbf{V}_{drift}$;
- adiabatic energy losses or gains;
- a source term Q.

Modulation studies are done by obtaining numerical solutions for this equation. These solutions are then compared with observations obtained by satellite and spacecraft measurements.

Reinecke *et al.* (1993) partially described the development of the modulation models. Fisk (1999) gave an overview of the basic concepts of the theory of cosmic ray transport; he reviewed the current state of the theory of cosmic ray and anomalous particle behaviour in the heliosphere.

Figure 2.11, adapted from Reinecke *et al.* (1997), gives an example of the modulation of proton intensity spectra as function of kinetic energy, at various distances from the sun. A numerical solution of the Parker transport equation was applied for a one-dimensional, no-drift model in Panel A. The calculated spectra in Panel B were obtained with a simplified 2-dimensional steady-state transport equation, ignoring drift effects and shock acceleration. Drift effects were, however, included in the spectra shown in Panel C. The differences between the solutions give an indication of the relative importance of the various modulation mechanisms. These two solar minimum periods are supposed to be quite different, due to oppositely directed drift fluxes in consecutive solar cycles. The spectra were calculated from 1 – 61 AU, for the consecutive solar minimum periods in 1977 ($qA > 0$) and 1987 ($qA < 0$) and the first half of 1995 ($qA > 0$). These calculated spectra were compared with observations by the spacecraft Pioneer 10 and 11, Voyager 1 and 2, and the satellite IMP8 for 1977 and 1995 (open symbols) and 1987 (filled symbols). (The data sets were multiplied with different scale factors for better visual presentation).

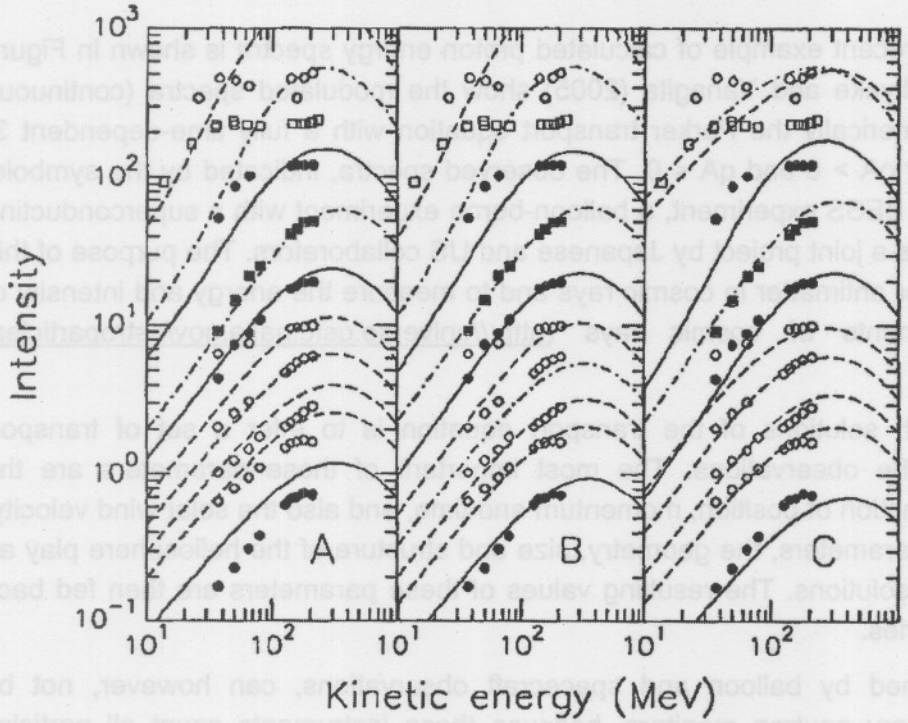

Figure 2.11: Calculated intensity spectra with different models (lines) and spacecraft observations (symbols). Adapted from Reinecke *et al.* (1997).

Kota and Jokipii (1983) developed a fully 3-dimensional, dynamically self-consistent solution, including all known important effects on particle transport, particle drifts, convection, anisotropic diffusion and energy losses. Their model is time-independent in the coordinate frame rotating with the sun. Hattingh (1998) solved the steady-state transport equation in a 3-dimensional numerical modulation model, using a wavy current sheet and a latitudinal-dependent solar wind.

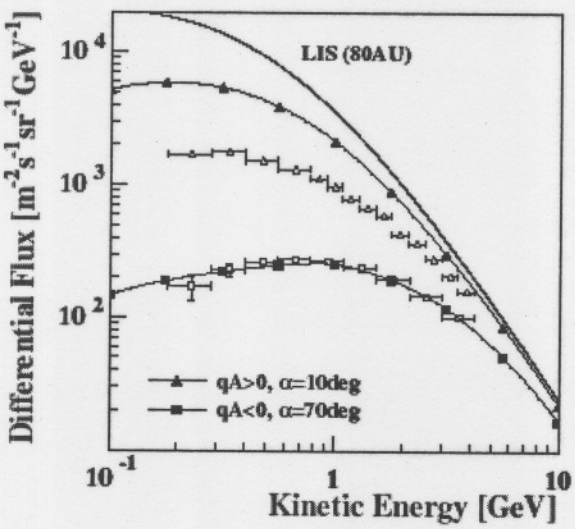

Figure 2.12: Calculated proton intensity spectra (continuous lines) and BESS observations (symbols). Adapted from Miyake and Yanagita (2005).

Another and a more recent example of calculated proton energy spectra is shown in Figure 2.12. In this figure Miyake and Yanagita (2005) show the modulated spectra (continuous lines), by solving numerically the Parker transport equation with a fully time-dependent 3-dimensional code, for qA > 0 and qA < 0. The observed spectra, indicated by the symbols, were obtained by the BESS experiment, a balloon-borne experiment with a superconducting spectrometer, which is a joint project by Japanese and US collaborators. The purpose of this project is to search for antimatter in cosmic rays and to measure the energy and intensity of less exotic components of cosmic rays (http://universe.gsfc.nasa.gov/astroparticles/programs/bess).

The purpose of such solutions of the transport equation is to infer a set of transport parameters that fit the observations. The most important of these parameters are the diffusion tensor as function of position, momentum and time, and also the solar wind velocity. In addition to these parameters, the geometry, size and structure of the heliosphere play an important role in the solutions. The resulting values of these parameters are then fed back into the relevant theories.

Such spectra, obtained by balloon and spacecraft observations, can however, not be acquired with stationary neutron monitors, because these instruments count all particles above a certain cutoff, as described in Chapter 5. One way to circumvent this problem has been to conduct so-called latitudinal surveys with neutron monitors in order to derive such spectra, as described in Chapters 5 and 7. Another way to derive intensity spectra from neutron monitor data would be to calibrate the worldwide network of stationary neutron monitors against each other, and to derive spectra from differences in counting rate. In order to do this, two calibration neutron monitors were built and tested, as described in Chapters 6 and 8.

To conduct such latitudinal surveys and to do the intercalibration, the so-called cutoff rigidities of neutron monitors must be known. Therefore the next chapter describes the geomagnetic field models, the transport of cosmic rays through this field, and the calculation of these cutoff rigidities.

Chapter 3
Geomagnetic Effects and Cutoff Rigidities

3.1 Introduction

The propagation of cosmic rays is not only influenced by the heliospheric magnetic field carried along by the solar wind plasma, but also by the geomagnetic field (GMF). Knowledge of the GMF is thus needed to describe the transport of charged particles in this field.

The GMF is generally divided in an internal field, generated by the core and the crust of the earth, and the external field, generated in the ionosphere and the magnetosphere. The core field, also called the main field, to first order forms approximately a dipole with an axis inclined by 11.5° with the rotation axis of the earth. This core field is the main contributor to the GMF. It changes regularly on the long term.

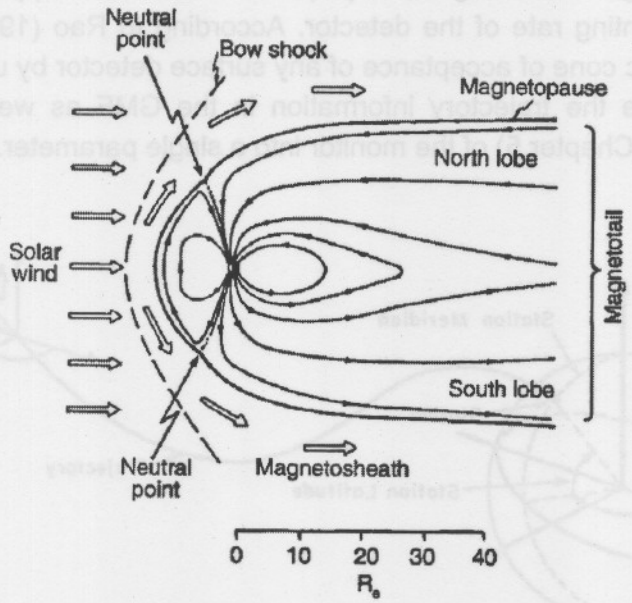

Figure 3.1: A sketch of the magnetosphere. Adapted from Gombosi (1998).

The magnetosphere is deformed by the solar wind pressure, as shown in Figure 3.1. Therefore, the magnitude of the GMF is larger on the dayside, and on the dark side it has a large magnetotail. The high latitudinal geomagnetic lines are mostly dipolar. The solar wind is highly time-dependent and therefore its pressure on the GMF as well. This gives rise to changes in the GMF near the earth's surface.

Smart *et al.* (2000) recently gave a review of models of the GMF and the trajectory computations of cosmic rays in this field, in order to determine the so-called cutoff rigidities, as described in Section 3.2. These cutoff rigidities, the minimum rigidity the particles from an asymptotic direction (defined in the following section) must have to be detected at a given position, are well-known for operating neutron monitors, to calculate cosmic ray spectra from

latitude surveys (see, e.g. Chapter 5), and to evaluate the characteristics of short-term variations such as Forbush decreases and ground level events, as mentioned in Chapter 2. These cutoff rigidities are also fundamental for the concept of calibration of neutron monitors, and are therefore discussed in this chapter.

3.2 Cosmic ray trajectories and cutoff rigidities

The geomagnetic field deflects cosmic rays in such a way that their arrival directions at the detector may not correspond to their original directions of approach. In general, particles follow rather complicated trajectories through the magnetosphere. The directions of the particles before entering the magnetosphere are defined as their asymptotic directions of approach, as shown in Figure 3.2. The direction of arrival at the top of the atmosphere is usually specified by the angles θ and ϕ as the zenith and azimuth angles, respectively, while the asymptotic directions of approach are represented by the asymptotic latitude Λ and longitude Ψ.

A concept, the 'asymptotic cone of acceptance of the detector', is defined by Rao *et al.* (1963) as the solid angle containing the asymptotic directions of approach that contribute significantly to the counting rate of the detector. According to Rao (1972), it is possible to calculate the asymptotic cone of acceptance of any surface detector by utilising the trajectory data, which incorporate the trajectory information in the GMF as well as the differential response function (see Chapter 5) of the monitor into a single parameter.

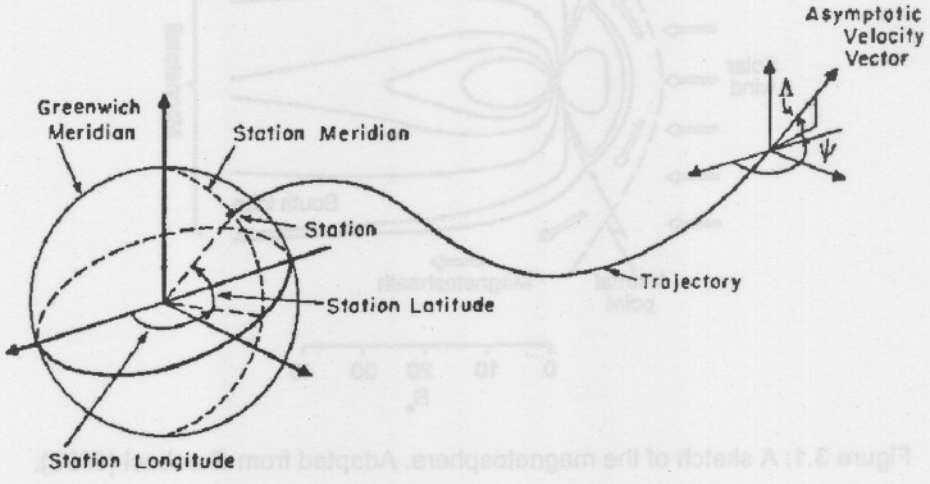

Figure 3.2: A sketch of a typical cosmic ray trajectory. Adapted from Shea and Smart (1967).

The precise trajectories are of primary importance for studying anisotropies, like GLEs (see Chapter 2) and diurnal variations. A network of neutron monitors will observe the amplitudes of these anisotropy enhancements as a strong function of the viewing direction.

On the other hand, galactic cosmic ray intensities are almost entirely isotropic. Then the GMF serves as a shield as well as a natural spectrometer for cosmic rays. In this case, the parameter of primary importance is the minimum rigidity (defined in the following paragraphs) that a particle must have to reach a detector at a given location.

A charged particle that moves with velocity **v** in a uniform magnetic field **B** experiences a force according to the relationship

$$m(\frac{d\mathbf{v}}{dt}) = q(\mathbf{v}\times\mathbf{B}). \qquad (3.1)$$

The solution to this equation leads to spiral orbits around **B**, with a so-called gyroradius r_g:

$$r_g = \frac{mv}{qB}\sin\alpha,$$

where q is the charge of the particle, and α is the pitch angle between the velocity and the magnetic field **B**. The gyroradius of a particle is determined by its relativistic momentum (**p**=m**v**) per unit charge:

$$r_g = \frac{pc}{qBc}\sin\alpha.$$

The particle's properties can be characterised by the rigidity $P = pc/q$, i.e. momentum p per unit charge q. Thus

$$r_g = \frac{P}{Bc}\sin\alpha.$$

According to the total energy relation

$$(T + E_0)^2 = p^2c^2 + E_0^2$$

it follows that, if T and E_0 are expressed in eV, then pc is also expressed in eV, and thus the rigidity P has the unit of volt (V). Particles having the same rigidity P follow identical trajectories.

When the energy is too low, cosmic rays are prevented from reaching the atmosphere through the GMF. In this case, the concept of minimum rigidity for a particle to reach a detector at a given location is important.

The cutoff rigidity P_c (θ, ϕ) is defined as the lowest rigidity a charged particle can possess and still arrive at a specific point on the earth's surface from the direction specified by both the zenith θ and azimuth ϕ angles of arrival at the top of the atmosphere (Shea *et al.*, 1965). By common usage, however, the cutoff rigidity at a specific point at the top of the atmosphere is typified by the minimum rigidity for which cosmic rays can arrive at that point from the zenith. This rigidity is defined as the vertical cutoff rigidity, and varies from 0 at the geomagnetic poles to ~15 GV at the magnetic equator, and up to 17 GV in the equatorial regions of South-East Asia.

The development of field models to calculate the (1) cutoff rigidity at a specific position and (2) asymptotic directions of approach, by means of numerical calculations in modelling cosmic ray trajectories in the earth's magnetic field, is described in the following sections.

3.3 Development of geomagnetic field (GMF) models

Initially a simple centred dipole approximation was used to describe particle motion in the GMF. This field can be represented at the surface to first order by the field of a bar magnet with magnetic dipole moment $\mathbf{M}$ placed at the earth's centre. Its geomagnetic axis is tilted by 11.5° with respect to the geographic axis of rotation. According to Merrill and McElhinny (1983) this dipole accounts for roughly 90% of the surface field; when the best fitting geocentric dipole is removed, about 10% of the field at the earth's surface remains, which is called the non-dipole field. Both the dipole and non-dipole parts of the earth's magnetic field are time-dependent.

Le Roux (1986) studied the transfer of charged particles in dipole magnetic fields using analytical calculations, the so-called classical Størmer theory, as well as in sixth-degree axially symmetric fields and in the real geomagnetic field. The magnetic field $\mathbf{B}$ in terms of the magnetic vector potential $\mathbf{A}$ is given by

$$\mathbf{B} = \nabla \times \mathbf{A},$$

with

$$\mathbf{A} = -\left(\frac{M}{r^2}\right)\sin\theta\mathbf{e}_\phi .$$

The magnetic moment $M \approx 8\text{x}10^{15}$ T m^3 and is directed in the geographic southern direction. In axially symmetric fields, $\mathbf{A}$ is only a function of r and θ in the spherical coordinate system (r, θ, ϕ), with unit vectors $\mathbf{e}_r$, $\mathbf{e}_\theta$ and $\mathbf{e}_\phi$. The surface field intensity is about 50 000 nT at the poles and about 30 000 nT at the equator.

The GMF is, however, neither a dipole nor axially symmetric. Therefore, the only method to calculate the trajectories of charged particles, and thus cutoff rigidities, is the numerical integration of the equation of motion (3.1).

The mathematical representation of the GMF is described quantitatively by a spherical harmonic model, which is discussed in detail by Merrill and McElhinny (1983). Various combinations of data of the GMF and its variation in time are used to obtain coefficients of this spherical harmonic description. The magnetic field is obtained from the scalar magnetic potential $V(r, \theta, \phi)$ in the current-free regions. Some of the terms collectively represent the dipole field, while the remaining terms represent the non-dipole part.

Smart *et al.* (1969) utilised a magnetic field model containing both the internal and external fields to calculate particle trajectories:

$\mathbf{B}_I = \nabla V$ is the internal field, where the magnetic potential V is obtained by a spherical harmonic expansion;

$\mathbf{B}_S$ is the external field due to currents in the magnetopause; and

$\mathbf{B}_{CS}$ is the external field due to currents in the neutral sheet of the magnetospheric tail.

Mathematical models describing the GMF have improved over the years. A working group of the International Association of Geomagnetism and Aeronomy (IAGA) evaluates and

approves these models. Shea *et al.* (1990) described two terms for the geomagnetic reference field, as approved by the IAGA, as follows:

- International Geomagnetic Reference Field (IGRF): These models are interim models, accurate for present purposes derived from available data.
- Definitive Geomagnetic Reference Field (DGRF): These models are the "final" internationally accepted models for epochs in the past after all the available magnetic data can be adequately evaluated.

Since 1940, this working group of IAGA has determined models of the DGRF every 5 years.

Tsyganenko (1989) developed an improved quantitative representation of the GMF. This model takes into account the effect of (1) the magnetic field ring current, (2) the magnetic field from the magnetotail currents, including the plasma sheet current and return currents, (3) the magnetopause contribution, and (4) the averaged magnetic effect of field-aligned currents. He also used data from the IMP and HEOS satellites in developing this model.

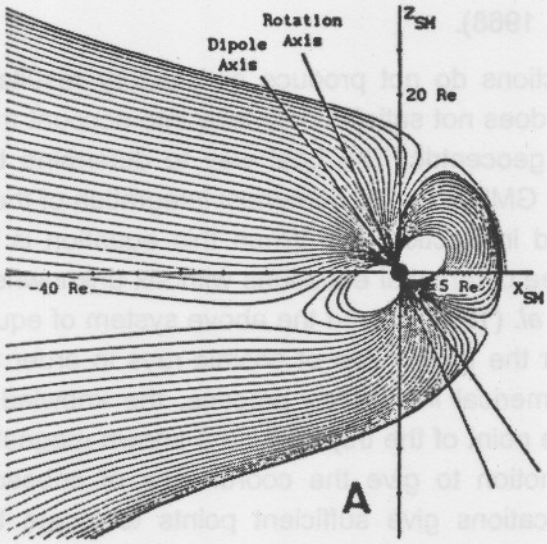

Figure 3.3: The magnetospheric field line pattern, as described by the Tsyganenko (1989) model. Adapted from Flückiger *et al.* (1991).

Smart *et al.* (2000) emphasized that the accuracy of the magnetic field models employed may be the limiting factor in charged particle trajectory calculations. It has become a common procedure to combine the internal magnetic field of the earth (usually represented by the IGRF magnetic field model) with a model of the external field based on the analysis of spacecraft measurements. Figure 3.3 is an illustration of such a magnetic field line topology. In this figure, Flückiger *et al.* (1991) modelled the magnetosphere by combining the DGRF/IGRF models for 1945 – 1985, representing the geomagnetic main field, together with the model of the external current systems derived by Tsyganenko (1989). Bütikofer *et al.* (1995 and 1997) improved on this model by also including the magnetic field in the magnetosheath, developed by Kobel and Flückiger (1994).

As mentioned in Section 3.2, there are two aspects of the motion of charged particles in the GMF that are important: (i) the cutoff rigidities below which cosmic rays cannot reach the earth and (ii) the asymptotic directions of the trajectories of the particles outside the magnetosphere. These two aspects are discussed in the following sections.

3.4 Calculation of cutoff rigidities

The pioneer researchers, like Carl Størmer, used the simple dipole representation of the GMF during the early 20th century in order to study the motion of charged particles in this dipole field and to calculate cutoff rigidities. According to Le Roux (1986), the vertical cutoff rigidity in a dipole field is given by

$$P_c = \frac{Mc}{4r_e^2}\cos^4\lambda = 14.9\cos^4\lambda \text{ GV}, \qquad (3.2)$$

where λ is the geomagnetic latitude, and r_e is the earth's radius. This expression is valid for any direction of arrival lying in the meridian plane of the observation point for a transparent earth (Hofmann and Sauer, 1968).

These Størmer cutoff functions do not produce satisfactory results. This theory assumes longitudinal symmetry and does not satisfactorily take into account the offset of the effective magnetic centre from the geocentric. The best way to determine the cutoff rigidities in a realistic reproduction of the GMF is by the numerical integration of the differential equation of motion (3.1), as mentioned in Section 3.3. When this equation is expressed in spherical coordinates, it leads to three differential equations with six unknowns that can be integrated numerically. McCracken *et al.* (1962) solved the above system of equations with fourth order Runge-Kutta integration for the trajectories of cosmic rays in order to calculate cosmic ray cutoff rigidities. In this numerical integration process, the knowledge of the position and velocity coordinates on one point of the trajectory in a known magnetic field is used with the differential equations of motion to give the coordinates of subsequent points along the trajectory. Repeated applications give sufficient points to locate the trajectory in space (Smart *et al.*, 2000).

This trajectory-tracing program calculates the trajectory of a negatively charged particle moving outward from the earth from a specific location and direction. This trajectory is the same as that of the positively charged particle of equal rigidity approaching the earth to arrive at the same position from the same direction. Shea *et al.* (1965), Shea and Smart (1967), Smart *et al.* (1969), Humble *et al.* (1985), Smart *et al.* (2000), and Cooke *et al.* (1991) described this program in detail.

The cutoff rigidities are calculated by starting with a cosmic ray trajectory at the top of the atmosphere, at an altitude of 20 km above a specific location on earth, with a vertical incidence, i.e. with a zenith angle of 0°. This trajectory is followed until access to the interplanetary medium (at 25 earth radii) is assured, when the trajectory is allowed, otherwise the trajectory is called forbidden. Forbidden trajectories are those which intersect the solid earth, called re-entrant trajectories, and those for which no solution can be obtained within a reasonable number of iterations selected arbitrarily in the program – initially it was 15 000 iterative steps and later up to 600 000 steps were imposed. At higher rigidities most

trajectories are completed well within 15 000 steps, but the trajectories of very low rigidity particles can become very complicated with many loops, such that often 600 000 steps may still fail to reach a solution.

To summarise, the calculations are terminated when any of the following conditions is reached (Smart *et al.*, 1969):

1. The orbit intersects the solid earth (re-entrant and forbidden trajectory).
2. The orbit reaches the magnetopause.
3. The orbit extends into the tail to a distance greater than 25 earth radii (R_e).
4. None of the previous conditions has been satisfied by an arbitrary large chosen number of iterative steps.

Smart *et al.* (2000) described the escape or re-entrance of the cosmic rays. They considered trajectories of particles with different energies in the GMF. A very high-energy particle propagates outward through the GMF and reaches interplanetary space with a minimum amount of geomagnetic bending. A charged particle with lower energy undergoes more geomagnetic bending before it can escape. At some lower energy, it no longer has sufficient momentum to escape the magnetic field and then the particle with an initially outward directed trajectory near the top of the atmosphere, re-enters. A still lower energy trajectory escapes after a series of complex loops near the earth. These series of allowed and forbidden bands of particle access are called the cosmic ray penumbra. Therefore, cosmic ray geomagnetic cutoff rigidities are not sharp, except for special cases in the equatorial regions.

In order to determine geomagnetic cutoff rigidities, trajectory calculations at discrete intervals are made, beginning at a value above the highest possible cutoff, and progress down in steps through a rigidity spectrum scan, until the lowest possible allowed trajectory, called the upper cutoff, has been found. Then the first discontinuity in asymptotic direction, i.e., the first forbidden trajectory, is obtained, which is the start of the cosmic ray penumbra. The last allowed trajectory identifies the lower end of the cosmic ray penumbra, the lower cutoff. The effective cutoff rigidity, P_c, is then a weighted average between the upper and the lower cutoff rigidities.

Shea and Smart (1967) computed a worldwide grid of vertical cutoff rigidities for every 5 degrees in latitude and 15 degrees in longitude for epoch 1955. They showed how interpolations obtained from this grid could be used to order experimental cosmic ray intensity data. As more advanced and accurate geomagnetic field modelling became possible, and the speed of computer calculations improved, worldwide grids of vertical cutoff rigidities were calculated for epochs 1965, 1975 and 1980, according to Shea *et al.* (1990, and references therein) and Shea *et al.* (1983). The grid for 1980 is shown in Figure 3.4. The spherical harmonic coefficients for the 1980 model were derived from data obtained from the MAGSAT satellite; this was the first international model completely derived from spacecraft data with the satellite measurements being made in late 1979 and early 1980.

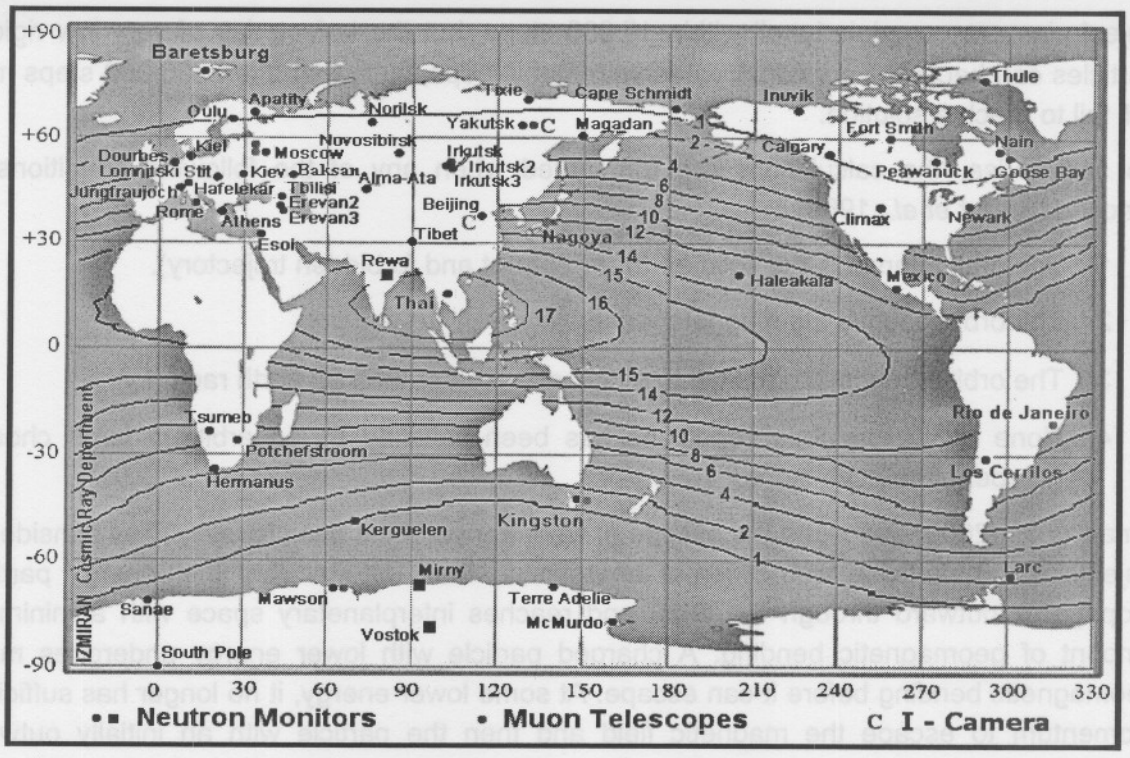

Figure 3.4: Illustration of the effective vertical cutoff rigidities for a world grid (Shea and Smart, 1983) using the IGRF model for epoch 1980.0. From K.R. Pyle (private communication).

Shea *et al.* (1990) recomputed the cosmic ray vertical cutoff rigidities for 1980 using the DGRF for 56 neutron monitor locations. Their recomputed cutoff values compared favourably with the earlier values computed for 1980 using the IGRF model. Table 3.1 shows the difference in the cutoff rigidities of several selected neutron monitor stations between the 1980 IGRF model and the 1980 DGRF model.

Table 3.1: Calculated vertical cutoff rigidities

	1980 IGRF model	1980 DGRF model	1995 IGRF model
Climax, USA	2.95	2.99	2.93
Deep River, Canada	1.15	1.14	1.25
Hermanus	4.55	4.58	4.45
McMurdo	0.00	0.00	0.00
Potchefstroom	6.94	7.00	6.85
Sanae	0.86	0.86	0.75
Tsumeb, Namibia	9.15	9.21	9.06

Smart and Shea (1997) updated their world grid of effective vertical incident cosmic ray cutoff rigidities, using the DGRF model for epoch 1990.0. These new cutoff rigidity values show the effects of the continued changes in the geomagnetic field. They calculated cutoff rigidities in a three times denser grid, every 5° in latitude and 5° in longitude. When they compared these values with those determined for epoch 1980.0, they found significant and systematic differences. They found on average a decrease, that reflects changes in the main dipole component, and because these changes are not uniform over the world, they suggested that the non-dipole terms are relatively important for an accurate determination of cutoff rigidities near the surface of the earth.

The most recent tables with calculated cutoff rigidities for stationary monitors for 1995 can be obtained in Shea and Smart (2001). A few of these cutoff rigidities are shown in Table 3.1, in comparison with the 1980 values.

In general, it has been sufficient to use vertical cutoff for the effective cutoff rigidities. This is so because cosmic ray arrival directions are strongly centred on the zenith direction due to atmospheric absorption. However, as mentioned by Clem *et al.* (1997), since cosmic rays arrive almost isotropic, there is still a significant population of obliquely incident primaries. Because cutoff rigidities depend upon the direction of incidence, they introduced the term 'apparent' cutoff rigidity to accommodate obliquely primary cosmic rays. They defined the apparent cutoff rigidity as that rigidity which, if uniform over the whole sky, would yield the same neutron monitor counting rate as the real, angular dependent cutoff distribution. Thus, these apparent cutoff rigidities improve upon the vertical cutoff rigidity by including effects of obliquely incident particles.

Bieber *et al.* (1997) recomputed these apparent cutoff rigidities with some approximations to save on computation time. They investigated and described the differences between the vertical and apparent cutoff rigidities calculated by Clem *et al.* (1997), who used these apparent cutoff rigidities to interpret a sea level neutron monitor latitudinal survey. They found that effects due to obliquely incident primaries are significant and may be responsible for anomalies observed in this and other latitudinal surveys.

To investigate the effect of apparent cutoff rigidities, Stoker *et al.* (1997) compared vertical cutoff rigidities with apparent cutoff rigidities at 30 000 feet pressure altitude in the South African region, and concluded that it appears that apparent cutoff rigidities are a much better ordering parameter of neutron monitor survey data at 30 000 feet pressure altitude than vertical cutoff rigidities in that region, confirming that obliquely incident particles must be incorporated in the calculations of accurate effective cutoff rigidities.

Vertical cutoff rigidities are calculated in Chapter 7 using this formalism, and one of the early McCracken programs provided by Shea and Smart (2005, private communication).

3.5 Field models to calculate asymptotic directions of approach

By using high-order simulations of the GMF to calculate trajectories of cosmic rays in the GMF with current fast computers, not only a worldwide grid of cosmic ray cutoff rigidities can be calculated, but the asymptotic cones of acceptance for the worldwide network of cosmic ray stations can also be determined.

An example is the early works of Gall *et al.* (1969), who calculated the asymptotic directions of approach of a particle of given rigidity by numerical integration of the orbit for a series of stations and directions of incidence. When a model of the GMF is used, the integration is carried out from the station outward up to the boundary of the domain of the field, and the asymptotic directions of approach are computed at the crossing point. They used a modified McCracken program, described in the previous section, to compute the orbits of cosmic ray particles. They mentioned that the directions along which particles of specific rigidity cross the magnetopause to reach a station from all possible directions of incidence, form a cone. In other words, the asymptotic cone of acceptance is defined by the set of asymptotic directions accessible at a specific position. These cones are very wide for stations near the equator, but narrow down as the rigidity lowers for stations at higher latitudes, where the direction of viewing is not a strong function of rigidity. Neutron monitors at geomagnetic latitudes > 60° have asymptotic cones of acceptance lying close to the equatorial plane. It seems that the general property of the GMF is to bend asymptotic directions of viewing towards the equator.

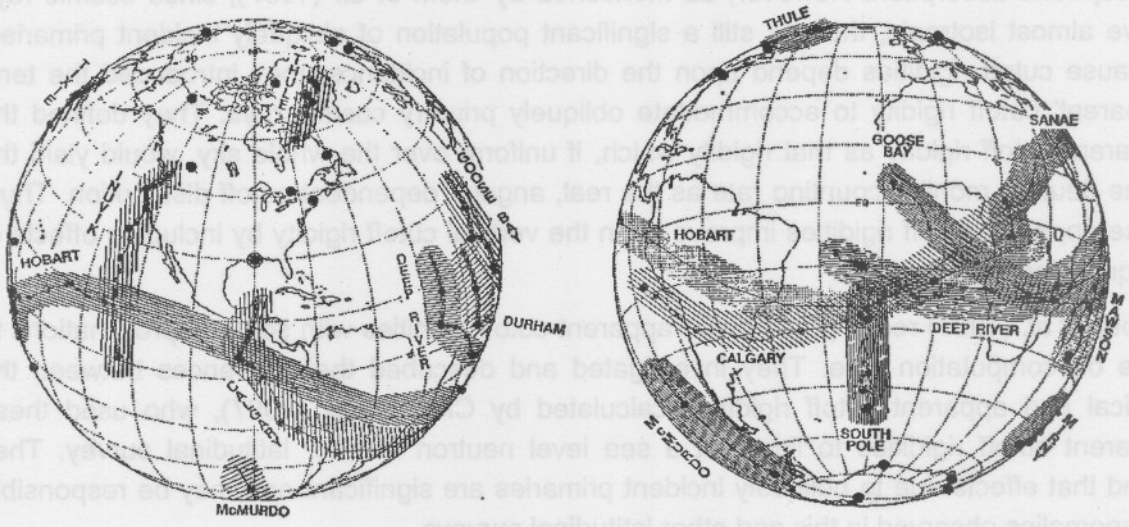

Figure 3.5: Asymptotic directions of approach calculated for several neutron monitors. Adapted from Smart *et al.* (2000).

For example, Figure 3.5 shows some typical asymptotic directions of approach for neutron monitors at several stations. This figure reveals the importance of stations at polar latitudes, where it is possible to observe particles from a narrow cone of the celestial sphere, such as Thule, South Pole, McMurdo, and Mirny, versus Calgary and Hobart.

As proposed by Bieber and Evenson (1995), the Bartol Research Institute is exploiting an Arctic/Subarctic neutron monitor network, the so-called Spaceship Earth, with nine stations viewing within 24° of the equatorial plane with narrow cones of acceptance. With this network, they are making optimal studies of GLEs, e.g. the "Bastille Day event" on 14 July 2000 (Bieber *et al.*, 2002), a very large enhancement on 15 April 2001 (Bieber *et al.*, 2004), and the three consecutive GLEs on 28 October, 29 October and 2 November 2003 (Bieber *et al.*, 2005).

The concept of asymptotic directions is not used further in this thesis.

Chapter 4
The Neutron Monitor

4.1 The history and development of neutron monitors

Chapters 2 and 3 describe the transport of cosmic rays through the heliosphere, magnetosphere and the atmosphere of the earth. This chapter describes the design of neutron monitors with which these particles are detected on earth.

When primary cosmic rays penetrate the atmosphere, extensive air showers of secondary particles are formed, as described in Chapter 2. Shea and Smart (2000) described early measurements of these secondary cosmic rays. The first routine monitoring of cosmic rays was performed with an ionisation chamber at Hafelekar, Austria, in January 1932. Another four ionisation chambers commenced operation in the 1930s: in Christchurch, New Zealand; Huancayo, Peru; Cheltenham, USA; and Godhavn, Greenland. This network of ionisation chambers operated for more than twenty years. Atmospheric secondary particles were also observed by using photographic emulsions, from 1940 – 1946. Geiger-Müller counters, together with muon telescopes, were also used (Dorman, 1974). Neher et al. (1953) described an ionisation chamber that could transmit the data gathered in flights.

Ionisation chambers record only highly energetic secondary particles produced by protons with energies > ~4 GeV (Shea and Smart, 2000). A detector was therefore developed that can record secondary particles generated by incident primaries with lower energy, as well as being relatively easy to maintain – the neutron monitor.

J.A. Simpson developed and tested the neutron monitor in 1948 – 1951, as described in Simpson (2000). He installed the first neutron monitor in Climax, Colorado, USA, in September 1951. This monitor is still operational. Figure 4.1 shows the counting rate of this monitor from 1951 to 2000.

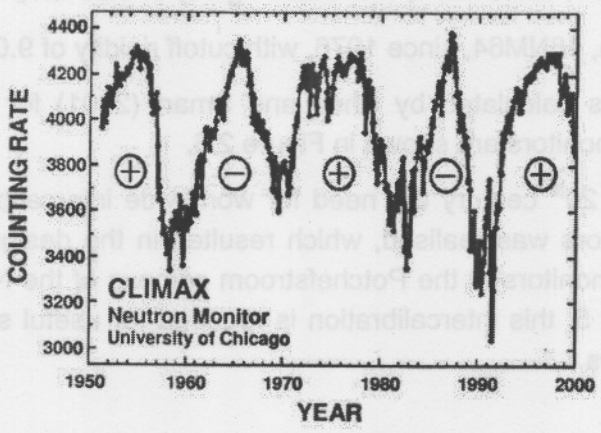

Figure 4.1: The counting rate of the neutron monitor at Climax, Colorado, USA, from 1951 to 2000. It is the longest continuously operated neutron monitor in the world. The plus and minus signs indicate the polarity of the magnetic solar cycle in the northern hemisphere. Adapted from Shea and Smart (2000).

Simpson also installed neutron monitors at Chicago, Huancayo and Sacramento Peak around 1952. Simpson's purpose with these first monitors was to prove the existence of a dynamical heliosphere and how galactic cosmic rays were modulated by it. Thereafter, neutron monitors proliferated until there was a worldwide network of 51 in 1957, used for the International Geophysical Year (IGY) from July 1957 to December 1958. These 'Simpson' neutron monitors are also called IGY monitors. According to Hatton (1971), this network made an important contribution to the present knowledge of the interplanetary environment, in particular the characteristics of the solar magnetic field, and the interaction of the cosmic rays and solar particles with this magnetic field.

Better statistical accuracy was desired. Hughes (1961, as quoted by Hatton and Carmichael, 1964) found that only 1.9% of the produced neutrons were registered. According to Hatton (1971), the counting rate of the IGY monitor was too low (~25 000/hour). A counting rate of ~10^6/hour was desired in order to improve the statistical accuracy of neutron monitor data. In 1959 a monitor station at Deep River (Canada) used larger tubes, resulting in a much higher counting rate (~750 000/hour). This was the beginning of the design of the super neutron monitor, the NM64. Hatton and Carmichael (1964) did some tests in 1960 to find the optimum design for this NM64. This larger and standard neutron monitor has been used since the International Quiet Sun Year (IQSY), in 1964 – 1965.

Since 1970 cosmic ray monitor stations have been using mainly NM64 neutron monitors, but several are still using the IGY, like here at Potchefstroom. Shea and Smart (2000) provide a list of operating neutron monitors, as well as closed ones. The data of these monitors can be used for long-term studies of cosmic rays. According to McDonald (2000), there were 59 neutron monitor stations still in operation around the world at that time, covering a wide range of geomagnetic cutoff rigidities, altitudes and viewing directions.

The Unit for Space Physics at the Potchefstroom campus of the North-West University has four monitors under its authority, namely at

- Hermanus, 12NM64, since 1957, with cutoff rigidity of 4.45 GV;
- Sanae, Antarctica, 15NM64, since 1964, with cutoff rigidity of 0.75 GV;
- Potchefstroom, IGY, since 1971, with cutoff rigidity of 6.85 GV;
- Tsumeb, Namibia, 18NM64, since 1976, with cutoff rigidity of 9.06 GV.

The cutoff rigidity values calculated by Shea and Smart (2001) for 1995 are used. The counting rates of these monitors are shown in Figure 2.6.

Towards the end of the 20th century the need for worldwide intercalibration of these large, stationary neutron monitors was realised, which resulted in the design and construction of two calibration neutron monitors at the Potchefstroom campus of the North-West University. As described in Chapter 5, this intercalibration is required for useful spectral studies of the modulation of cosmic rays.

4.2 Design of neutron monitors

A neutron monitor consists of a gas-filled proportional counter surrounded by a moderator, lead producer and reflector. Neutrons are moderated by low atomic number materials and

are multiplied in lead surrounding the counters. Many experiments have been done to find the optimum design of neutron monitors, first for the IGY and then the NM64. The function and operation of each component will be described below. The following general background on neutron monitors was obtained from Le Couteur (1949), Tongiorgi (1949), Rossi (1952), Hatton and Carmichael (1964), Egelstaff (1965), Harrison (1966), Hayakawa (1969), Hatton (1971), Dorman (1974), Wilson (1976), Krane (1988), Friedlander (1989 and 2000), Simpson (2000), Stoker *et al.* (2000), K.R. Pyle (private communication) and lansce.lanl.gov/overview/neutrons.htm.

4.2.1 Gas-filled counters

The counters in question have to detect mainly neutrons. However, free neutrons cannot ionise or excite atoms. They interact with matter primarily through collision (by scattering or absorption) with other atoms or nuclei. Therefore, the products of a nuclear reaction induced by neutrons are recorded by detecting the charged particles produced in this reaction. The following concepts are relevant for these counters:

The *microscopic cross-section* (σ) of a nucleus is the probability of a neutron interacting with a nucleus. In other words, it is the effective area the nucleus presents to the neutron (or bombarding particle) for the particular reaction. This cross-section depends on the kind of nucleus, as well as the energy of the neutron.

Many radiation detectors use an electric field to separate and count the ions or electrons formed. A simple type of detector is the *ionisation chamber*, which functions like a parallel-plate capacitor, in which the region between the plates is filled with a gas. The applied electric field keeps the ions and electrons from combining. When ionisation occurs in the gas, due to the passage of charged particles, a cloud of electrons drifts toward the positive plate, while the positive ions drift toward the negative plate. A resulting current, that can be measured, occurs.

This ionisation chamber is omni-directional and it also yields no direct information on the kinds of particles. It has the advantage of measuring a quantity proportional to the energy per unit area impinging onto the atmosphere at the location where it is used. It is light in weight and simple to construct.

To use a *gas-filled detector* to observe pulses, considerable amplification must be applied. When the voltage is increased, the accelerated electrons can make inelastic collisions and can create new ionised atoms. This rapid amplification through production of secondary ionisations is called an avalanche. Although there are a large number of secondary events for each original ion, the *proportional counter* operates such that the number of secondary events is proportional to the number of primary events. The output pulse height is proportional to the energy deposited by the radiation through primary ionisation.

The *detection efficiency* (ε) of neutrons depends on their energies. The efficiency of detection of neutrons of energy E by a detector of thickness d, containing N atoms per unit volume (number density) of a neutron absorber for which the absorption cross-section is σ at the given neutron energy, is

$$\text{Efficiency} = f[1-\exp(-N\sigma d)]. \qquad (4.1)$$

The term $[1-\exp(-N\sigma d)]$ gives the fraction of incident neutrons that is absorbed in the detector, and f indicates the fraction of these interactions that results in an output pulse from the detector. In gas-filled counters the factor f is close to unity and the detection efficiency is limited by the number of absorbing nuclei in the path of the neutron travelling through the detector.

Neutron energies are classified as follows:

- Cold neutrons: $E < 0.025$ eV
- Thermal neutrons: $E \approx 0.025$ eV
- Epithermal neutrons: $E \sim 1$ eV
- Slow neutrons: $E \sim 1$ keV
- Intermediate neutrons: $E \approx 100 - 500$ keV
- Fast neutrons: $E > 500$ keV

Cold, thermal and epithermal neutrons exhibit a cross-section for nuclear interaction that is proportional to $1/E^{1/2}$ or $1/v$, the neutron speed.

When high-energy neutrons penetrate a medium, scattering reduces the speed of the neutrons. After a number of collisions with nuclei, the energies of the neutrons are close to *thermal energies*, i.e. about 0.025 eV at 20°C.

Detectors for slow and thermal neutrons are based on the (n,p) and (n,α) reactions. The isotope ^{10}B is commonly used by an ionisation chamber or a proportional counter filled with BF_3 gas. The exothermic reaction is, as given by Hatton (1971), is

$$^{10}B + n \rightarrow {}^{7}Li^{*} + {}^{4}He \rightarrow {}^{7}Li + {}^{4}He + 0.480 \text{ MeV } (94\%) \qquad (4.2)$$

or

$$^{10}B + n \rightarrow {}^{7}Li + {}^{4}He + 2.78 \text{ MeV } (6\%). \qquad (4.3)$$

Reaction (4.2) indicates that ^{7}Li is usually left in an excited state, indicated as $^{7}Li^{*}$, and reaction (4.3) shows that in the remaining 6% the ^{7}Li is left in ground state.

Natural boron consists of about 20% of the isotope ^{10}B and 80% of ^{11}B. The isotope ^{10}B has a large cross-section, 3820 barns for thermal (0.025 eV) neutrons (Figure 4.2), while it is only 755 barns for natural boron. Therefore, enriching the gases with ^{10}B, increases the efficiency of the detector (1 barn = 10^{-24} cm^2).

Neutron monitors use proportional counters, usually filled with boron trifluoride (BF_3), enriched with 96% ^{10}B, with pressure of 0.25 atmospheres. When a neutron reacts with a ^{10}B-nucleus, the energetic helium and lithium ions absorb electrons from the neutral atoms in the counter and produce a charge. A thin wire goes through the centre of each counter along its axis, surrounded by the gas, and is connected to an amplifier and discriminator. The charge is recorded as a count through the amplifier.

In proportional counters the amplitude of γ-ray induced pulses is considerably less than the amplitude of pulses from neutron detection. Pulse height discrimination techniques can be used to detect mainly the neutrons.

About 6% of the evaporated neutrons are captured by the ^{10}B-atoms. There are also events from which more than one neutron is captured in the counters. Therefore, if the dead time of registration is much smaller than the average lifetime of a neutron, a significant amount of cosmic rays can cause more than one event. The average lifetime of the neutrons is about 300 μs, while the dead time is about 20 μs. The neutrons will therefore be registered individually in general and the counting rate will be larger than the occurrence of statistically independent cosmic ray events, according to Hatton and Carmichael (1964).

As mentioned in Section 4.1, the NM64 was developed at the Deep River cosmic ray station in 1959, by using various large $^{10}BF_3$ proportional counters. These counters are called the 'BP28 Chalk River Neutron Counters', because they were developed in Chalk River, Canada. The counters were redesigned in 1962 by using thin stainless steel instead of heavy copper tubes. Absorption in the sides of the tubes decreased the loss of electrons, and the efficiency of the monitor was improved. The effective diameter of the IGY counters is 0.225 of the average mean free path length of thermal neutrons in ^{10}B, where it is 0.375 for the NM64 counters. (The mean free path is the average distance that a neutron travels in a material between interactions.) As a result of these combinations, Hatton and Carmichael (1964) found that the NM64 counter is 1.37 times more efficient than the IGY counter.

Hatton and Carmichael (1964) did some tests with the gas pressure in the counters to determine how the counting rate of an NM64 varies with this pressure. They found that the counting rate increased by 50% when the gas pressure doubled without an inner moderator, while it increased by only 35% with an inner moderator. Their conclusion was that a pressure of 20 cm Hg = 0.27 atmospheres at 22°C is adequate, because a low-pressure $^{10}BF_3$ counter functions better and retains a reasonably low operating voltage.

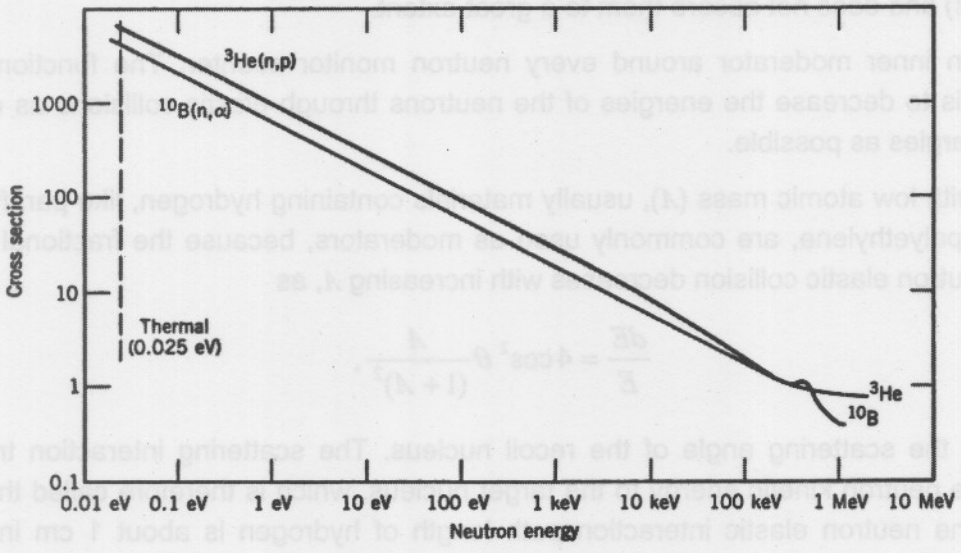

Figure 4.2: The neutron cross-sections for ^{10}B (n,α) and ^3He (n,p). Adapted from Krane (1988).

Since 1990 ^3He counters have also been used in neutron monitors. These counters have not been used earlier, due to the relatively high cost of the gas. Currently, the cost is comparable

with that of $^{10}BF_3$ gas (Stoker *et al.*, 2000) and ^{3}He counters have a simpler construction. The exothermic reaction for the counting of neutrons with ^{3}He counters is

$$^3\text{He} + \text{n} \rightarrow {}^3\text{H} + \text{p} + 0.765 \text{ MeV}. \qquad (4.4)$$

The Q-value of ^{3}He is smaller than that of ^{10}B but the ^{3}He cross-section is larger (σ = 5330 barns for thermal neutrons), as can be seen in Figure 4.2.

^{3}He gas in a proportional counter has the advantage that a high pressure of helium can be used with modest voltages, less than 1500 V, on the electrode. The neutron absorption of ^{3}He is greater than $^{10}BF_3$ gas for the same length and pressure, e.g. being 75% for ^{3}He compared to 62% for $^{10}BF_3$ for 10 cm of each gas at 1 atmosphere pressure, with 0.025 eV neutrons, according to Egelstaff (1965). ^{3}He filled proportional counters can be operated satisfactorily at 3 – 7 atmospheres and therefore can have a much higher efficiency per unit volume than the usual large $^{10}BF_3$ counters (Stoker *et al.*, 2000). These ^{3}He counters are commercially available, e.g. the model LND25373, designed by J.M. Clem at Bartol.

Although counters based on above-mentioned reactions (4.2 – 4.4) are most efficient for thermal neutrons due to the $1/E^{1/2}$ and $1/v$ dependence of the cross-section, they can also detect faster neutrons by surrounding these counters with materials that contain hydrogen, like paraffin wax or polyethylene. Elastic collisions of the neutrons with the hydrogen nuclei reduce the neutron energy to thermal values, where the counters are efficient.

4.2.2 Moderators

The process of reducing the neutron energy to thermal values is called *thermalisation*, or *moderation*. The material that thermalises or moderates the neutrons is called a *moderator*. A good moderator reduces the speed of the neutrons in a small number of collisions (scatterings) and does not absorb them to a great extent.

There is an inner moderator around every neutron monitor counter. The function of the moderator is to decrease the energies of the neutrons through elastic collisions as close to thermal energies as possible.

Materials with low atomic mass (A), usually materials containing hydrogen, like paraffin wax, water and polyethylene, are commonly used as moderators, because the fractional energy loss per neutron elastic collision decreases with increasing A, as

$$\frac{dE}{E} = 4\cos^2\theta \frac{A}{(1+A)^2},$$

where θ is the scattering angle of the recoil nucleus. The scattering interaction transfers some of the neutron kinetic energy to the target nucleus, which is therefore called the recoil nucleus. The neutron elastic interaction path length of hydrogen is about 1 cm in typical moderator materials, for neutron energies ≤ 1 MeV. The average number of elastic collisions required to thermalise a 4 MeV neutron is about 20 for paraffin.

The average thickness of the paraffin moderator around one counter of the standard IGY is 3.7 cm, while it is 2.0 cm for the polyethylene moderator of the NM64 (see Table 4.1).
A counter with its moderator is called a counter assembly.

As already mentioned, Hatton and Carmichael (1964) determined the efficiency of a 6NM64 to record a thermal neutron as ~6%. Due to this low efficiency for detecting evaporation neutrons, a lead producer is used to surround the counter assembly to increase the production of neutrons.

4.2.3 Lead producer

When energetic subatomic particles, such as protons and neutrons, strike or interact with the nucleus of an atom, such as in lead, spallation occurs, and several particles, including many neutrons, are ejected from the nucleus, in two stages. Firstly, the incident particle induces nucleon-nucleon collisions with the nucleons of the target nucleus. These particles may escape from the nucleus, or may interact again. Thus a chain of interactions, a so-called cascade shower, may develop inside the nucleus. These collisions lead to the prompt emission of a few neutrons and protons, called *prompt* neutrons and protons, because they are released almost instantaneously (~10^{-13} s) during the reaction. A fraction of the kinetic energy of the incoming particle will be transferred to the target nucleus as excitation energy, e.g. a 1 GeV proton deposits on average 200 MeV in the target nucleus. Leaving the nucleus in a highly excited state, the remainder of the energy will be shared between the prompt emitted nucleons (> 20 MeV) that escape the nucleus.

Secondly, the highly excited nuclei produced in the collisions will de-excite by emitting low-energy *evaporation* neutrons and protons. Neutron evaporation is favoured because evaporated protons need extra energy to overcome the Coulomb barrier of heavy nuclei. The average energy of the evaporated nucleons is determined mainly by the temperature reached by the residual nucleus in the collisions, i.e. by the amount of energy that remains in the nucleus after the initial stage of disintegration is completed, and will be in the order of 10 MeV. This second reaction of producing evaporation neutrons at lower energy is the main contributing factor to the multiplication and moderation of the neutrons.

Hatton (1971) named two important internal instrumental properties that should be known about the detection of evaporation neutrons in a specific neutron monitor:

- the absolute efficiency for detecting evaporation neutrons;
- the time distributions for their detection.

These properties depend on the geometry and constituents of the neutron monitor, but are independent of the geographical location. The detection efficiency of the two monitors is described in Section 4.3.2.

The producer of the IGY consists of rectangular lead bricks, while a lead cylinder surrounds the counter assembly of the NM64, with additional lead between the cylinders. Lead is chosen, because an element with a high atomic mass, A, provides a large nucleus target for producing evaporation neutrons. Such a producer has a neutron production rate per unit mass that is about $\propto A^{0.7}$ for the incident energy range of 100 – 700 MeV, and slowly decreasing with increasing energy, according to Clem and Dorman (2000). Lead also has a relatively low thermal absorption cross-section, about 0.17 barn.

The average number of neutrons simultaneously produced by a single neutron, with energies lying in the energy range to which the detector is sensitive, is called the *multiplicity (ν)*.

The average number of evaporated neutrons produced in the lead depends on the energy of the incident neutron. Bieber *et al.* (2001b) described the produced multiplicity roughly as a power law:

$$\nu_n = 25\, E^{0.4} \text{ (GeV)},$$

where ν_n is the average number of evaporation neutrons. Therefore, a 100 MeV incident neutron produces ≈ 10 evaporation neutrons in the lead. Hatton (1971) found that secondary nucleons with typical energy of 200 MeV produce about 10 evaporation neutrons on average in the monitor. This multiplicity is discussed in detail in Chapter 8.

4.2.4 The reflector

It is necessary to shield detectors from stray thermal neutrons and from the environment. Thus, a reflector surrounds the lead producer of a neutron monitor, absorbing and reflecting unwanted low-energy neutrons from the surroundings. The purpose of the reflector is also to moderate the energies of the neutrons it reflects. Therefore, the reflector consists of hydrogenous material for moderation, e.g. paraffin wax or polyethylene.

The reflector is a simple rectangular box in both the IGY and NM64. A thickness of 30.5 cm paraffin wax is used for the IGY. For the NM64 Hatton and Carmichael (1964) performed various tests, with different compositions of lead for the producer and paraffin wax around three counters, to find the optimum design for a larger neutron monitor. A lead and paraffin wax monitor with 24 counters was built in Deep River in 1961. An important development was the use of polyethylene instead of paraffin wax in 1962 for the moderator around the counters, as well as for the reflectors. A reflector of polyethylene is a fixed structure that is much easier to install than a reflector of paraffin wax. A thickness of 7.5 cm polyethylene is recommended for the reflector, equivalent to about 8 cm of paraffin wax. The main reason for using thinner polyethylene is the relatively high cost. Hatton and Carmichael (1964) showed experimentally that this thickness of polyethylene is adequate for reflecting neutrons produced in the monitor, because the diffusion length of thermal neutrons in polyethylene is 2.4 cm (Hatton, 1971), and only a negligible number of reflected neutrons moderated in the reflector will diffuse back to the counters.

4.3 The configuration and detection efficiency of the IGY and NM64 monitors

4.3.1 The configuration of the IGY and NM64 monitors

The first 6NM64 was built according to specifications, and became available in 1963. Figure 4.3 shows the structure of a 6NM64, designed and constructed for the IQSY in 1965, as described by Hatton and Carmichael (1964) and Hatton (1971). Simpson's 12-counter IGY is shown in the left panel. Both the counters of the NM64 and the IGY are filled with $^{10}BF_3$ gas.

In Table 4.1 a 6-counter unit of an NM64 is compared with a 12-counter IGY. The two types of counters used in NM64s are also compared. This table is compiled from Hatton and Carmichael (1964), Pyle *et al.* (1999), Stoker *et al.* (2000), and the specifications from the company Lnd, Inc.

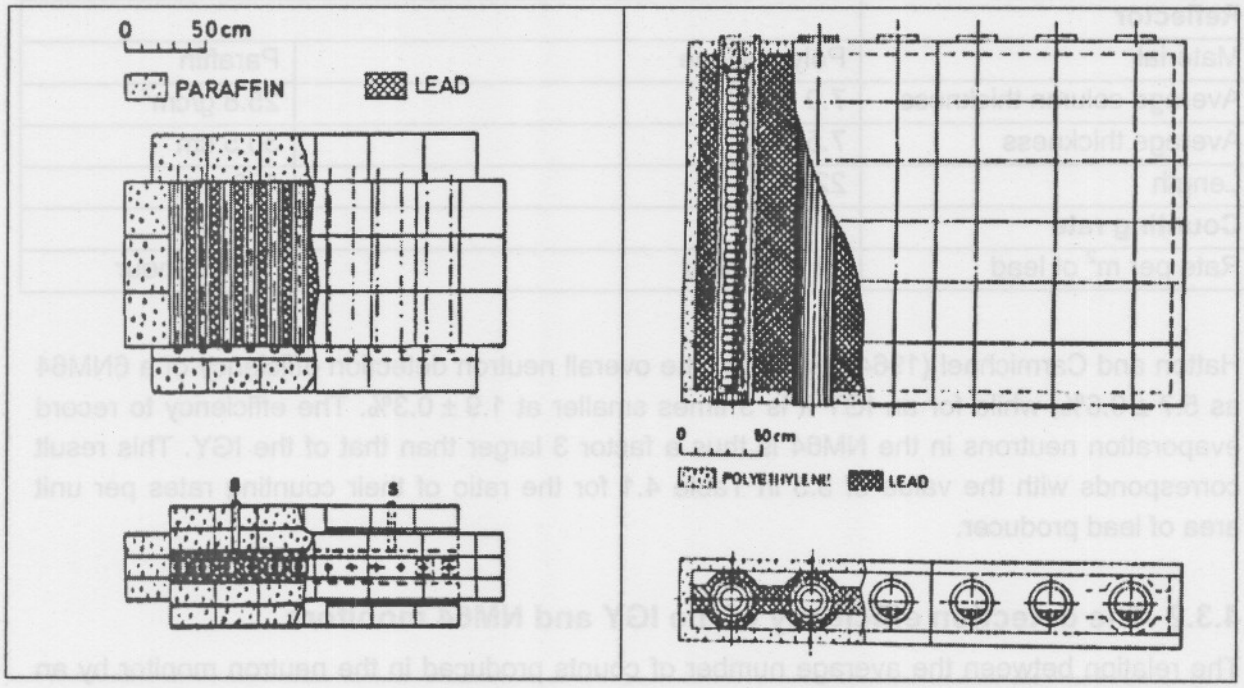

Figure 4.3: The left panel is a sketch of the Simpson IGY neutron monitor with 12 counters. The right panel presents the 6NM64 super neutron monitor, described in Hatton and Carmichael (1964) and Hatton (1971). Adapted from Stoker *et al.* (2000).

Table 4.1

	6NM64	6NM64	Standard IGY
Counter			
Type	BP28	LND25373	NW G-15-34A
Number	6	6	12
Diameter	14.8 cm	4.9 cm	3.8 cm
Spacing	50.0 cm	50.0 cm	15.2 cm
Effective Length	191 cm	190.8 cm	86.4 cm
Gas	$^{10}BF_3$	97% ^3He + 3% CO_2	$^{10}BF_3$
Pressure	200 mm Hg	3040 mm Hg	450 mm Hg
Operating voltage	2800 V	1300 V	1950 V
Thermal neutron absorption path length	41.0 cm	1.9 cm	18.2 cm
Moderator			
Material	Polyethylene		Paraffin
Average column thickness	1.84 g/cm^2		2.95 g/cm^2
Average thickness	2.0 cm		3.7 cm
Producer			
Material	Lead		Lead
Average column thickness	156 g/cm^2		153 g/cm^2
Length	207 cm		102 cm
Projected top area	6.21 m^2		1.9 m^2

Reflector		
Material	Polyethylene	Paraffin
Average column thickness	7.0 g/cm^2	25.8 g/cm^2
Average thickness	7.5 cm	30.5 cm
Length	222 cm	168 cm
Counting rate		
Rate per m^2 of lead	42 000 /hour	12 800 /hour

Hatton and Carmichael (1964) estimated the overall neutron detection efficiency of a 6NM64 as 5.7 ± 0.6%, while for an IGY it is 3 times smaller at 1.9 ± 0.3%. The efficiency to record evaporation neutrons in the NM64 is thus a factor 3 larger than that of the IGY. This result corresponds with the value of 3.3 in Table 4.1 for the ratio of their counting rates per unit area of lead producer.

4.3.2 The detection efficiency of the IGY and NM64 monitors

The relation between the average number of counts produced in the neutron monitor by an incident particle and the energy of that particle, is given by Hatton (1971):

$$\overline{n}(E) = P(E)\overline{\nu}(E)\overline{\varepsilon}(E),$$

where

$\overline{n}(E)$ = the average number of counts for an incident nucleon,

$P(E)$ = the probability of the incident particle penetrating the reflector and interacting in the producer of the monitor,

$\overline{\nu}(E)$ = the average number of evaporation neutrons produced by an interaction,

$\overline{\varepsilon}(E)$ = the average efficiency for detecting the evaporation neutrons.

Clem (1999) determined the detection response of the neutron monitor for secondary particles at ground level by using a Monte Carlo simulation. He used the 3-dimensional Fluka particle transport code, together with programs to simulate the proportional tube and electronics response. Standard dimensions and compositions for the geometry of an IGY and NM64, as described in Table 4.1, were used. The total number of counts per beam luminosity, i.e. the number of beam particles per unit area, was determined for different incident beam angles, initial energies and particles species. These simulations were also discussed by Clem and Dorman (2000).

Clem simulated the detection response of an NM64 with $^{10}BF_3$ BP28 and ^{3}He counters, for vertically incident neutrons and protons, as shown in Figure 4.4. This figure shows that the calculated response for the two counters is very similar. Based on these calculations, the ^{3}He counters were designed to have similar performance as the $^{10}BF_3$ BP28 counters. This was confirmed by Pyle *et al.* (1999), when he replaced one $^{10}BF_3$ counter with a ^{3}He counter on one of their annual sea level latitudinal surveys, in 1998/9. They determined experimentally that the efficiency and the energy (latitudinal) response of this counter are nearly identical to

that of the $^{10}BF_3$ BP28 detector, and that the ^3He counter can be used just as well in a standard NM64.

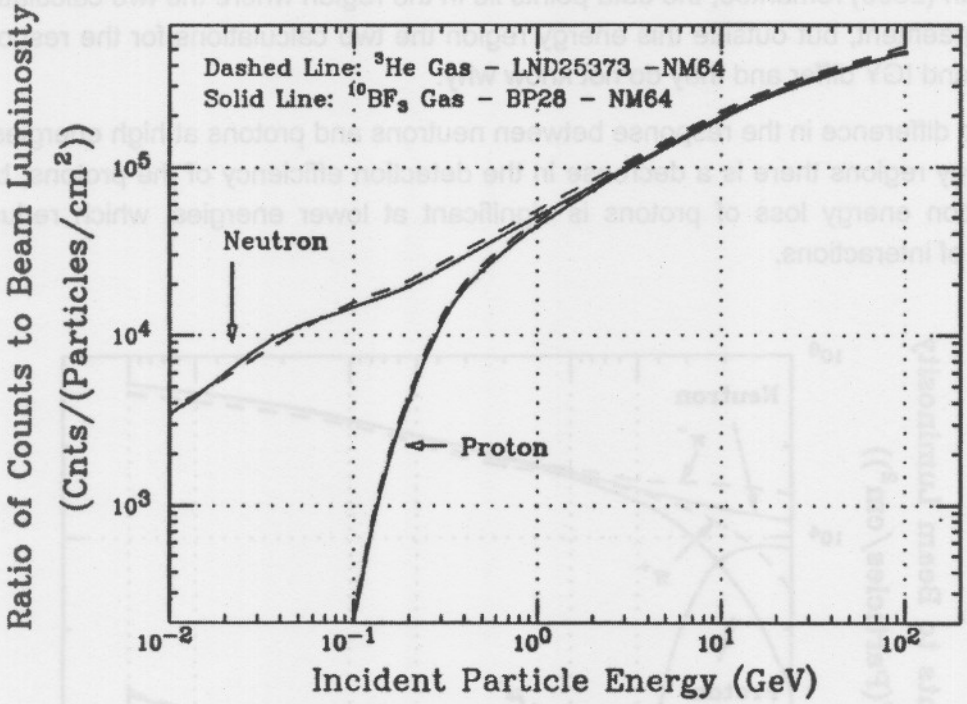

Figure 4.4: The calculated detection efficiency of an NM64 with ^3He and $^{10}BF_3$ counters. Adapted from Clem (1999).

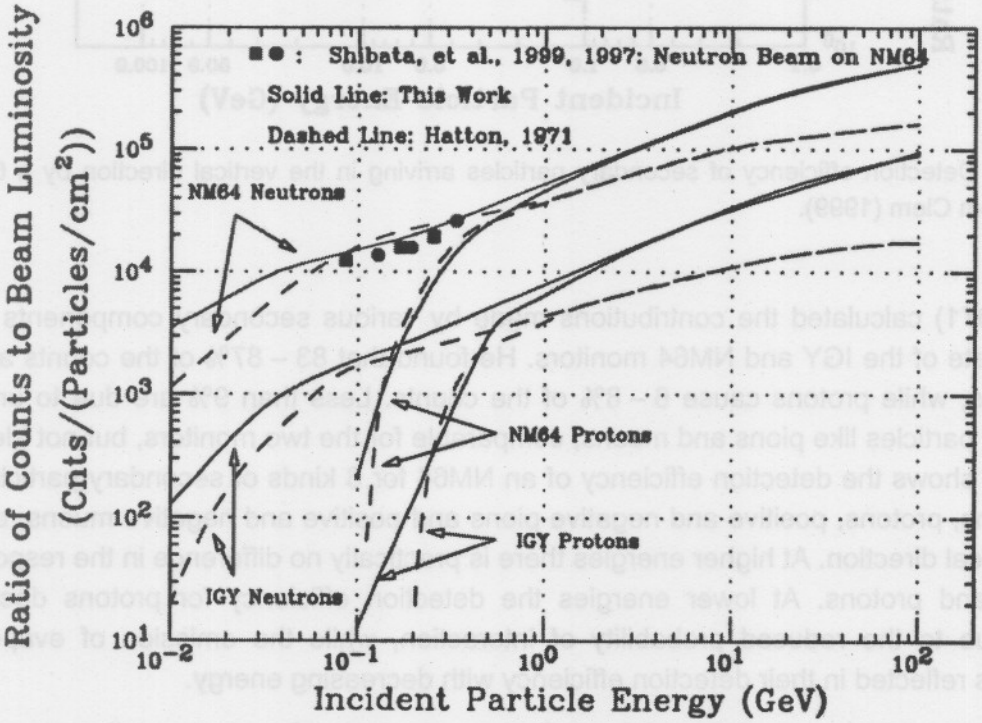

Figure 4.5: The detection efficiencies of the NM64 and IGY neutron monitors are compared for protons and neutrons. Adapted from Clem (1999).

Figure 4.5 compares the detection efficiencies for protons and neutrons in an NM64 and IGY. The dashed lines are the calculations of Hatton (1971). The solid lines indicate the simulation by Clem (1999). The different responses of the two monitors can clearly be seen. As Clem and Dorman (2000) remarked, the data points lie in the region where the two calculations are in good agreement, but outside this energy region the two calculations for the responses of the NM64 and IGY differ and they do not know why.

There is no difference in the response between neutrons and protons at high energies. In the lower energy regions there is a decrease in the detection efficiency of the protons, because the ionisation energy loss of protons is significant at lower energies, which reduces the probability of interactions.

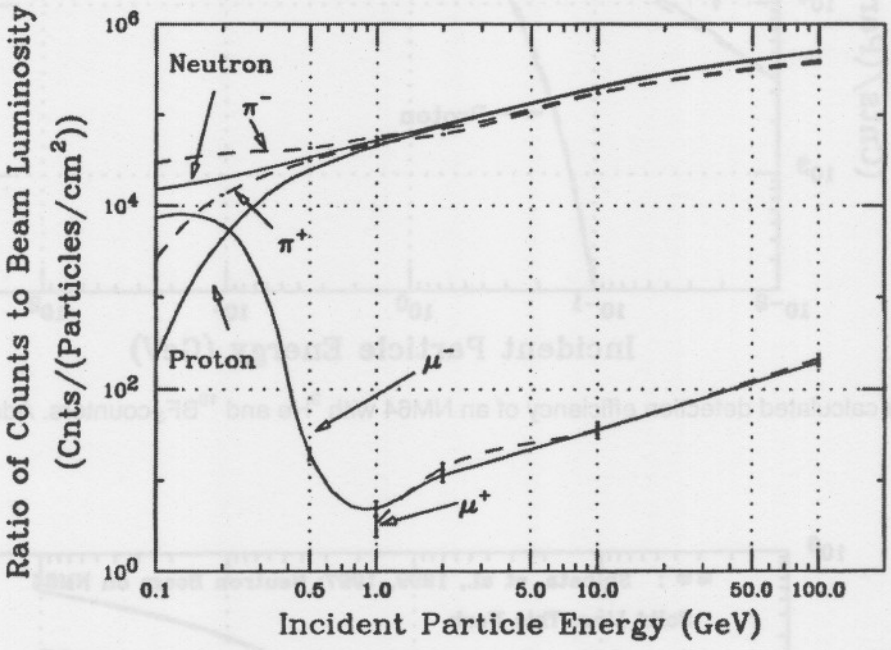

Figure 4.6: Detection efficiency of secondary particles arriving in the vertical direction by a 6NM64. Adapted from Clem (1999).

Hatton (1971) calculated the contributions made by various secondary components to the counting rate of the IGY and NM64 monitors. He found that 83 – 87% of the counts are due to neutrons, while protons cause 6 – 8% of the counts. Less than 9% are due to unstable secondary particles like pions and muons, comparable for the two monitors, but not identical. Figure 4.6 shows the detection efficiency of an NM64 for 6 kinds of secondary particles, i.e. for neutrons, protons, positive and negative pions and positive and negative muons, arriving in the vertical direction. At higher energies there is practically no difference in the response to neutrons and protons. At lower energies the detection efficiency for protons decreases sharply due to the reduced probability of interaction, while the emission of evaporation neutrons is reflected in their detection efficiency with decreasing energy.

In Chapter 6 these characteristics of the various components of neutron monitors are used to construct a lightweight mobile neutron monitor, to be used for the intercalibration of the worldwide neutron monitor network.

Chapter 5
Differential Response Functions and Intercalibration of Neutron Monitors

5.1 Network of neutron monitors

Since the start of neutron monitor work, many neutron monitors had been built at different places in the world. The number of stations had grown to ~100 by the end of the 1960s, and today about half of them are still operating.

Moraal *et al.* (2000) gave three main categories of observations with these neutron monitors:

- Anisotropic studies, which require neutron monitors with well-defined and narrow cones of acceptance for charged particles, covering all directions as evenly as possible;
- Solar neutron measurements, which require neutron monitors at high altitude in equatorial regions;
- Spectral measurements, which require an optimal distribution along cutoff rigidities.

This chapter is mainly devoted to this third category.

5.1.1 Anisotropic studies

The advantage of the neutron monitors in the network is their high statistical accuracy due to their high counting rate, which allows them to observe small events that are not possible with spacecraft. Neutron monitors can detect anisotropies, but that depends on their directional sensitivity. Moraal *et al.* (2000) described the two factors in determining this sensitivity. Firstly, the vertical direction is the most favourable due to atmospheric absorption. Secondly, the asymptotic cone of acceptance, as described in Chapter 3, differs according to the position of the neutron monitor. Neutron monitors with the narrowest cones of acceptance are the best anisotropy recorders.

Both Forbush decreases and SEP increases are inherently anisotropic in nature. Bieber and Evenson (1995) stated that a neutron monitor network at high geographic latitudes, and consequently at low cutoff rigidity ($\leq$ 2 GV), is essential to view these directional events, due to their uniform energy responses and well-defined asymptotic cones of acceptance. Therefore, Spaceship Earth (see Chapter 3) is used to investigate these particles.

5.1.2 Solar neutron measurements

Solar neutrons from solar flares are not affected by magnetic fields. Pyle (1993) gave a few reasons why an equatorial high-altitude neutron monitor has several advantages for direct detection of these neutron events. The main criterion is to have the minimum amount of absorbing atmosphere above the neutron monitor in the direction of the sun. He calculated the probability that neutron monitors in the network will be able to observe these neutrons, and found that only 14 neutron monitors view towards the sun through less than one

atmosphere for more than 5% of the time, while no monitor does it for more than 30% of the time.

Usoskin *et al.* (1997) discussed the use of the world's neutron monitor network to detect these high energetic solar neutrons in detail. They showed that the existing neutron monitor network can be used for continuous monitoring of intense sporadic solar neutron events. They mentioned that there is, however, no practical way to calibrate the neutron monitor network.

5.1.3 Spectral analysis

One aspect of neutron monitor work that still has to be developed is spectral studies of modulation effects, as is done with spacecraft data, e.g. as shown in Figure 2.11. In order to obtain such spectra, the worldwide neutron monitors must be optimally distributed along cutoff rigidities and have to be intercalibrated, as described in Section 5.3. Since such an intercalibrated network does not yet exist, the traditional way to obtain spectra has been to conduct latitudinal surveys, as described in this chapter.

5.2 Summary of latitudinal surveys

Since the 1930s, various balloon flights, sea and land voyages, as well as aircraft surveys, were conducted to investigate the latitudinal dependence of cosmic rays. The most significant of these latitudinal surveys are described here.

- Twelve sea voyages were performed between Vancouver, Canada, and Sydney, Australia, on the Pacific Ocean, from 17 March 1936 to 18 January 1937. Compton and Turner (1937) described this journey. An ionisation chamber was used. The two main objectives were to obtain a precise comparison of cosmic rays in the northern and southern hemispheres, and to study their intensity at different latitudes at different seasons.
- Since 1935, balloon flights with ionisation chambers and counter telescopes had been conducted in Canada, the United States, Mexico and India, by a group at the California Institute of Technology. According to Biehl *et al.* (1949), they measured the change in intensity of cosmic rays with geomagnetic latitude at 30 000 ft pressure altitude by aircraft flights with Geiger counter telescopes and ionisation chambers, in June 1948. The aim was to investigate the penetration of ionising particles with various absorber thicknesses to obtain the ionisation of the counting rate as a function of depth below the top of the atmosphere. They obtained some knowledge about the nature of the primary radiation and the interaction of the primary particles with the matter through which they passed. Biehl and Neher (1950) described the results obtained of the latitudinal and longitudinal variations in cosmic ray intensity at 30 000 ft.
- From December 1947 to November 1949, Simpson (1951) performed some neutron measurements in aircraft, with $^{10}BF_3$ counters. He showed that more than 90% of the neutrons in the atmosphere are the disintegration product produced by high energetic charged primary particles with energies of ~300 MeV. He used this to show that the neutron component has a large latitudinal effect.

- In 1951 Neher *et al.* (1953) performed 28 successful (simultaneous) balloon flights, using a newly developed ionisation chamber, to determine the fluctuations and latitudinal effect at high latitudes and altitudes. The balloons went up to 90 000 ft.
- Simpson (1954) conducted latitudinal surveys with a $^{10}BF_3$ counter surrounded by paraffin with a cadmium shield, using a jet aircraft, in the period 1950 – 1952.
- In 1954 Meyer and Simpson (1955) conducted several latitudinal surveys at aircraft altitudes. They found a significant increase in the intensity of particles at low rigidities between 1948 and 1954.
- Rose *et al.* (1956) presented results of cosmic ray measurements at sea level from the Arctic to Antarctica in 1954 – 1955. Latitudinal and longitudinal effects were measured, using a neutron monitor and a muon telescope. This survey produced the first solar minimum differential response function (described in the next section) of a neutron monitor, as reported by e.g. Moraal *et al.* (1989).
- Cosmic ray investigations were done with a shipboard neutron monitor during the International Geophysical Year, from October 1956 to January 1958 between Scandinavia and South Africa, and then from March 1958 to February 1959 between Scandinavia and Australia (Pomerantz, 1969). The primary aim of that project was to precisely locate the position of the cosmic ray equator, to determine whether the position of the cosmic ray equator depends on the level of solar activity and to determine whether time variations occur at minimum cosmic ray intensity. Sandström *et al.* (1962) investigated the so-called knee of the latitudinal effect, by using the data obtained from these journeys.
- During 1956 – 1962, the Japanese Antarctic Research Expedition carried out five sea-borne surveys along a constant route between Japan and Antarctica. Fukushima *et al.* (1963) discussed the final results of the data obtained.
- An airborne journey in a worldwide survey extending from the equator to the north and south geomagnetic poles during November 1958 to October 1960, is described by Coxell *et al.* (1965).
- Kent *et al.* (1968) obtained data from an airborne neutron monitor latitudinal survey, which was in operation between December 1964 and March 1966. They wanted information concerning the energy dependence of the average number of evaporation neutrons produced by a nucleon incident on a neutron monitor. The latitude and altitude variations of events with different multiplicities were determined.
- A German research group operated an Atlantic sea expedition from August to December 1965, and a Greenland expedition in August and September 1966, as a German contribution to the IQSY, described by Allkofer *et al.* (1969). They used an IGY neutron monitor with $^{10}BF_3$ counters.
- Carmichael *et al.* (1969a,b) described an overland cosmic ray latitudinal survey, operated in Canada, the USA and Mexico during solar maximum, in April to June 1965. Their objective was to carry out a latitudinal survey with the new NM64 during the IQSY. They used a 3NM64 neutron monitor and a muon monitor. A follow-up survey was conducted in Canada in December 1965, and a third survey in Western

USA and Hawaii in May to July 1966. This produced a second, often quoted, solar minimum differential response function.

- Investigations of latitudinal effects with cutoff rigidities in the 0 – 8 GV interval, as well as investigations of the cosmic ray nucleon component intensity variation at altitudes of 260 – 400 mb, were performed by Dorman *et al.* (1969) in January and February 1966.
- Bachelet *et al.* (1972) made a summary of five ship surveys performed by the Uppsala group in co-operation with the Bartol Research Foundation, in the period 1957 – 1965, as well as two land-borne surveys, one in Europe, performed by the Rome group in 1963, and one throughout America, by the Deep River group, in 1965. The cutoff rigidities were between 0.7 and 16.9 GV.
- Shea *et al.* (1987) described the stratospheric balloon measurements operated by the 22nd Soviet Antarctic Expedition, in late 1975 to early 1976. This sea level survey started in the north-western part of Russia, continued to Antarctica, to Buenos Aires, Argentina, down to Antarctica and back to Russia. Vertical cutoff rigidities were derived.
- From 1964 until 1989 several airborne and sea-borne latitudinal surveys were conducted by the Cosmic Ray Research Unit of the Potchefstroom University. Initially a 2IGY neutron monitor was used, but in 1969 it was changed to a 1NM64 (Raubenheimer *et al.*, 1980).

  The airborne surveys were centred at Cape Town, with a mean atmospheric depth of 307 g/cm^2 (30 000 ft), covering a cutoff rigidity interval of 1.5 – 14 GV. Accurate differential response functions were determined, which enable the study of the time dependence of cosmic ray modulation during a whole solar cycle.

  According to Van der Walt and Stoker (1977), a sea level latitudinal and longitudinal survey was conducted from South Africa, with two neutron monitors and a neutron moderated detector, during the solar minimum period, from 9 December 1975 to 4 November 1976. There were three voyages: the first one was from South Africa to the Far East, with Yokohama as the most northern port, and back, with Cape Town the most southern port. The second voyage was to North America, with New York as the most northern port, and back. The third one was to the Far East again. This survey covered a cutoff rigidity interval of 2 – 17 GV.

  Another latitudinal survey to determine cosmic ray intensities at sea level was conducted by the Cosmic Ray Research Unit of the Potchefstroom University, during the solar minimum period of 1986 – 1987. Moraal *et al.* (1989) described this survey and showed that the differential response function (see next section) for the 1986/7 solar minimum agrees well with that obtained in 1965.
- Villoresi *et al.* (2000) operated a 3NM64 on board of an Italian ship, recording neutron intensities on a sea survey between Italy and Antarctica and back, during 1996 – 1997. They used a standard 3NM64 and two bare $^{10}BF_3$ neutron counters. All meteorological effects were investigated, geomagnetic effects were evaluated and coupling functions were computed.

- Since 1994, a continuing annual neutron monitor latitudinal survey has been conducted by the Bartol Research Institute at the University of Delaware, USA, in collaboration with the Australian Antarctic Division and University of Tasmania, Australia, as described by Bieber *et al.* (2001a). These sea voyages are from Seattle, USA, to McMurdo, Antarctica, usually from November to March the next year. A standard 3NM64 is carried aboard the *Polar Sea* or the *Polar Star*, two US Coast Guard Icebreakers. Since 2002, one of the two calibration neutron monitors, described in Chapter 7, has been carried in the same room as the 3NM64. The cutoff rigidities vary from < 1 GV at McMurdo to about 15 GV in the mid-Pacific.

The primary purpose of these surveys has been to study the neutron monitor response function as derived from the latitudinal dependence. The next sections describe examples of these differential response functions.

5.3 Differential response functions

The counting rate, $N(P_c, x)$, of a neutron monitor depends on atmospheric depth or pressure and has a strong latitudinal dependence, as can be seen in Figure 5.1. This figure shows the counting rates during several of the airborne latitudinal surveys, mentioned in the previous section, as described by Stoker and Moraal (1995). Figure 5.2 shows the equivalent counting rate from the sea-borne surveys of Moraal *et al.* (1989) in 1987.

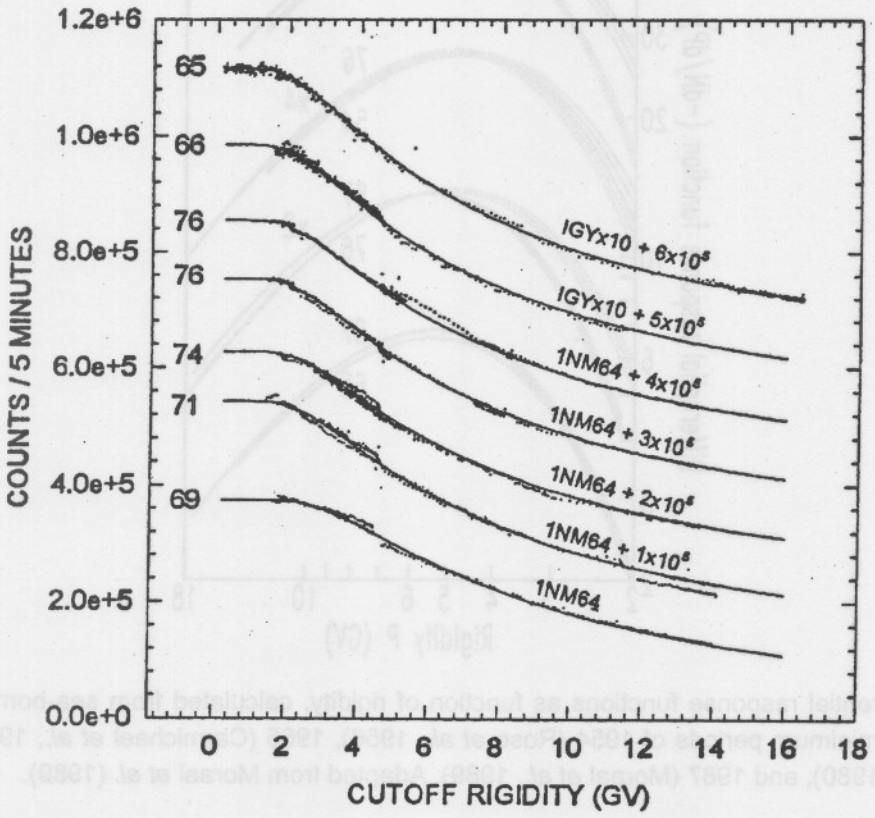

Figure 5.1: Counting rates obtained as function of cutoff rigidity, calculated from airborne latitudinal surveys. Adapted from Stoker and Moraal (1995).

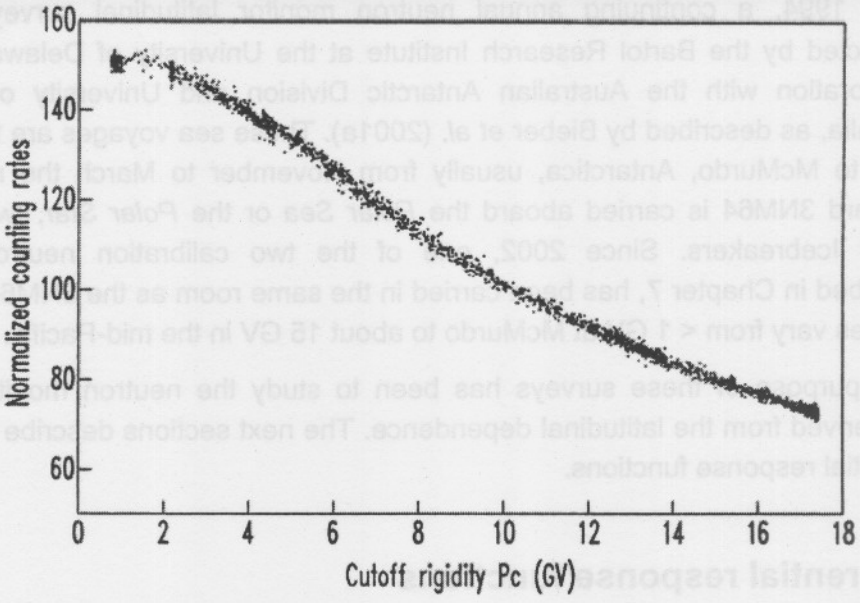

Figure 5.2: Hourly counting rates from sea-borne surveys. Adapted from Moraal *et al.* (1989).

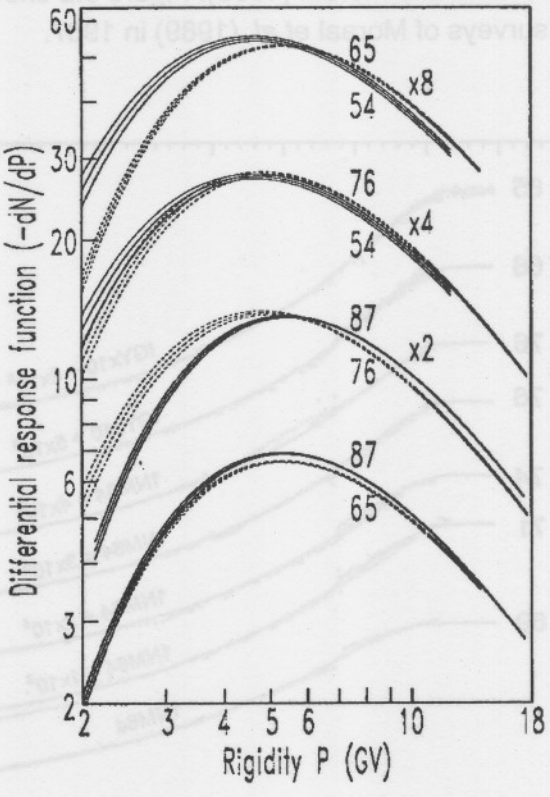

Figure 5.3: Differential response functions as function of rigidity, calculated from sea-borne surveys, during the solar minimum periods of 1954 (Rose *et al.*, 1956), 1965 (Carmichael *et al.*, 1969b), 1976 (Potgieter *et al.*, 1980), and 1987 (Moraal *et al.*, 1989). Adapted from Moraal *et al.* (1989).

When the counting rate, $N(P_c)$, is differentiated with respect to rigidity, $-dN/dP$, it is called the differential response function, as represented in Figure 5.3. This demonstrates the underlying

purpose of these differential response functions, namely to be sensitive indicators of the modulation. These differential response functions are different in consecutive solar minima, being softer during the 1954 and 1976 minima than in the 1965 and 1987 minima, as expected from drift effects in the modulation. Clem and Dorman (2000) stated that the study of response functions has improved the understanding of the ~22-year solar cycle and heliospheric effects such as Forbush decreases, as well as the behaviour of solar energetic particles (see Chapter 2).

The differential response functions are rigidity spectra of secondary particles within the atmosphere. However, spectra of cosmic rays above the atmosphere are wanted. The relation between the response function *in* the atmosphere and the observation of the intensity spectrum of primary particles, *j(P,t)*, *above* the atmosphere, is given by the so-called atmospheric yield function, *S(P, x)*:

$$-\frac{dN}{dP} = S(P,x)\,j(P,t)\,. \qquad (5.2)$$

Thus, the yield function is the number of secondary particles detected by a neutron monitor per primary particle penetrating the top of the atmosphere. There is a direct relation between the modulation, or temporal changes in the secondary spectrum, *dN/dP*, and the changes in the primary spectrum above the atmosphere. Cosmic ray primary spectra on top of the atmosphere can be deduced from neutron monitor differential response functions if the atmospheric yield function for the production of secondary particles is known.

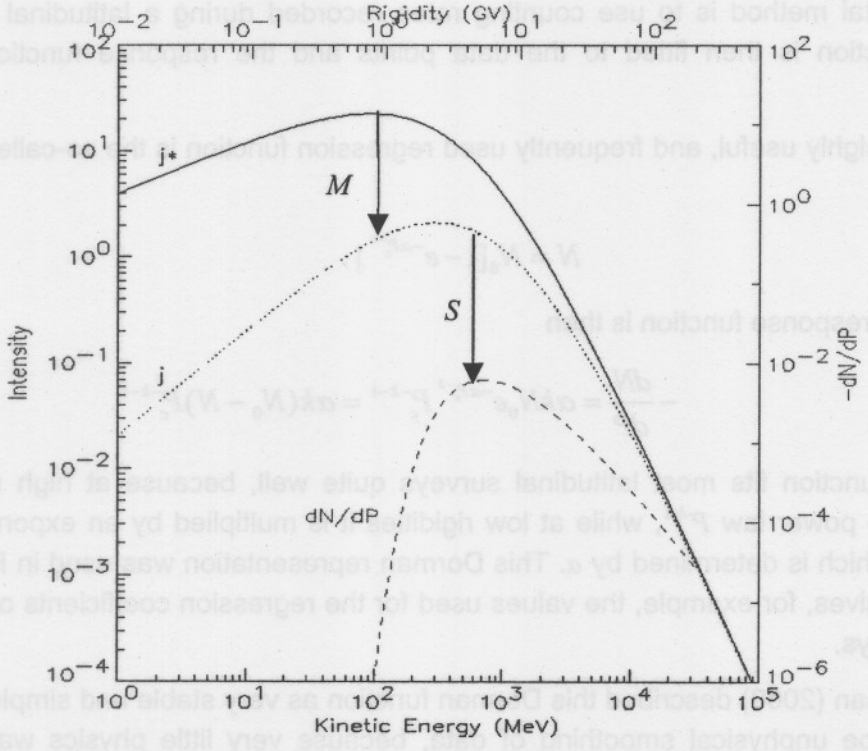

Figure 5.4: The intensity spectrum *j** modulated to spectrum *j* at 1 AU. The spectrum *j* above the atmosphere is derived from the yield function *S* and the differential response function *–dN/dP* at ground level.

Figure 5.4 shows the unmodulated intensity spectrum j^* outside the heliosphere, also called the LIS (local interstellar spectrum). This spectrum j^* is modulated to spectrum j at 1 AU, above the atmosphere, by $j = j^* M$. This intensity spectrum j *above* the atmosphere yields a differential response function, dN/dP, at ground level *inside* the atmosphere. From (5.2) it follows that

$$-\frac{dN}{dP} = S(P,x) j^* M \,. \tag{5.3}$$

Conversely, the expected counting rate from latitudinal surveys can be calculated by integrating the response functions (5.2):

$$N(P > P_c) = \int_{P_c}^{\infty} \frac{dN}{dP} dP \,. \tag{5.4}$$

5.4 Determination of differential response functions

Clem and Dorman (2000) discussed the three different categories of methods to determine a neutron monitor response function, viz. the experimental data of latitudinal survey observations (also called the parameterisation method), theoretical calculation, and the Monte Carlo simulation of cosmic ray transport through the atmosphere and neutron monitor detection efficiency. The experimental method is by far the most frequently used.

5.4.1 Experimental (parameterisation) method

The experimental method is to use counting rates recorded during a latitudinal survey. A regression function is then fitted to the data points and the response function can be calculated.

A well-known, highly useful, and frequently used regression function is the so-called Dorman function:

$$N = N_0[1 - e^{-\alpha P_c^{-k}}] \,. \tag{5.5}$$

The differential response function is then

$$-\frac{dN}{dP} = \alpha k N_0 e^{-\alpha P_c^{-k}} P_c^{-k-1} = \alpha k (N_0 - N) P_c^{-k-1} \,. \tag{5.6}$$

This Dorman function fits most latitudinal surveys quite well, because at high rigidities it approaches the power law P^{-k-1}, while at low rigidities it is multiplied by an exponential, the magnitude of which is determined by α. This Dorman representation was used in Figure 5.2, and Table 5.1 gives, for example, the values used for the regression coefficients of the 1976 and 1987 surveys.

Clem and Dorman (2000) described this Dorman function as very stable and simple to apply, but there can be unphysical smoothing of data, because very little physics was used to construct this function. Furthermore, only a limited amount of information can be obtained, such as the primary spectrum, atmospheric transport and detection efficiency.

Table 5.1

	1976	1987
N_0	150.90	148.10
α	8.953	10.068
k	0.9159	0.9519

Nagashima *et al.* (1989) obtained an alternative parameterisation of the differential response function of neutron monitors and its altitude and time dependence, by using all the then available data obtained by overseas, overland and airborne surveys, together with those obtained from space exploration. These data enabled them to decompose the response function into three terms, which is the same as (5.3) above:

- the unmodulated energy spectrum of galactic cosmic rays (j^*),
- the modulation function of cosmic rays in the heliosphere (M), and
- the yield function of neutrons in the atmosphere (S).

After an extensive study they obtained analytical expressions for j^*, S and M:

$$j^*(E)dE = \frac{\gamma_1(x)}{E^{2.585\pm0.004}}dE, \quad \text{with } \gamma_1(0) = (1.2\pm0.02)\cdot10^4, \tag{5.7}$$

$$S(T,x) = E^{0.0\pm0.1}\exp\left[-(2.2\pm2.5)\left(\frac{x}{1033}\right)^{1.62\pm0.96} - \frac{12.7\pm5.6}{(\ln E)^{0.42\pm0.21}}\left(\frac{x}{1033}\right)^{0.50\pm0.09}\right], \tag{5.8}$$

$$M(P,t) = \exp\left[\frac{\mu_1(t)}{(0.097\pm0.009)+(P/1\text{GV})^{1.02\pm0.02}}\right], \tag{5.9}$$

$$\text{with } \mu_1(t) = (1.15\pm0.02)+(14.9\pm0.8)\left\{1-\frac{I(t)}{I_{MtW}(t_{\max})}\right\}^{1.12\pm0.03}, \tag{5.10}$$

and $I_{MtW}(t_{\max})$ = 2465 counts/hour for Mt. Washington, and t_{max} = 1965,

where x is the atmospheric depth, E is in GeV, t describes time in the modulation cycle, and γ is a non-negative parameter.

Another example of using the parameterisation method to obtain response functions is shown in Figure 5.5. The dashed line indicates the measured response function for the qA positive drift cycle in 1976, and the dotted line for the qA negative drift cycle in 1987, both using the Dorman function (5.6), with the corresponding regression coefficients showed in Table 5.1. The continuous line shows the response function obtained from the solution of the Parker transport equation (2.1), at 1 AU, as transformed with the yield function (5.8) of Nagashima *et al.* (1989).

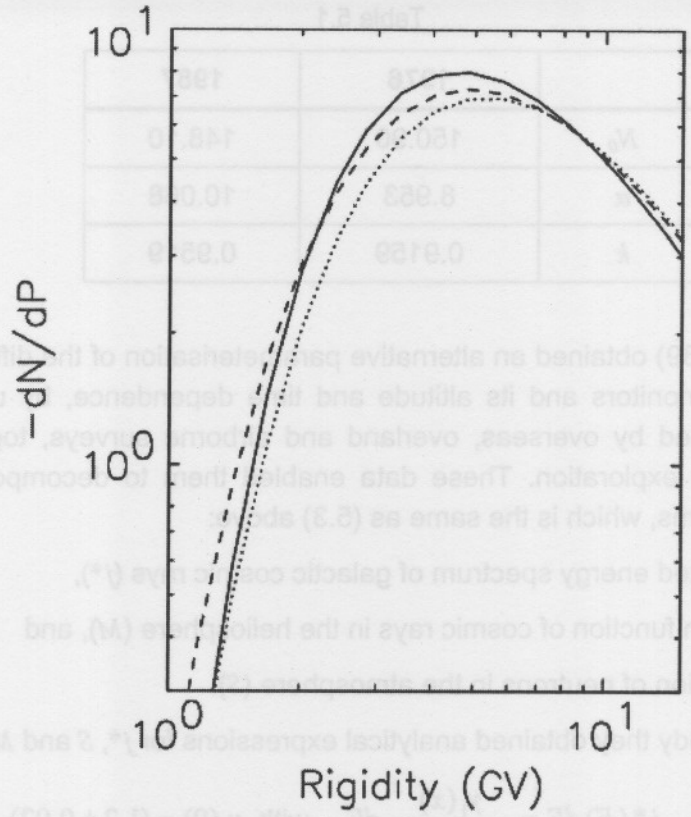

Figure 5.5: Response functions as function of rigidity, by using the Dorman function in the qA positive cycle in 1976 (dashed line) and in the qA negative cycle in 1987 (dotted line). The continuous line is obtained by using the yield function of Nagashima *et al.* (1989).

Nagashima *et al.* (1989) stated that they had demonstrated that the derivation of a reasonable response function from observation cannot be made by a single set of surveys of neutron intensity and requires the simultaneous use of data at different atmospheric depths and at different times. They mentioned further that in order to obtain a more satisfactory response function than the present, it is necessary to make simultaneous and global surveys of cosmic ray intensity at sea level, in the air and in space at least at several epochs of different solar activities.

5.4.2 Theoretical calculation method

According to Clem and Dorman (2000), the calculation method attempts to quantify all the fundamental physical mechanisms that describe the interaction and transport of cosmic rays through the atmosphere. Each of these parameters has a fundamental physical definition, but the accuracy with which these parameters are known, is limited.

An example is shown in Figure 5.6, where the theoretically calculated atmospheric yield functions $S(P_c, x)$, as in (5.2), are compared with those derived from the experimental method for different altitudes. The dashed lines indicate the theoretical curves, while the continuous lines give the yield functions obtained by using experimental methods.

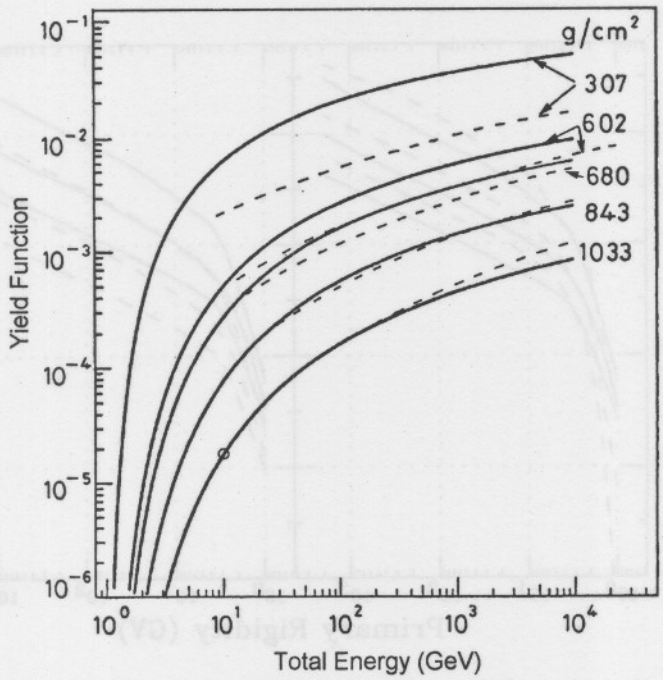

Figure 5.6: The continuous lines represent values for the yield function, determined by using parameterisation methods, while the dashed lines represent theoretical values. The theoretical and experimental curves were normalised at sea level (depth = 1033 g/cm^2) at E = 10 GeV. Adapted from Nagashima *et al.* (1989).

However, this method is not easy to perform and to reach adequate agreement with observed, parameterised differential response functions, it requires more accurate input data about nuclear atmospheric processes than are presently available.

5.4.3 Monte Carlo method

The Monte Carlo method, used by Clem (1999) and described by Clem and Dorman (2000) too, simulates the three-dimensional transport of particles through the atmosphere and the detection efficiency of a neutron monitor for energies from 0.02 eV to 20 TeV. It is not dependent on observational data or very accurate input data of fundamental transport, as with the theoretical method. It simulates a population of cascades and then records the development of each cascade in the form of particle tracks. Since there are many generations of secondary particles, it may depend quite strongly on the assumed cross sections. Spectra for different kinds of particles can be determined. These results are weighted by the detection efficiency of a neutron monitor to obtain the counting rate.

Figures 4.4 to 4.6 are examples where this Monte Carlo method was applied. Another example is Figure 5.7, where Clem (1999) used the Monte Carlo method to find the yield function from particles incident from different fixed angles with respect to the zenith at the top of the atmosphere. The continuous lines in both panels indicate the yield functions of an NM64 from primary protons at sea level. The dashed lines in the left panel are the NM64 yield function for helium nuclei, while the right panel shows that of an IGY for protons. The top curves indicate incident particles at 0°, the middle curves particles from 45° and the bottom curves that from 60° with respect to the zenith.

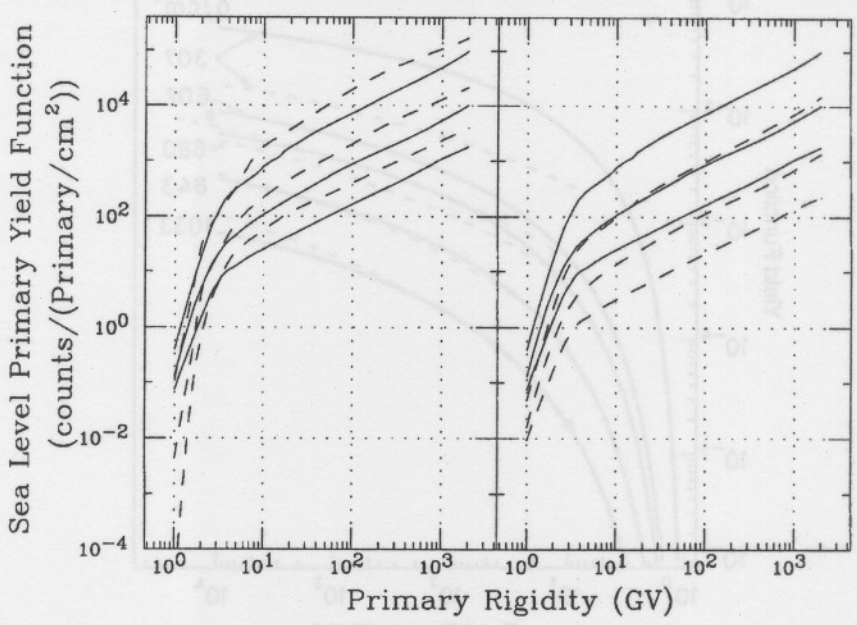

Figure 5.7: The yield function of an IGY and NM64 for primary particles. The continuous lines in both panels show the NM64 yield function for protons. The dashed lines in the left panel show the NM64 yield function for alphas, while the dashed lines in the right panel the IGY yield function for protons. Adapted from Clem and Dorman (2000).

In Figure 5.8 Clem and Dorman (2000) show a comparison of different response functions as function of cutoff rigidity at sea level during solar minimum. Some response functions were derived by using similar parameterisation methods and others by Monte Carlo simulations.

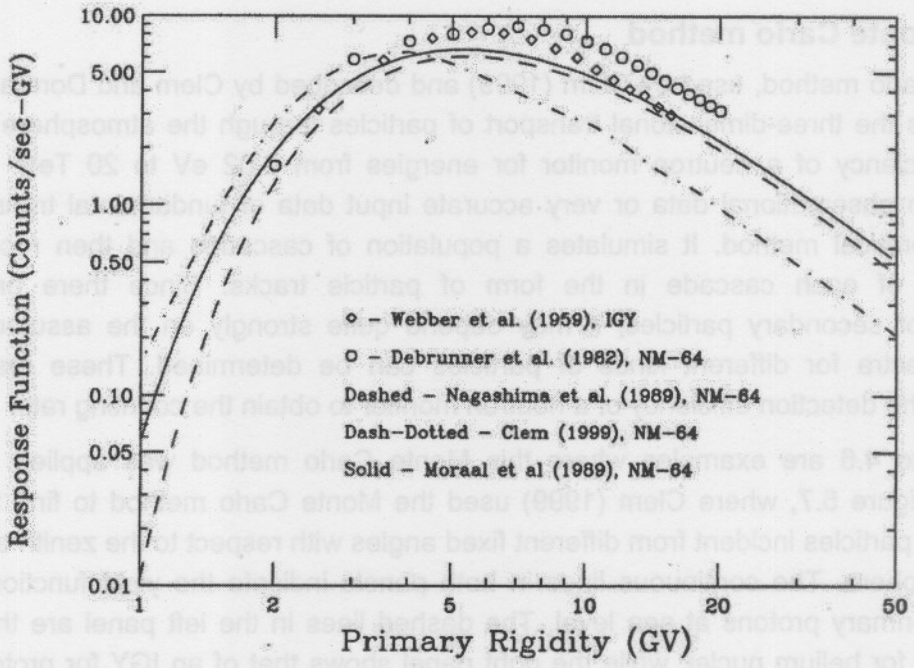

Figure 5.8: The differential response functions as function of rigidity, during solar minimum. Adapted from Clem and Dorman (2000).

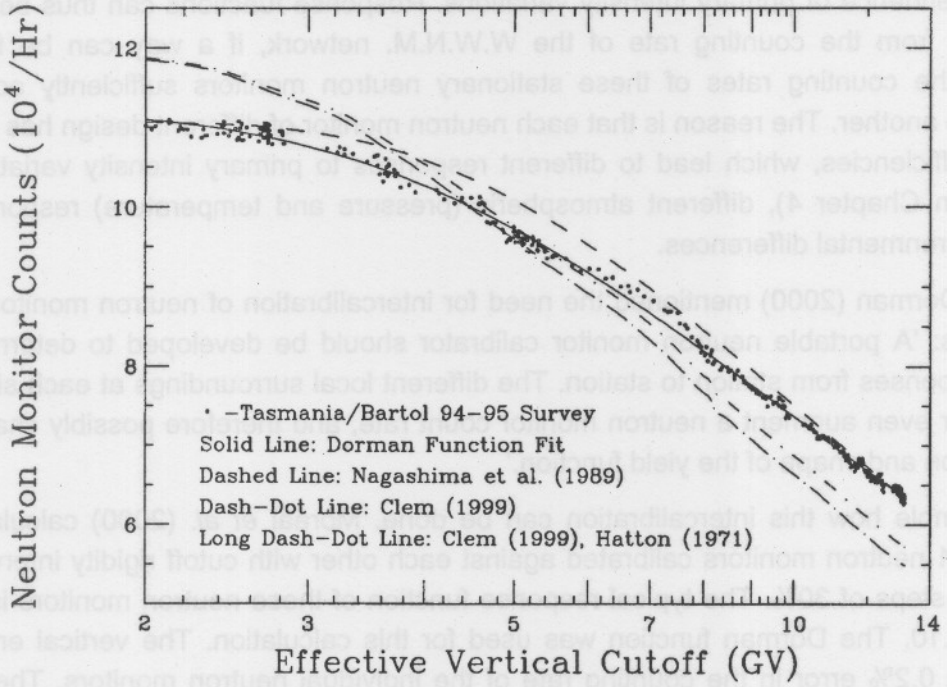

Figure 5.9: The experimental counting rate obtained during the Tasmania-Bartol 1994 – 1995 latitudinal survey, compared to the counting rates derived by using the parameterisation and Monte Carlo methods. Adapted from Clem and Dorman (2000).

The counting rate for latitudinal surveys can be calculated by integrating the response functions over rigidity, using (5.4) and then compare it with the experimental counting rates, as shown in Figure 5.9. In this figure Clem and Dorman (2000) show the counting rate recorded during one of the US / Australian annual latitudinal surveys (1994/5), which is compared with various derived counting rates. The Dorman function was used to fit the observations, displayed by the continuous line. The dashed line shows the parameterisation method used by Nagashima *et al.* (1989) for solar minimum period. The two dash-dot line and the long dash-dot line represent the Monte Carlo method of Clem (1999).

5.5 Intercalibration for spectral studies

The problem with above-mentioned methods is that latitudinal surveys are not performed on a continuous or regular base. On the other hand, the theoretical and Monte Carlo methods need more accurate input. For example, Figures 5.6, 5.8 and 5.9 show that the differences between the theoretical, calculated and experimental lines are too large, which indicate that the atmospheric production of secondary particles is still not sufficiently understood.

Furthermore, differential response functions can also be calculated, in principle, from stationary neutron monitor data by

$$\frac{dN}{dP} \approx \frac{N(P_{c2}) - N(P_{c1})}{P_{c2} - P_{c1}}, \tag{5.11}$$

where P_{c1} and P_{c2} are two reasonably near cutoff rigidities.

The worldwide neutron monitor (W.W.N.M.) network can be used in this way to study the rigidity dependence of primary intensity variations. Response functions can thus be derived in principle from the counting rate of the W.W.N.M. network, if a way can be found to normalise the counting rates of these stationary neutron monitors sufficiently accurately against one another. The reason is that each neutron monitor of different design has different detection efficiencies, which lead to different responses to primary intensity variations (as described in Chapter 4), different atmospheric (pressure and temperature) responses, as well as environmental differences.

Clem and Dorman (2000) mentioned the need for intercalibration of neutron monitors in the same terms: 'A portable neutron monitor calibrator should be developed to determine the relative responses from station to station. The different local surroundings at each site could attenuate or even augment a neutron monitor count rate, and therefore possibly change the normalization and shape of the yield function.'

As an example how this intercalibration can be done, Moraal *et al.* (2000) calculated the rigidity of 11 neutron monitors calibrated against each other with cutoff rigidity intervals that increase in steps of 30%. The typical response function of these neutron monitors is shown in Figure 5.10. The Dorman function was used for this calculation. The vertical error bars represent a 0.2% error in the counting rate of the individual neutron monitors. The size of these error bars shows that an error > 0.2 % would make this calibration not meaningful.

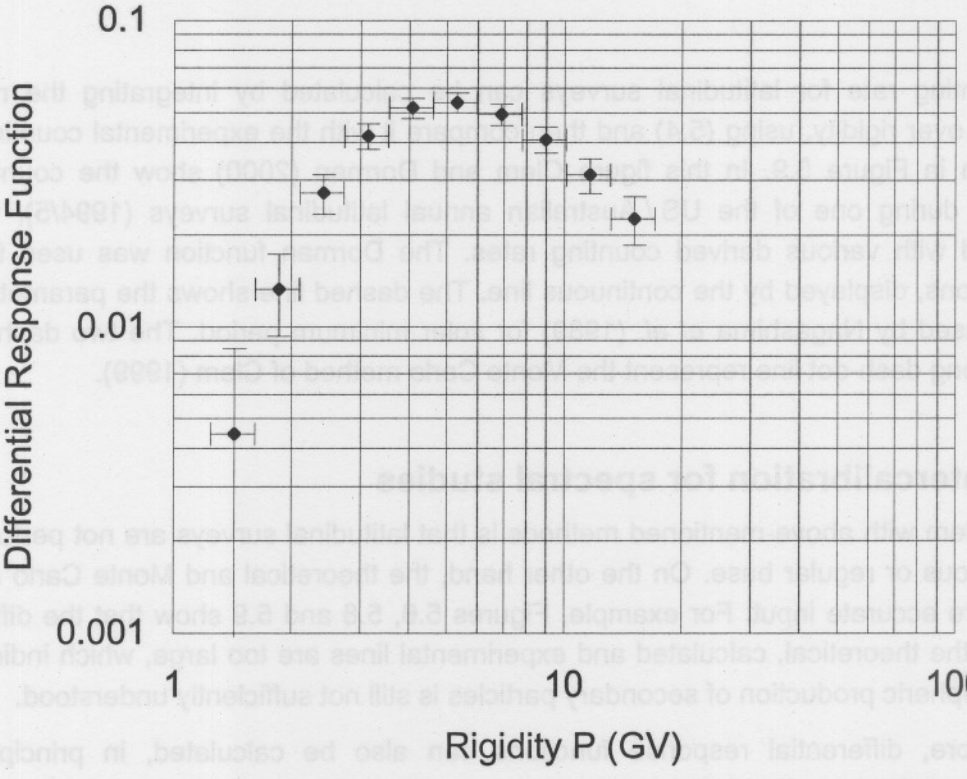

Figure 5.10: Typical differential response function as function of cutoff rigidity for 11 intercalibrated neutron monitors. Adapted from Moraal *et al.* (2000).

This calibration concept is the purpose of this work, as two calibrators were constructed (see next chapter), that can be transported to the worldwide stationary neutron monitors for intercalibration. This calibration became much more viable with the compact and affordable LND25373 ^{3}He counters (described in Chapter 4), with their higher pressure of 4 atmospheres (3040 mm Hg), in comparison with the generally used $^{10}BF_3$ counters with a pressure of 0.25 atmospheres (200 mm Hg). The remainder of this thesis describes this calibrator and the experiments that have so far been conducted with it.

Chapter 6
The Calibration Neutron Monitor

The possibility of a calibration neutron monitor for the purposes discussed in the previous chapter became reality with the availability of the high counting rate ^{3}He counters. Two such calibration neutron monitors were constructed with the neutron monitor programme of the Unit for Space Physics at the Potchefstroom campus of the North-West University in 2001 – 2002. The physical and electronic design and vital statistics of these calibrators are described in this chapter. Most of the pictures and descriptions were obtained from the manual (compiled by De Villiers, 2003) of the calibration neutron monitor, and from http://www.puk.ac.za/opencms/export/PUK/html/fakulteite/natuur/fisika/navorsing/kalibrasie_n_m.html. The author of this thesis was not part of this construction.

6.1 The design of the calibration neutron monitor

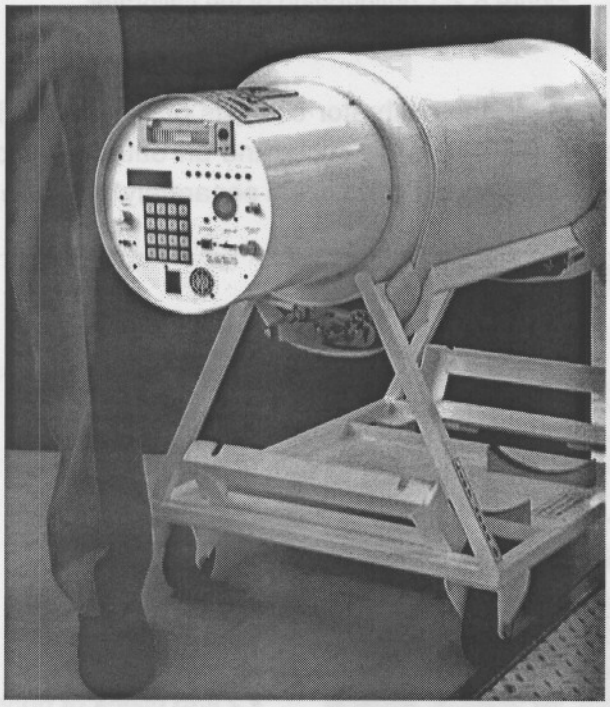

Figure 6.1: The calibrator on its cradle.

Figure 6.1 shows the calibrator on its cradle. It has a total length of 753 mm, i.e. about ⅓ of the length of a standard NM64 neutron monitor. Its total mass excluding the cradle is 201.3 kg. The cradle has a mass of 21.5 kg, and therefore the total mass including the cradle and wheels is 222.8 kg.

Six people can carry the calibrator as a unit. Thus, it can be physically moved and handled and brought to neutron monitors in the worldwide network for intercalibration. It is even possible to put it inside most neutron monitor huts.

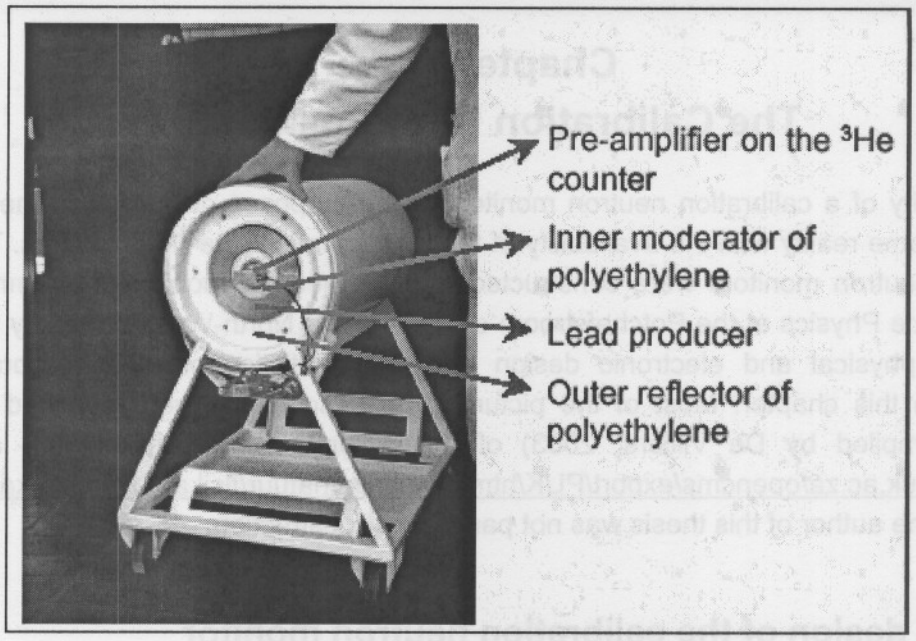

Figure 6.2: Configuration of the calibrator.

Like a standard neutron monitor, the calibrator consists of a counter, filled with ^{3}He gas, an inner moderator of polyethylene, a lead producer and an outer reflector of polyethylene, as shown in Figure 6.2. These components are shown separately in Figure 6.3.

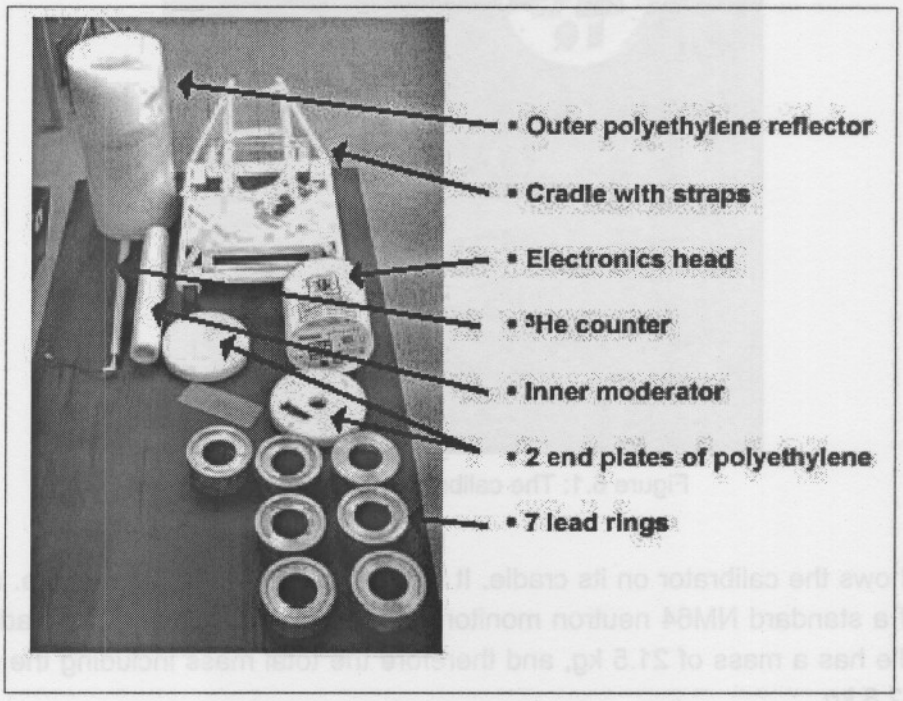

Figure 6.3: Separate components.

6.1.1 The counter

The counters are filled to a pressure of 4 atmospheres (3040 mm Hg) ^{3}He gas in comparison with the 0.25 atmospheres (200 mm Hg) of the standard $^{10}BF_3$ counters.

The cylindrical LND25382 counter has a length of 652 mm, which is about ⅓ of the standard length of the LND25373 in neutron monitor counters. Table 6.1 shows its general specifications.

Table 6.1: From LND, INC (private communication)

Tube type	25382
Cathode material	Stainless Steel
Gas filling	^{3}He
Gas pressure	4 atmospheres
Mass	1.5 kg
Connector type	HN
Pulse height	1 mV
Diameter	50.8 mm
Effective diameter	49.0 mm
Effective volume	1205 cm^3
Operating temperature range	-50 to +100 °C

The electrical specifications for the cylindrical LND25382 counter are shown in Table 6.2.

Table 6.2. From LND, INC (private communication)

Recommended operating voltage	1300 V
Operating voltage range	1200-1450 V
Maximum plateau slope	2 %/100 V
Maximum resolution	10 % FWHM
Capacitance	8 pf
Thermal neutron sensitivity	283.0 cps/nv

6.1.2 The inner moderator

The inner moderator consists of a high-density natural polyethylene $(CH_2)_n$ pipe. Table 6.3 shows the specifications.

Table 6.3: Inner moderator

Material	Polyethylene
Inner diameter	60.5 mm
Outer diameter	99.5 mm
Length	675 mm
Mass	3.0 kg
Density	0.95 Mg/m^3
Melting point	405 K
Maximum service temperature	370 K
Minimum service temperature	210 K

There is a gap of 60.5 – 51.0 = 9.5 mm between the counter tube and the inner moderator. This gap is filled with bubble plastic.

6.1.3 The producer

The lead producer of the calibration monitor consists of 7 lead rings, as shown in Figure 6.3. Table 6.4 gives the specifications of this producer.

Table 6.4: Producer

Material	7 lead rings
Inner diameter	101.0 mm
Outer diameter	193.0 mm
Length	653 mm
Mass	145.3 kg

6.1.4 The reflector

Table 6.5: Reflector

Reflector material	Polyethylene
Inner diameter	194.0 mm
Outer diameter	350.0 mm
Length	753 mm
Mass	42.5 kg

The specifications of the reflector are shown in Table 6.5. The reflector was made of polyethylene as the inner moderator, and specifications of the polyethylene are shown only in Table 6.3.

The calibrator also has two polyethylene end plates, with a thickness of 50 cm and an outer diameter of 299.0 mm. The front plate has a hole for the counter plug and pre-amplifier. The mass of both is 6.0 kg.

6.2 The electronic design

The electronic design and controls are fully described in the manual (compiled by De Villiers, 2003) of the calibration neutron monitor. Only the essential parts needed for operating the monitor are described in this section.

6.2.1 The electronics head

The electronics head, shown in Figure 6.5, has a mass of 3.0 kg. It is removed when transporting the monitor. The front panel is shown in Figure 6.4 and described in Table 6.6.

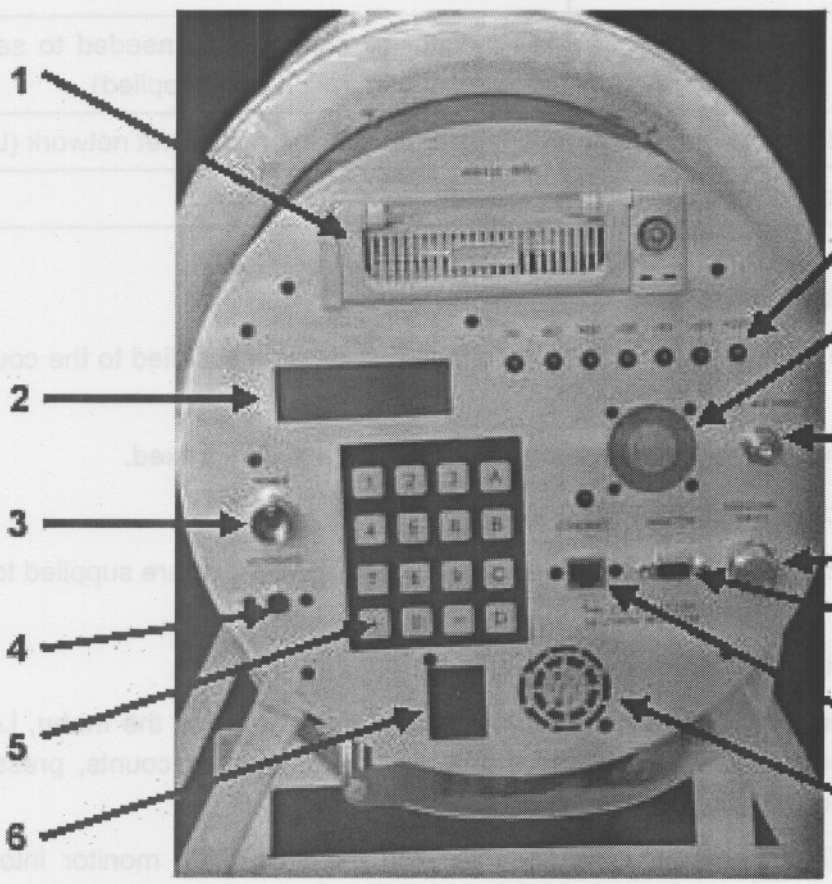

Figure 6.4: The front panel.

Table 6.6: Front panel

Number	Name	Description
1	Mobile hard disk drive	Removable 20 GB hard disk drive
2	LCD display	
3	Power switch	Press button to switch on the monitor
4	Keyboard connector	PC keyboard only needed to set up network configuration (not supplied)
5	Keypad	
6	AC in	Connects the main power supply. Only AC.
7	LED indicators	See text
8	Ventilation / Extraction fan	
9	GPS antenna connection	Connects the external GPS aerial
10	Pressure input	Pressure input for Paroscientific – solid-state barometer
11	Monitor	PC monitor connector, only needed to set up network configuration (not supplied)
12	Ethernet connector	Connects monitor to an ethernet network (LAN)
13	Ventilation / Extraction fan	

The LED indicators display the following:

- HV (High voltage): flashes when the high voltage of 1450 V is supplied to the counter tube.
- SEC (GPS second pulse): starts flashing after the GPS position is fixed.
- HDD (Hard disk drive): indicates IDE activity.
- -5V 5V -12V 12V: these indicators flash when individual voltages are supplied to the electronics when the system is powered on.

The removable hard disk has 20 GB storage capacity.

The keypad can be used to operate the monitor manually and to change the menu, i.e. to shut down, or to change the way of showing the date, total number of counts, pressure, temperature, voltage, and latitudinal and longitudinal coordinates.

The standard RJ45 UTP Ethernet plug is used to plug the calibration monitor into the network. Data can be accessed remotely at its IP address, to be downloaded via FTP or to update the software, or to correct errors from Potchefstroom.

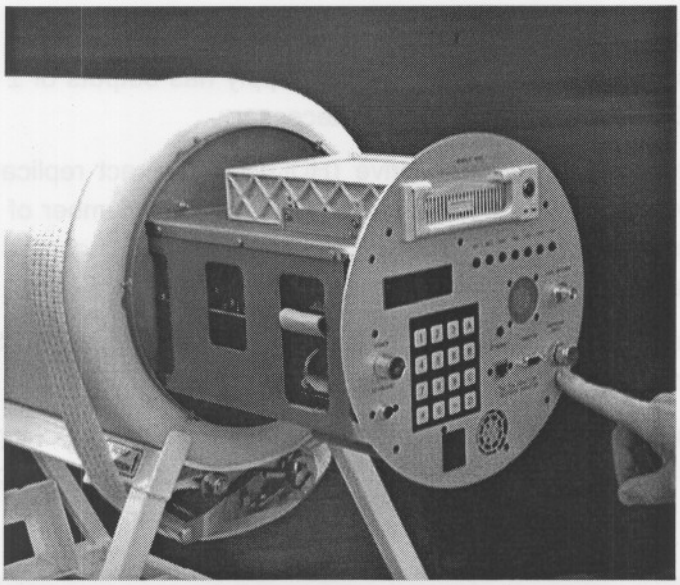

Figure 6.5: The electronics head of the calibration neutron monitor, from the side.

6.2.2 The electronic components

Figure 6.6 shows the electronic components and board layout. The detail description can be found in the operation manual of the calibration neutron monitor.

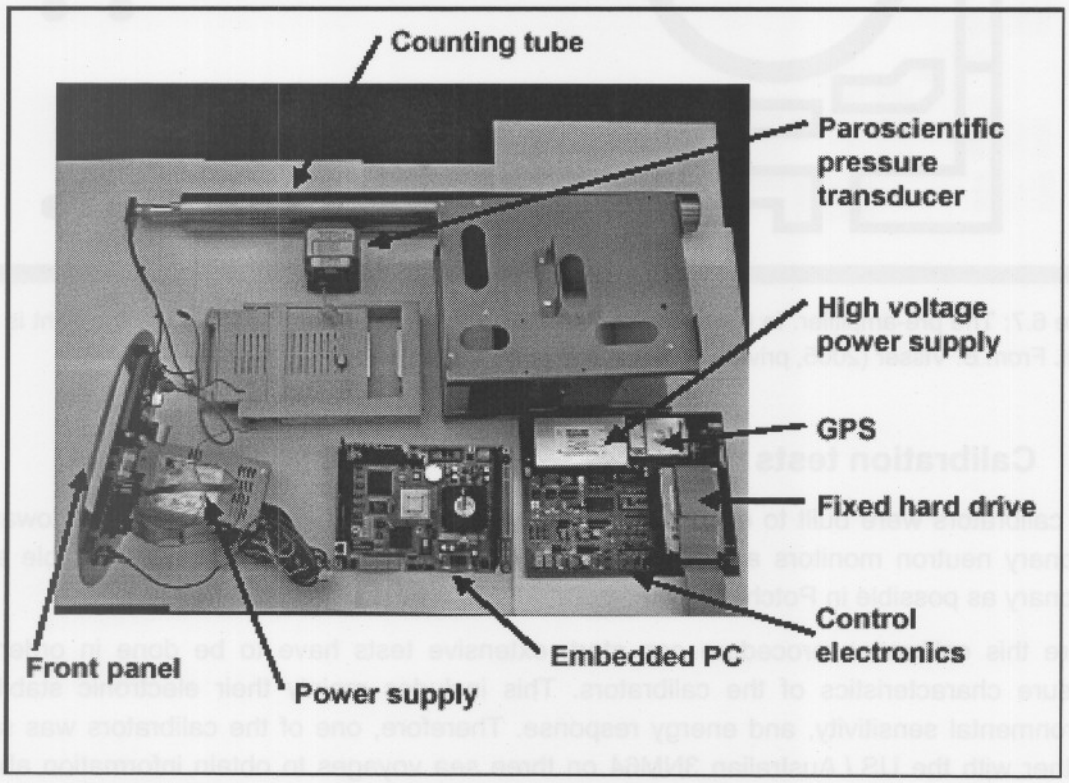

Figure 6.6: The electronic components.

A Paroscientific digiquartz solid-state barometer with accuracy better than 0.1 mm Hg measures the pressure. The 110 – 250 V power supply has outputs of ± 5 V and ± 12 V. A UPS is needed for DC battery operation when necessary.

A fixed 20 GB Notebook master hard drive (HDD) is an exact replication of the 20 GB removable hard drive (HDD). Data are recorded on both. The number of counts, barometric pressure, high voltage, temperature and GPS coordinates are recorded once per second. The fixed drive contains the Operating System.

The control electronic board contains the high voltage power supply, GPS receiver, counter amplifier and discriminator, temperature and HV sensors.

A pre-amplifier is needed at the end of the counting tube for matching and capacitance considerations. The layout, as well as the circuit of this pre-amplifier, is shown in Figure 6.7.

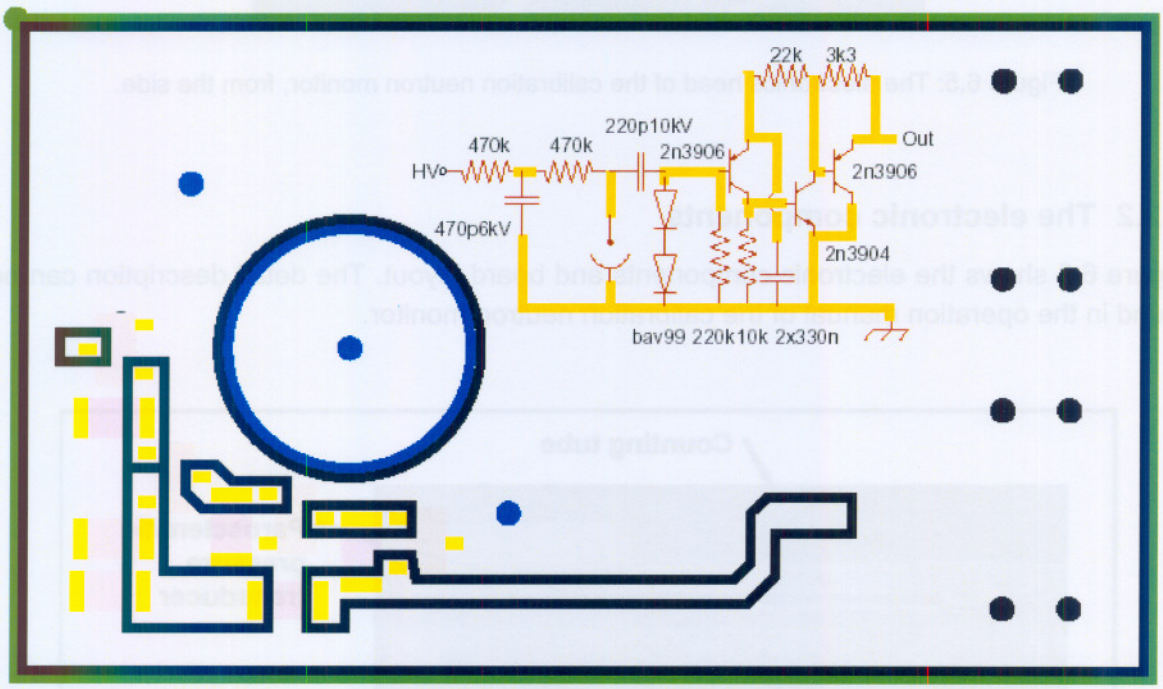

Figure 6.7: The pre-amplifier. In the left bottom is the layout on the board, while at the top right is the circuit. From B. Visser (2005, private communication).

6.3 Calibration tests

Two calibrators were built to ensure redundancy. The plan is to send one of them towards stationary neutron monitors around the world, while keeping the other one as stable and stationary as possible in Potchefstroom.

Before this calibration procedure can start, extensive tests have to be done in order to measure characteristics of the calibrators. This includes mainly their electronic stability, environmental sensitivity, and energy response. Therefore, one of the calibrators was sent together with the US / Australian 3NM64 on three sea voyages to obtain information about the energy response (latitudinal dependence) of this calibrator. This survey is described in

Chapter 7. The other one was used to test its repeatability, as well as the fractional standard deviation, and temperature and environmental sensitivity, in Potchefstroom, as described in Chapters 8 to 10.

An IGY monitor has been in operation in Potchefstroom since May 1971. The calibrator was calibrated against the IGY by simultaneous recordings. Figure 6.8 shows an example of the ratio of the counting rates of the IGY and calibrator as function of time. These counting rates were obtained in Potchefstroom, when both monitors stood in the monitor hut, for days 197-208 in 2004. The average of these ratios is 16.474. No (pressure) corrections were made. The average room temperature was 16.5°C.

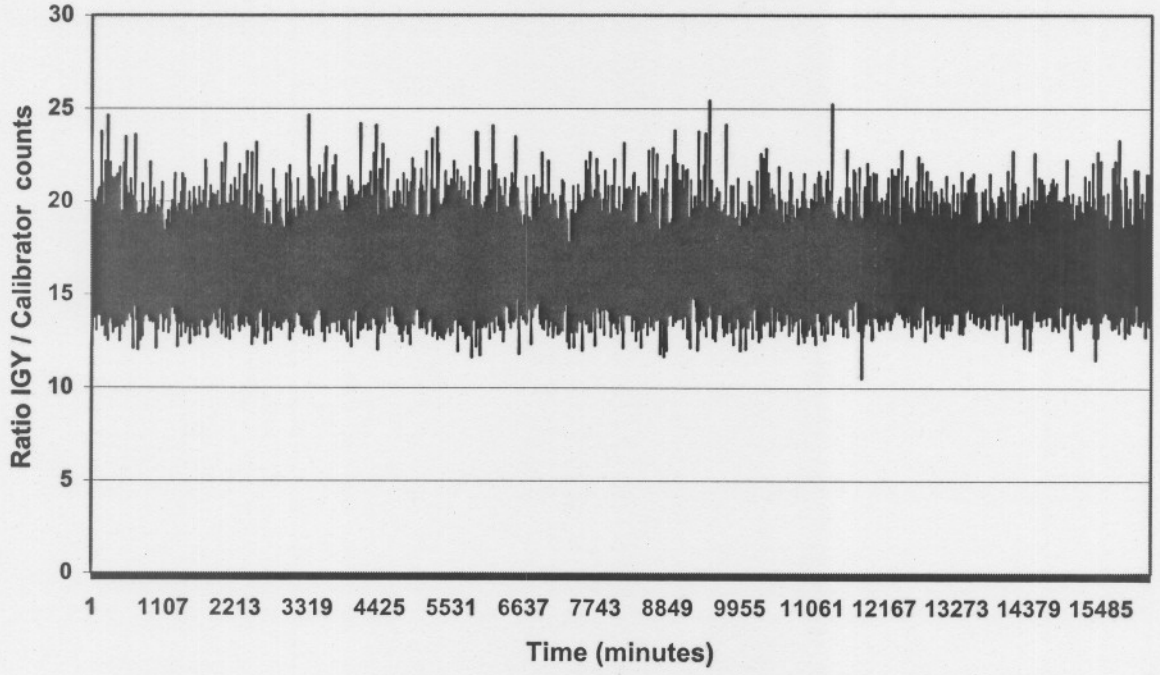

Figure 6.8: The ratio of the counting rates of the IGY and calibrator for days 197-208 in 2004. Both monitors were in the monitor hut, at constant temperature, in Potchefstroom.

Chapter 7
Energy Response of the Calibration Neutron Monitor

7.1 Energy response of neutron monitors

The geomagnetic field influences the trajectories of cosmic rays that penetrate to the top of the atmosphere, as described in Chapter 3. The differential response function, that contains the yield function, $S(P,x)$, is related to the intensity spectrum, $j(P)$, of primary particles at the top of the atmosphere, as described in Chapter 5, with (5.2):

$$-\frac{dN}{dP} = S(P,x)\,j(P,t)\,. \tag{5.2}$$

The counting rate of a neutron monitor during a latitudinal survey, going through a range of geomagnetic cutoff rigidities, gives the integral response function from which the differential response function may be derived. Neutron monitors of different design have different responses to primary intensity variations, as well as different atmospheric (pressure and temperature) responses. Thus, to achieve an accuracy of ± 0.2%, as described in Chapter 5, any difference in energy response between the calibrator and the standard NM64 type stationary neutron monitors must be known to within this accuracy.

Intensity changes increase with decreasing rigidity. The neutron monitor sensitivities for changes in the primary spectrum can be calculated by the following expression, from (5.2) and (5.4):

$$\delta N(P \geq P_c) = \int_{P_c}^{\infty} S(P,x)\,\delta j(P)\,dP\,.$$

J.A. Simpson wanted to investigate the energy spectrum and origin of cosmic rays after World War II. In 1946 he decided to investigate the dependence of the nucleonic cascade on the incident nucleon energy (Simpson, 2000). He was the first person to use the geomagnetic field cutoff effect as a function of latitude for analysis of the incident primary cosmic rays at the top of the atmosphere by measuring the nucleonic cascade. In this way Simpson (1951) observed that a large latitudinal effect exists for the production of neutrons produced by primary charged particles. He concluded that the response of a neutron monitor is more sensitive to lower energies in the primary spectrum.

According to Shea and Smart (2000), neutron monitors at sea level in the polar regions, where the geomagnetic shielding is least effective, can respond to incident protons above ~450 MeV, i.e. at $P_c < 1.0$ GV, which is the atmospheric cutoff. The incident protons must have considerably higher energies in the equatorial regions, above ~17 GeV, i.e. $P_c \approx 17$ GV, in order to be detected.

As mentioned in Chapter 5, Stoker *et al.* (1980) operated three detectors on a sea-borne latitudinal survey from South Africa to Japan and the USA in 1976. They used a 1NM64 super neutron monitor, which they called NM1, and a neutron monitor NM2 with cylindrical

lead rings. The total mass of lead of the NM2 was made equal to the total mass of lead of the NM1 by increasing the diameter of the outer ring. The results are displayed in Figure 7.1.

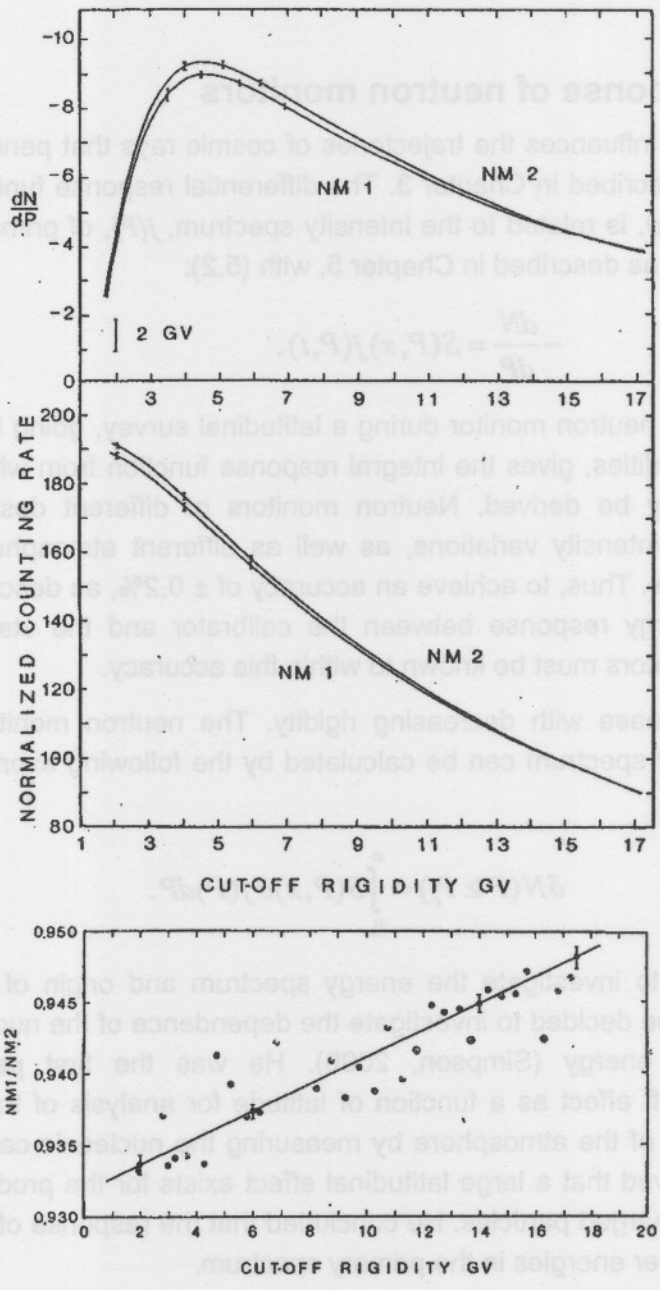

Figure 7.1: The top panel shows the differential response functions for the NM1 and NM2 as function of cutoff rigidity, while the middle panel indicates the corresponding integral response functions for the NM1 and NM2, normalised to a counting rate of 100 at 15 GV. The bottom panel shows the ratio of the hourly counting rate of the NM1 and NM2, as function of cutoff rigidity. Adapted from Potgieter *et al.* (1980).

Figure 7.1 (top two panels) displays the differential response functions, as well as the difference between the integral functions, i.e. the counting rates, for the NM1 and NM2 as function of rigidity, normalised to a counting rate of 100 at 15 GV. Figure 7.1 (bottom panel)

gives the ratio of the two monitors, binned into interval averages of 0.5 GV, as function of cutoff rigidity. The solid curve represents a best-fit regression line. The NM2 counting rate increased with 0.1 %/GV relative to the NM1. If two neutron monitors with such a nearly similar design have such a large difference in energy dependence, one must foresee that the energy dependence of the calibrator may also differ significantly from that of the NM64 (or IGY). Therefore, this chapter describes an experiment to measure and simulate these energy dependences.

Another example of obtaining differential response functions with a latitude survey, is the annual latitude surveys conducted by a US / Australian collaboration from the USA to Antarctica, as also mentioned in Chapter 5, and further discussed in Section 7.4. Bieber *et al.* (2003) reported on how the 8 annual surveys from 1994 to 2002 were divided into 26 data segments and the preliminary analysis of the data. Figure 7.2 shows the hourly data points plotted against the effective cutoff rigidity > 2 GV, for segment 9. The Dorman function (5.5) was fitted to the data points. This function was differentiated to give the differential response function (5.6), also shown in Figure 7.2.

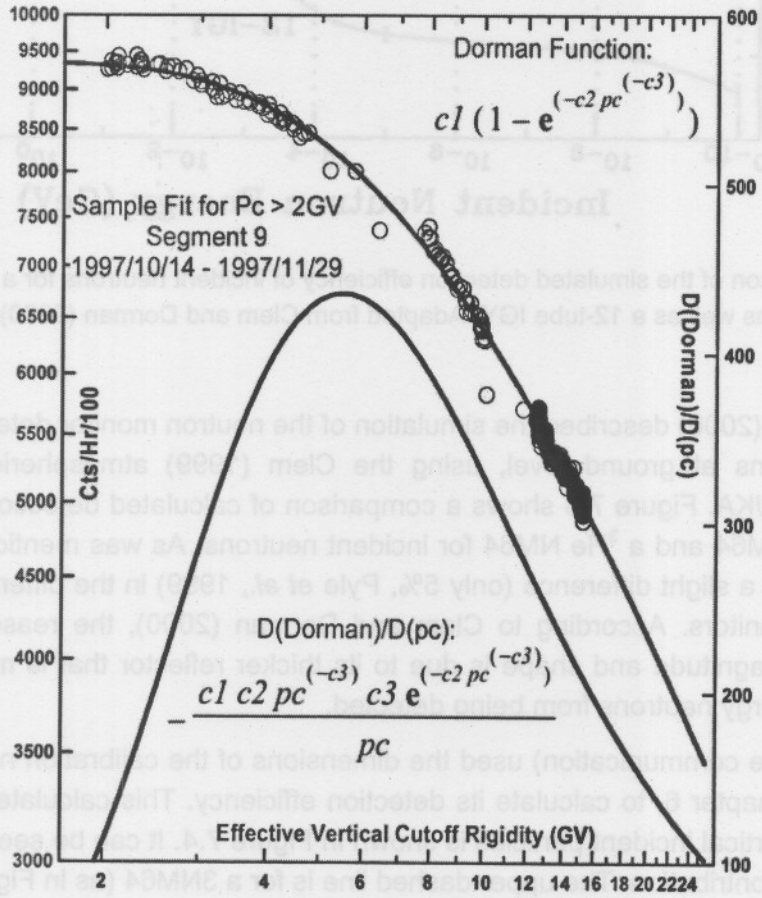

Figure 7.2: The counting rate as function of cutoff rigidity, fitted with the Dorman function, as well as the differential response function obtained by differentiating this Dorman function. Adapted from Bieber *et al.* (2003).

7.2 Simulation of detection efficiencies of neutron monitors

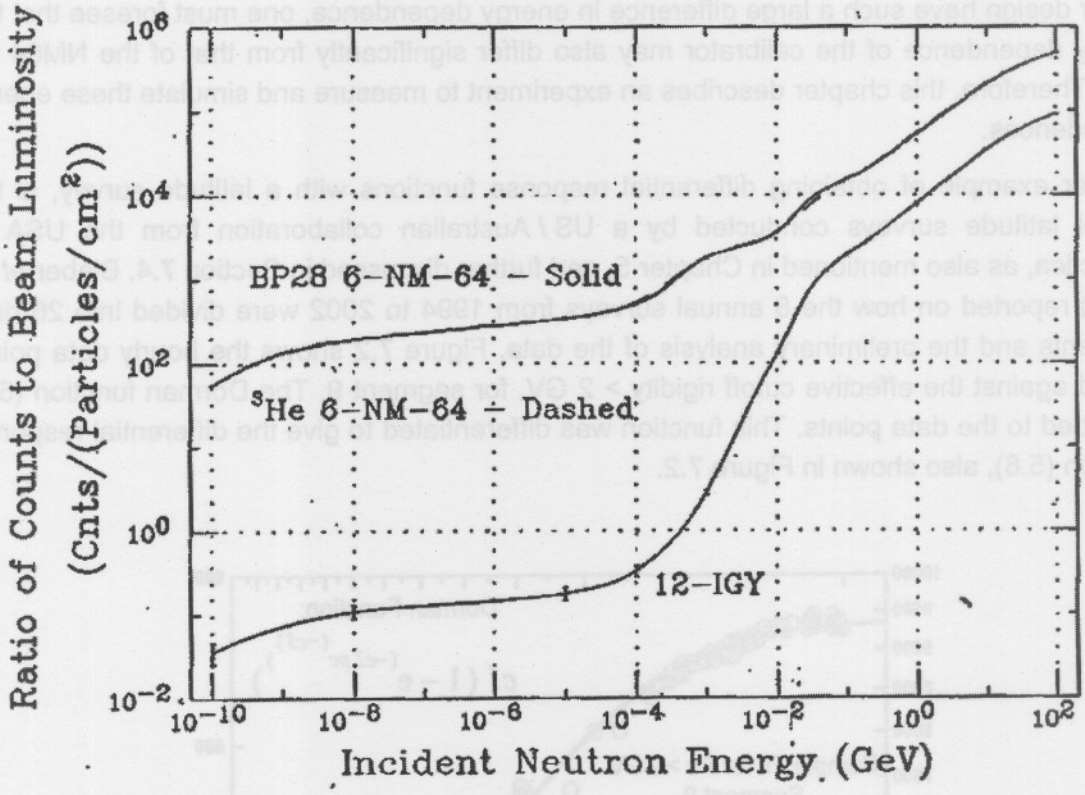

Figure 7.3: Comparison of the simulated detection efficiency of incident neutrons for a 6NM64 with ^{3}He and $^{10}BF_3$ counters, as well as a 12-tube IGY. Adapted from Clem and Dorman (2000).

Clem and Dorman (2000) described the simulation of the neutron monitor detection efficiency of incident neutrons at ground level, using the Clem (1999) atmospheric Monte Carlo transport code FLUKA. Figure 7.3 shows a comparison of calculated detection responses of an IGY, a $^{10}BF_3$ NM64 and a ^{3}He NM64 for incident neutrons. As was mentioned in Section 4.3.2, there is only a slight difference (only 5%, Pyle *et al.*, 1999) in the different counters of the two NM64 monitors. According to Clem and Dorman (2000), the reason for the IGY differing in both magnitude and shape is due to its thicker reflector that is more efficient in preventing low energy neutrons from being detected.

Clem (2005, private communication) used the dimensions of the calibration neutron monitor, as described in Chapter 6, to calculate its detection efficiency. This calculated efficiency for various kinds of vertical incident particles is shown in Figure 7.4. It can be seen that neutrons make the largest contribution. The upper dashed line is for a 3NM64 (as in Figure 7.3). When comparing the two lines for neutron detection, the efficiency of the calibrator is between 2% and 5% of the 3NM64, depending on primary energy. From this simulation one expects that the ratio of the calibrator to NM64 counting rate will decrease as function of cutoff rigidity.

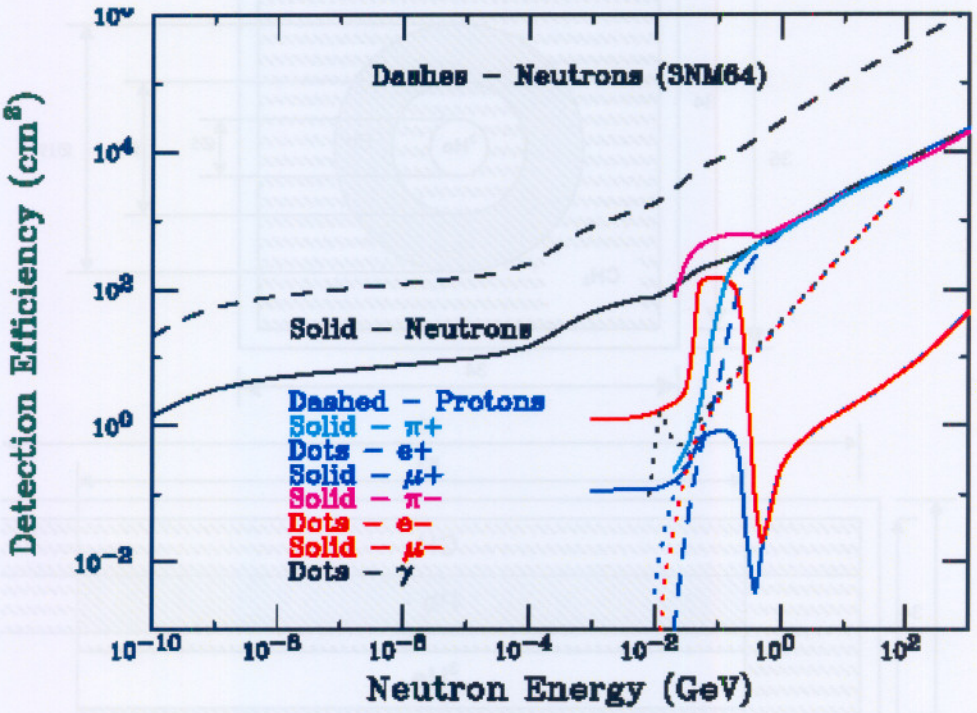

Figure 7.4: The simulated detection efficiency of the calibration neutron monitor as function of neutron energy for different kinds of vertical incident particles. From J.M. Clem (2005, private communication).

7.3 Simulation of energy response of neutron monitors

Clem (2005, private communication) actually calculated the calibrator/NM64 counting ratio as function of cutoff rigidity twice. The first one was for a conceptual design of the calibrator, done in 2000. The second calculation was for the actual calibrator design, done in 2005. Since the two designs and the calculated ratios differ significantly, both are described here.

The measurements used in the conceptual design of the calibrator for this simulation, are given in Figure 7.5, obtained from Moraal *et al.* (2000). The counter is a LND25382 tube, filled with ^{3}He at a pressure of 4 atmospheres. The length is 63 cm, about ⅓ of the length of a counter (LND25373 tube) used in a standard neutron monitor. The diameter is 4.8 cm. A moderator of paraffin wax, 2 cm thick, surrounds the counter. A lead producer, 5 cm thick and with a mass of 170 kg, surrounds the moderator. This lead ring is surrounded by an outer reflector of paraffin wax. The paraffin wax has a mass of 24 kg. The total outer dimensions are 79 x 35 x 35 cm, with a mass of about 220 kg. This monitor is inside an aluminium box, 5 mm thick.

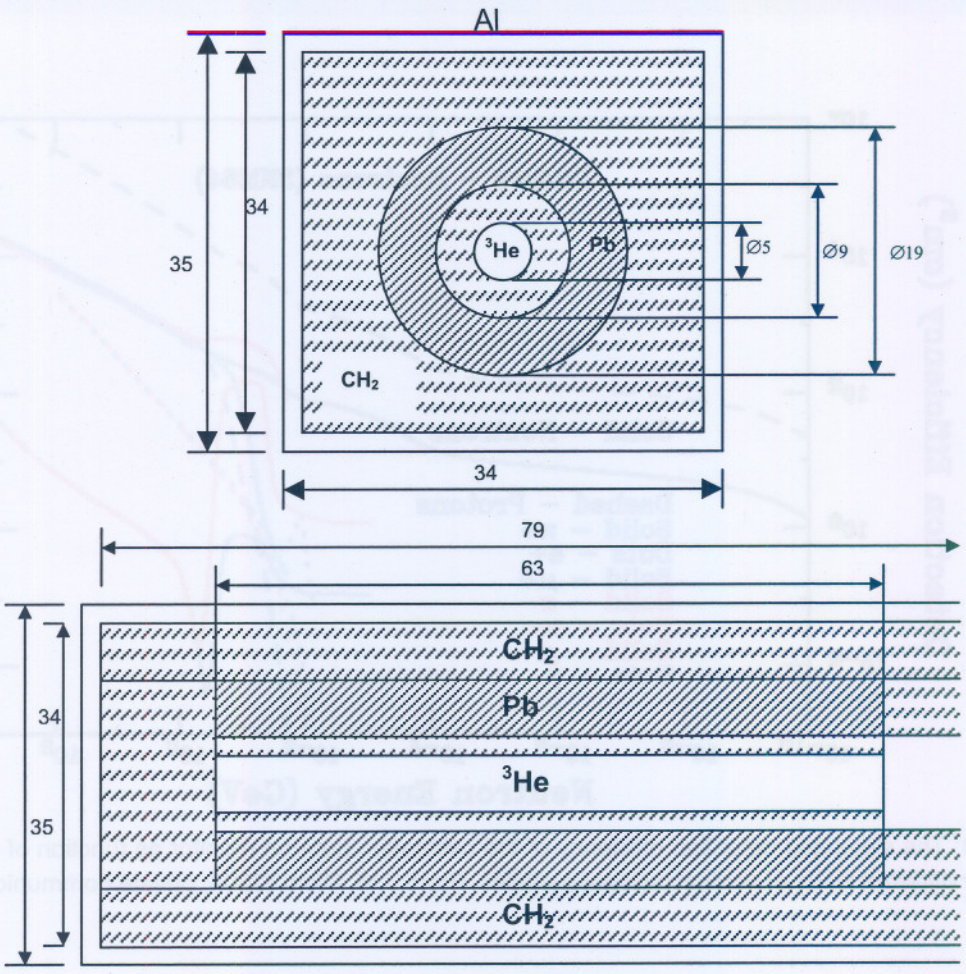

Figure 7.5: A schematic diagram of the original conceptual design of the calibration neutron monitor. The dimensions are in cm. It consists of a ^{3}He counter surrounded by an inner moderator 2 cm thick, a lead producer 5 cm thick, and an outer reflector, inside an aluminium box 5 mm thick. Adapted from Moraal *et al.* (2000).

The simulation performed on this preliminary design of the calibration neutron monitor is shown in Figure 7.6. Here the ratio of the counting rate of the calibration neutron monitor and the 6NM64 is given as function of cutoff rigidity P_c. Only the response to neutrons and protons was calculated. This was regarded as sufficient for determining the general characteristics of the monitor, because neutrons and protons make the largest contributions to the counting rate of the IGY and NM64 monitors, as shown in Figure 7.4.

The counting ratio in Figure 7.6 has an average slope of about -0.18 %/GV, or 2.7% from 1 to 15 GV. This indicates that the energy response of the calibrator may differ by as much as 0.18 %/GV from that of an NM64. Moraal *et al.* (2000) pointed out that this is too large for calibrations when an accuracy of < 0.2% is required, and it must therefore be corrected for.

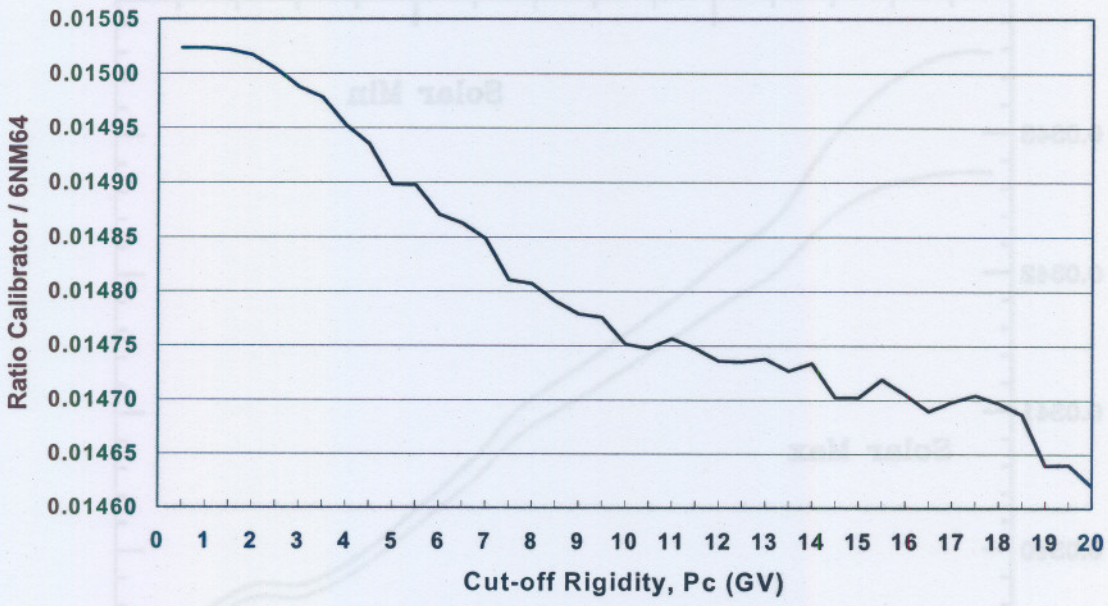

Figure 7.6: Simulation by Clem and co-workers. Adapted from Moraal *et al.* (2000).

During 2005, Clem (private communication) repeated simulations of the energy response of the calibrator, but this time for the actual calibrator, as described in Chapter 6. The detection efficiencies of Figure 7.4 are from this simulation. Figure 7.7 shows this calculated ratio of the counting rates of the calibration neutron monitor and the 3NM64 as function of cutoff rigidity P_c. This time the response for all the incident particles was taken into account, except the electromagnetic component (electrons and gammas). The simulation was done for a differential response function at both solar minimum and maximum conditions. As expected, the solar minimum response is noticeably steeper, due to the fact that more low-energy particles are included.

The counting ratio in Figure 7.7 has an average slope of about -0.08 %/GV. This is about half of the value obtained previously for the conceptual design. The difference between the two may lie in the difference in the geometry of the design and the actual calibrator, but may also be due to neglect of the contribution of minor species in Figure 7.6. One notices from Figure 7.4 for instance, that these minor species may make a significant contribution at higher energies, diminishing the latitudinal dependence of the counting ratio.

Clem (2005, private communication) suspects the difference is the result of excluding angular effects in the most recent calculations, because only vertically incident particles were considered. He expects that the calibrator has a stronger cosine projection dependence than the NM64. Furthermore, the peak energy of arriving particles (particularly muons) should be angle dependent. Clem is currently calculating the NM64 angular dependent response on a ship-like background and on the calibrator in identical environment.

To determine the difference of the energy responses between the two neutron monitors experimentally, one of the two calibrators was taken on a series of three latitudinal surveys together with an NM64.

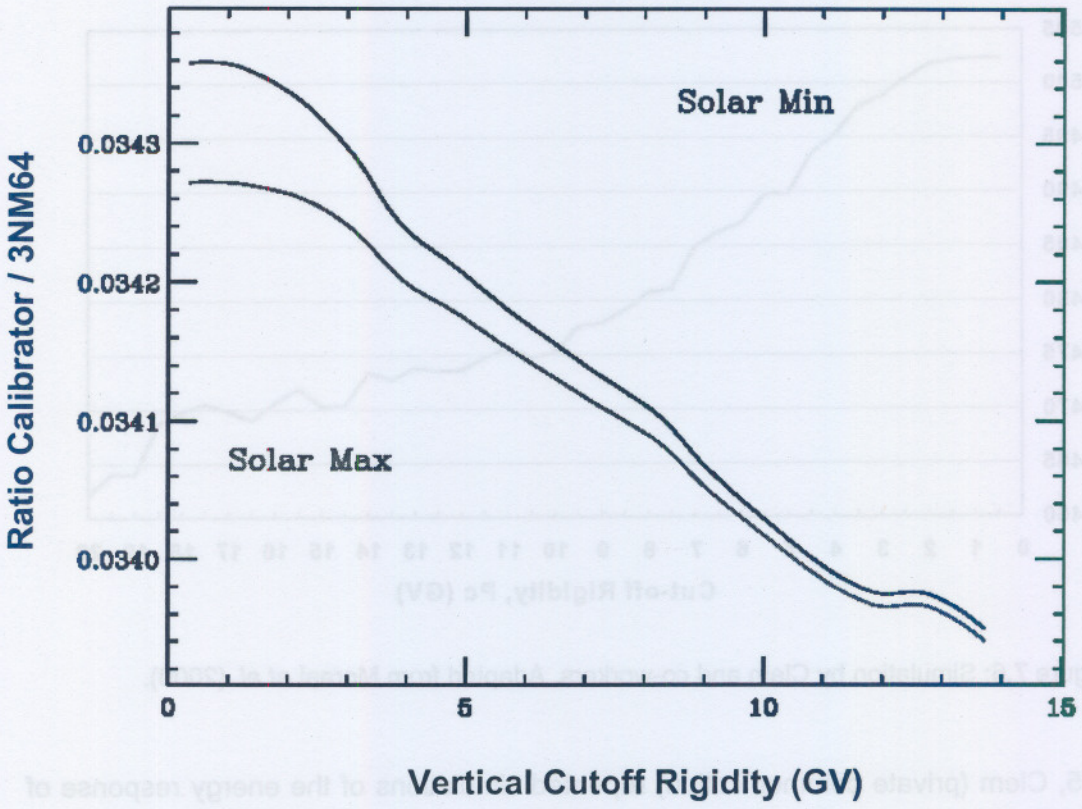

Figure 7.7: The simulated ratio of the counts of the calibrator and 3NM64 for a steel surface to simulate the ship, as function of cutoff rigidity. From Clem (2005, private communication).

7.4 Latitudinal surveys of the calibrator together with the 3NM64

The Bartol Research Institute, in collaboration with the Australian Antarctic Division and the University of Tasmania, have conducted a neutron monitor latitudinal survey annually since 1994, from Seattle, USA, to McMurdo, Antarctica, and back, over a 5 – 6 months period. The routes for 1994 to 2002 can be seen in Figure 7.8. They use a standard 3NM64 neutron monitor aboard one of two US Coast Guard icebreakers, the vessels *Polar Sea* and *Polar Star*. These surveys cover cutoff rigidities from ≈ 0.1 GV at McMurdo to ≈15 GV in the mid-Pacific. Details of these annual surveys were described by Bieber *et al.* (1997, 2001a, 2003).

One of the two Potchefstroom calibrators was sent with this 3NM64 on three of these voyages. The main reason was to test our calibration neutron monitor against the standard monitor, as well as to measure the latitudinal response of the calibrator against that of the standard 3NM64, and compare it with the simulated ratios of the previous section.

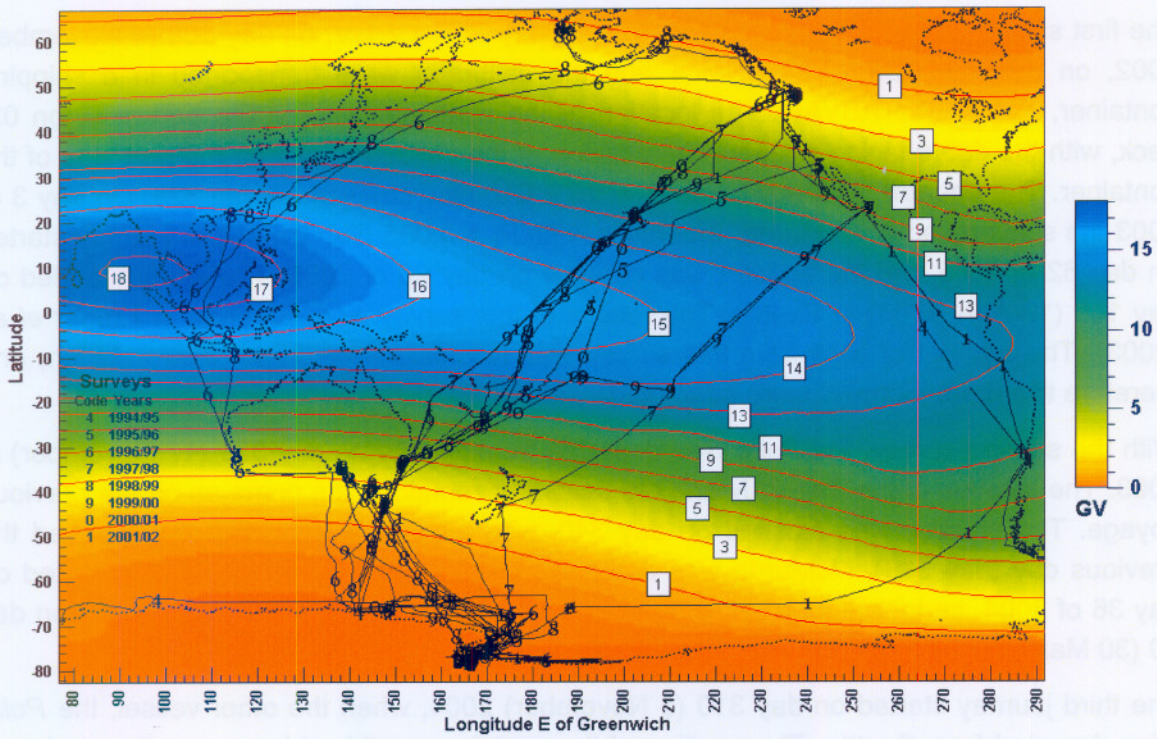

Figure 7.8: Annual latitudinal surveys from 1994 to 2002 by the Bartol Research Institute, USA, in collaboration with the Australian Antarctic Division and the University of Tasmania. Cutoff rigidities are shown as contours. From K.R. Pyle (private communication).

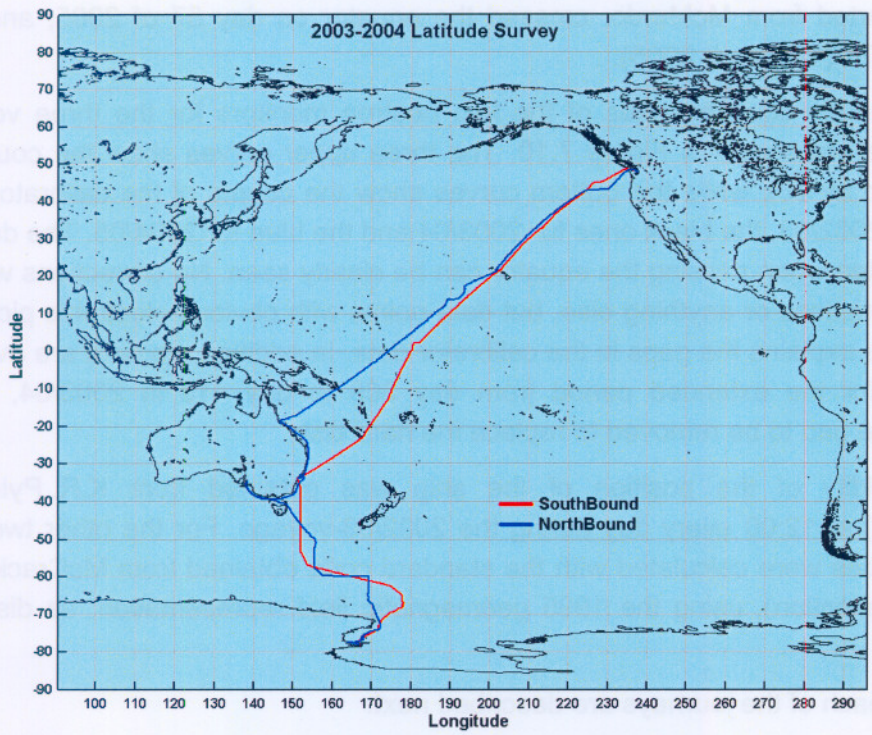

Figure 7.9: The route of the latitudinal survey during 2003/04. From K.R. Pyle (private communication).

The first survey started in Seattle, with cutoff rigidity $P_c \approx 1.7$ GV, on day 308 (4 November) 2002, on the *Polar Sea*. The 3NM64 and the calibrator were transported in a shipping container, called the TASVAN. The location of the container was on the port side, on 02-deck, with the doors facing a stern. The position of the calibrator was on the port side of the container. The equator, with maximum $P_c \approx 15.2$ GV, was crossed on day 328. On day 3 of 2003 the ship arrived at McMurdo, Antarctica, with $P_c = 0.095$ GV. The return journey started on day 62 of 2003 and the equator was crossed on day 96 of 2003. The journey ended on day 109 (19 April 2003) in Seattle. The results of this survey were reported in Krüger *et al.* (2003). The amount of data from this survey was insufficient for proper interpretation, and therefore two more journeys were attempted.

With the second survey, the *Polar Sea* departed from Seattle on day 321 (17 November) in 2003. The location of the TASVAN and the calibrator remained the same as on the previous voyage. The equator was crossed on day 340, with maximum $P_c \approx 15.5$ GV reached the previous day (day 339). McMurdo was reached on day 365. The return journey started on day 36 of 2004, and the equator was crossed on day 77 of 2004. It ended in Seattle on day 90 (30 March 2004). This route is shown in Figure 7.9.

The third journey started on day 310 (5 November) 2004, when the other vessel, the *Polar Star*, departed from Seattle. The position of the container on this ship was on the starboard side, 02-deck, with the doors facing towards the bow. The calibrator and 3NM64 were left in exactly the same location inside the container as in the previous voyages on the *Polar Sea*, viz. behind the left door (L. Schulman, private communication). The ship crossed the equator on day 327, with maximum $P_c \approx 15.2$ GV, and reached McMurdo on day 365. On day 40 of 2005 she departed from McMurdo, crossed the equator on day 57 of 2005, and reached Seattle on day 76 (17 March 2005).

The average hourly counting rates of the two neutron monitors for the three voyages as function of time are shown in Figure 7.10. The three upper curves show the counts of the 3NM64 (divided by 10), while the bottom curves show the counts of the calibrator. The red curves are for 2002/03, the black ones for 2003/04 and the blue for 2004/05. The decrease in the counting rates when passing the equator can be clearly seen. No corrections were made for pressure variations or anything else, but data points with obvious electronic pick-up were eliminated. This explains the gaps in the calibrator data. In addition, no data are available for the calibrator for the extended period from day 366 to day 413 in 2003/04, when the electronics head had to be removed to replace the hard disk.

The cutoff rigidity of the position of the ship was obtained from K.R. Pyle (private communication) at 12:00 every day during the 2002/03-voyage. For the other two voyages the cutoff rigidities were calculated with the standard code obtained from McCracken (2005, private communication), using the 1995 geomagnetic field representation, as discussed in Chapter 3.

The results of each of the journeys are described next.

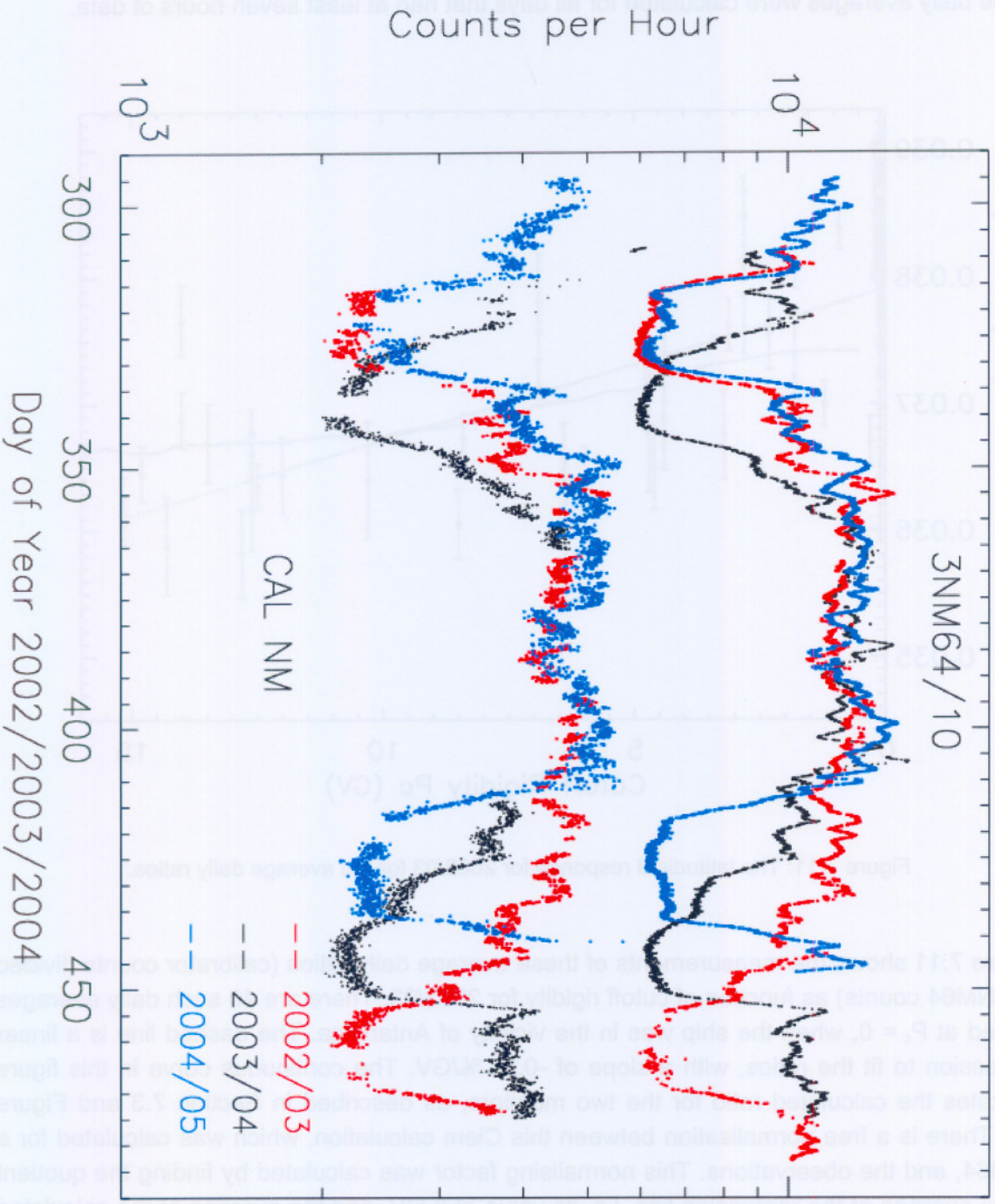

Figure 7.10: The average hourly counting rates of the calibrator and 3NM64 for three latitudinal surveys. The horizontal axis starts on day 290 of each year, and continues past day 365 into the first part of the next year.

The counts of the calibrator and 3NM64 were averaged in one-day intervals, and the ratios of these daily averages were calculated for all days that had at least seven hours of data.

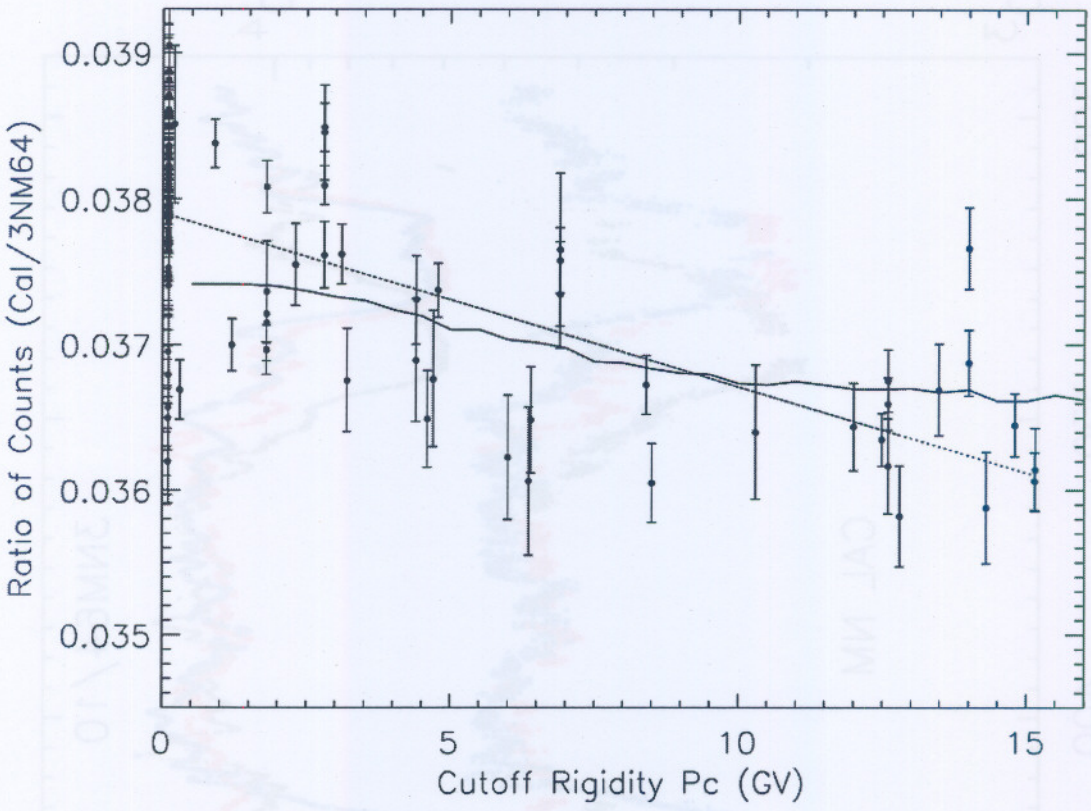

Figure 7.11: The latitudinal response for 2002/03 for the average daily ratios.

Figure 7.11 shows the measurements of these average daily ratios (calibrator counts divided by 3NM64 counts) as function of cutoff rigidity for 2002/03. There are 49 such daily averages plotted at P_c = 0, when the ship was in the vicinity of Antarctica. The dashed line is a linear regression to fit the ratios, with a slope of -0.31 %/GV. The continuous curve in this figure indicates the calculated ratio for the two monitors, as described in Section 7.3 and Figure 7.6. There is a free normalisation between this Clem calculation, which was calculated for a 6NM64, and the observations. This normalising factor was calculated by finding the quotient of the average of the regression line, i.e. its value at 8 GV, and the average of the calculated ratio for 0.5 – 16 GV in Figure 7.6, and was determined as 2.491.

This figure also shows that the scatter in the observed ratios is quite large, but it can clearly be seen that the observed ratios are smaller at higher cutoff rigidities than at lower rigidities. The error bars were calculated by using the hourly counts of both monitors for the number of completed hours in a day, as given in Section 8.2:

$$\text{error} = \text{standard deviation on hourly counting rate} / \sqrt{h}\,, \qquad (7.1)$$

where h = number of completed hours per day.

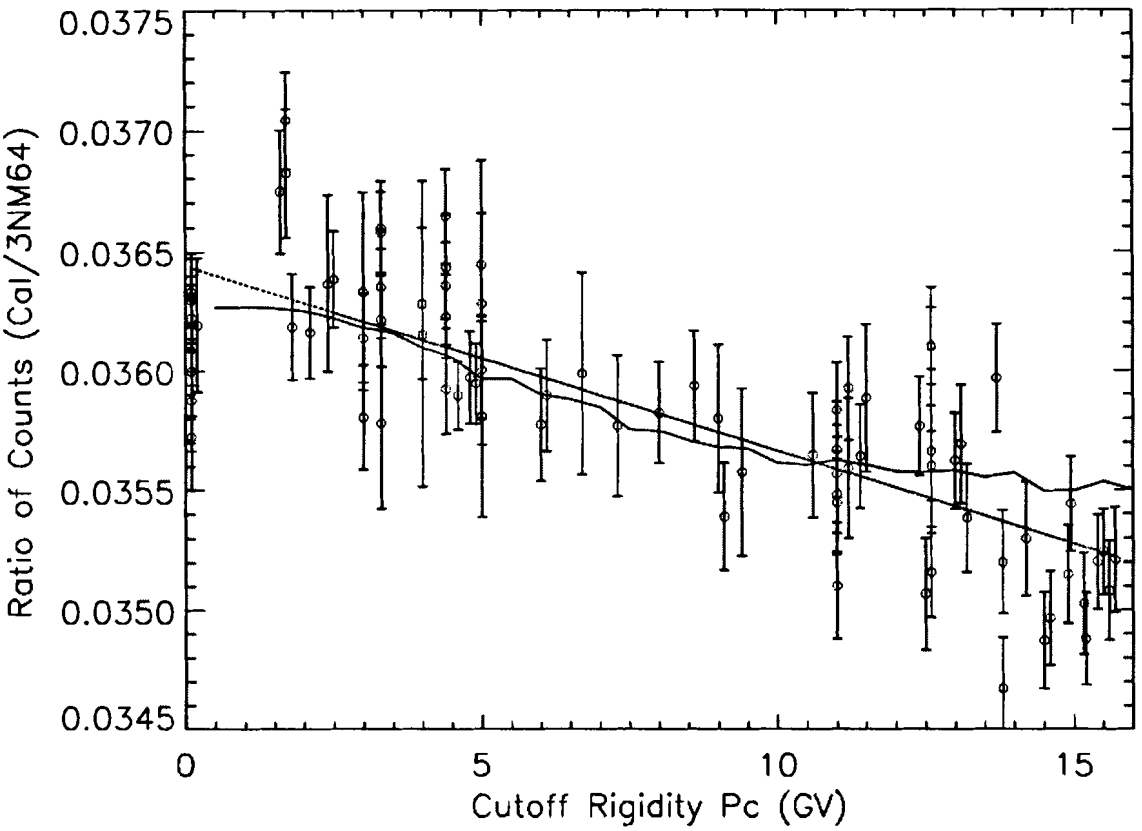

Figure 7.12: The latitudinal response for 2003/04 for the average daily ratios.

Figure 7.12 is the same as Figure 7.11, but for the second voyage in 2003/04. At cutoff rigidities > 1GV, there are now many more data points than during the previous year. The reason is that there are many gaps in the 2002/03-calibrator data because of intermittent failures of the electronics. At cutoff rigidities < 1GV, however, the figure shows only a few data points, because there were no calibrator counts at McMurdo and between McMurdo and Adelaide, Australia, as shown in Figure 7.10. The scatter is considerably less than the previous year's (Figure 7.11).

The continuous curve in Figure 7.12 shows the calculated ratio of Figure 7.6 for the two monitors by Clem. The normalisation factor for these values was calculated in the same way as for the previous year (2002/03) and has the value of 2.414. The slope of the linear regression is –0.21 %/GV, which is in much better agreement with that of the Clem calculation of –0.18 %/GV than the previous year's, shown in Figure 7.11.

An alternative presentation of the results of the two voyages in 2002/03 and 2003/04 can be obtained by binning the average daily ratios into rigidity intervals of 1 GV each, as shown in Figure 7.13 for 2002/03 and Figure 7.14 for 2003/04. This means that all days during which the monitors were within such a rigidity range, were averaged into one point. Separate crossings of a rigidity interval were, however, kept separate. In this way one can find up to four such points per interval: two for crossing it on both sides of the equator on the outbound leg, and two for the return. Here again, there are more data points collected for 2003/04

(Figure 7.14) than during the previous year (Figure 7.13) and the scatter is less. The error bars were calculated from the errors of the calibrator and 3NM64, calculated in (7.1), by using (8.7). The small error on the data point at 0 GV is due to the long period that the ship spent at McMurdo.

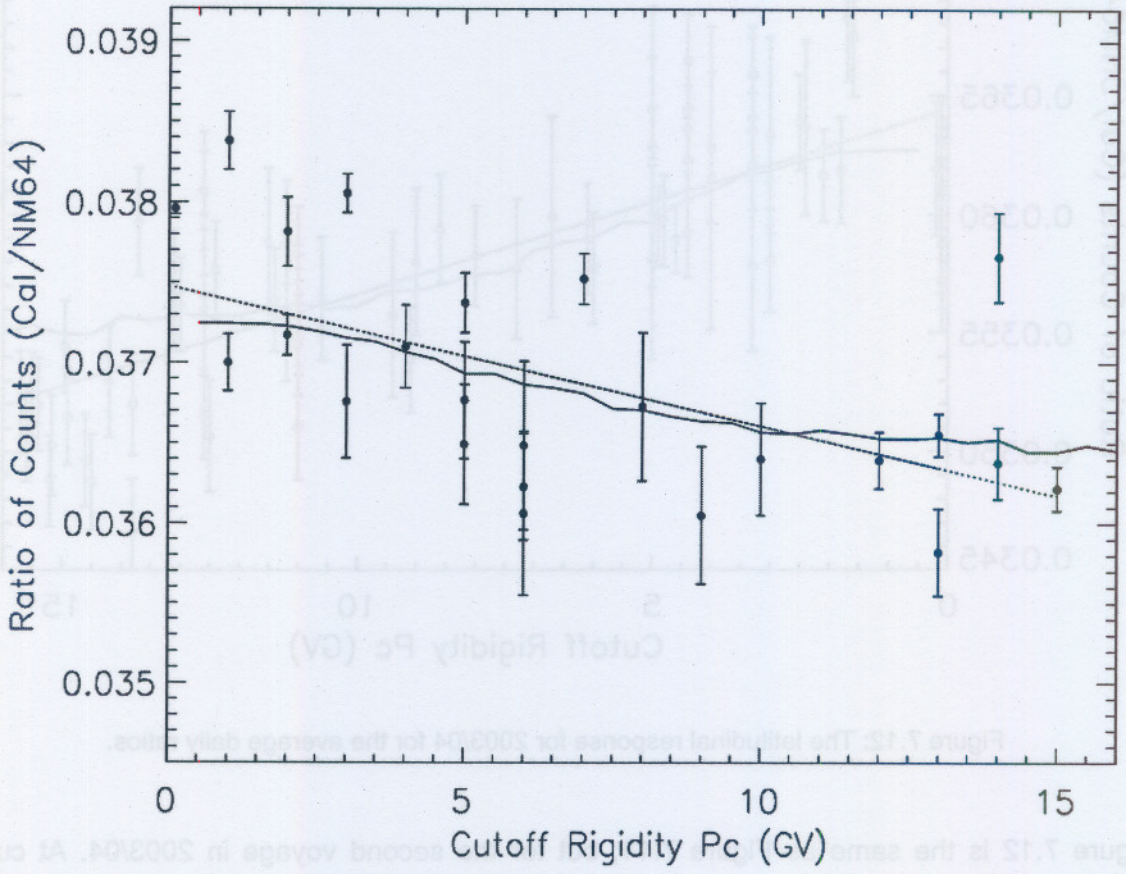

Figure 7.13: The counting ratios binned into rigidity intervals for 2002/03.

As in Figures 7.11 and 7.12, the continuous curve in Figures 7.13 and 7.14 indicates the ratio that was simulated by Clem, as shown in Figure 7.6, and normalised by finding the quotient of the average of the regression line and the average of the simulated ratio, and was determined as 2.479 and 2.416, respectively.

Figure 7.15 shows the average counting ratios of the counting rates for 2004/05 in the same format as Figures 7.13 and 7.14 for 2002/03 and 2003/04. The short error bars in general indicate that sufficient measured data were obtained. There is, however, a 24% random variation in the data, in comparison with a 5.9% variation of the ratios in Figure 7.14 for 2003/04. This large random fluctuation in the calibrator counts renders this third voyage useless. This was traced back to a problem with the pre-amplifier, which was replaced at the end of the voyage.

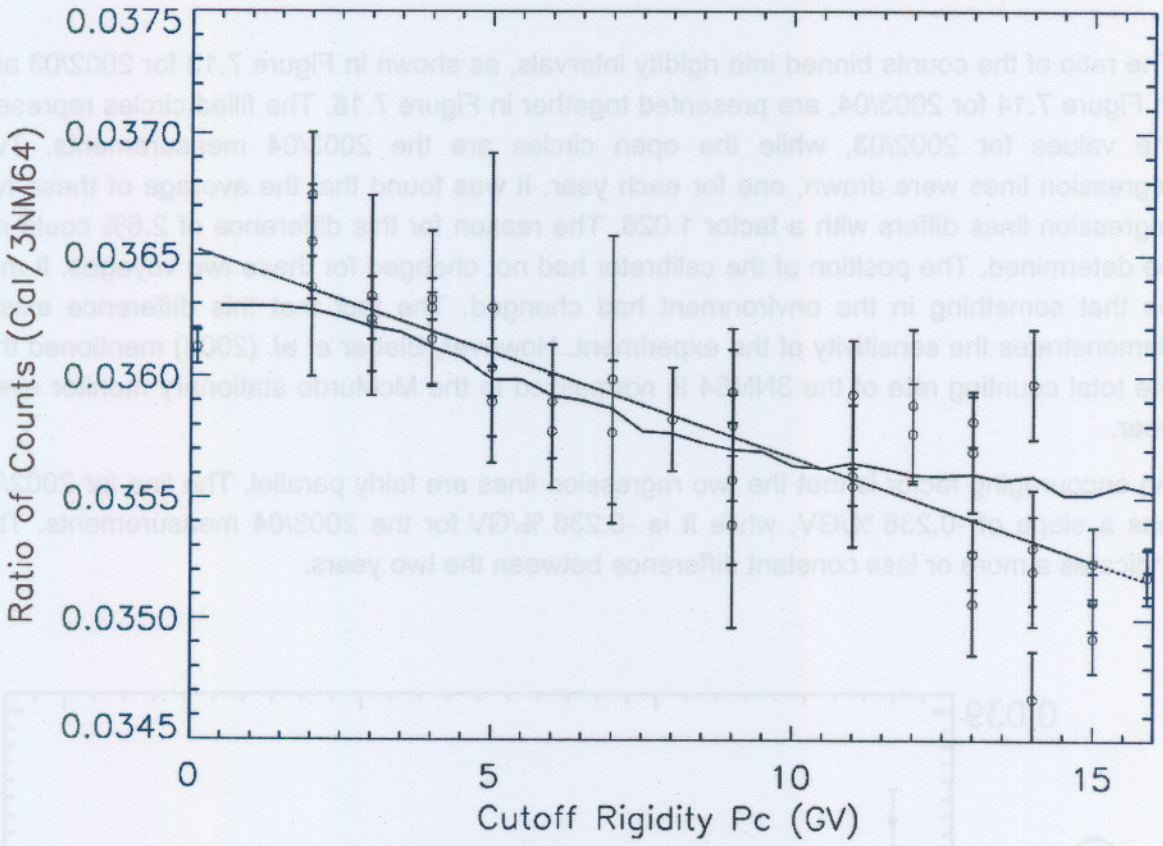

Figure 7.14: The counting ratios binned into rigidity intervals for 2003/04.

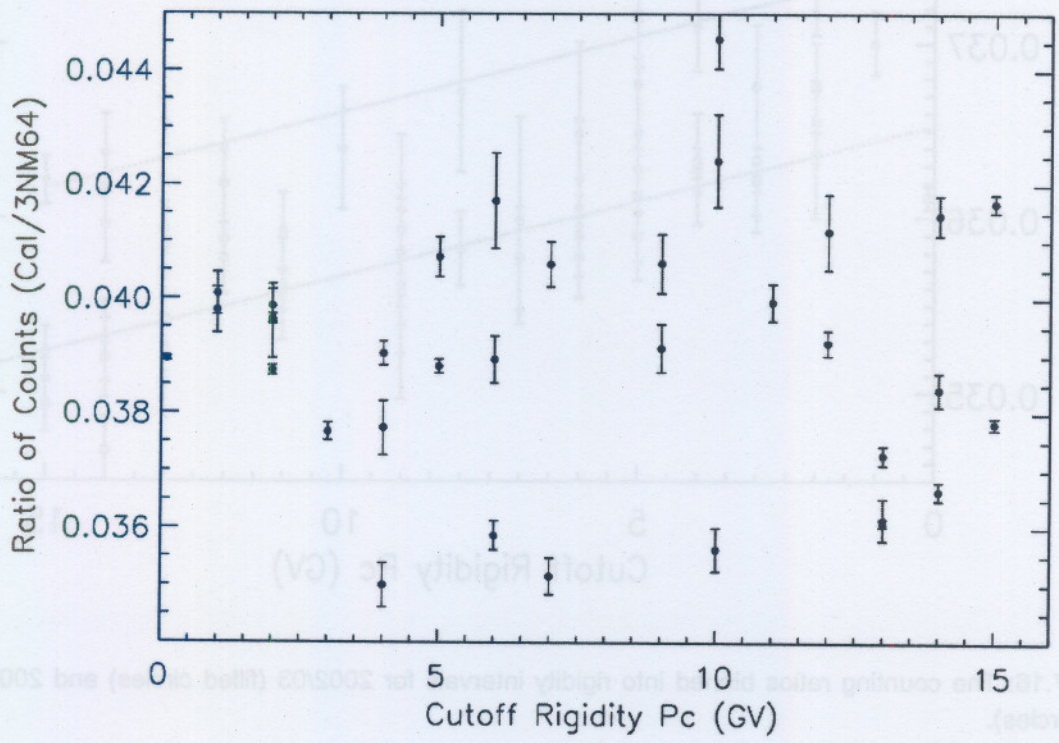

Figure 7.15: The latitudinal response for 2004/05 for the counting ratios binned into rigidity intervals.

The ratio of the counts binned into rigidity intervals, as shown in Figure 7.13 for 2002/03 and in Figure 7.14 for 2003/04, are presented together in Figure 7.16. The filled circles represent the values for 2002/03, while the open circles are the 2003/04 measurements. Two regression lines were drawn, one for each year. It was found that the average of these two regression lines differs with a factor 1.026. The reason for this difference of 2.6% could not be determined. The position of the calibrator had not changed for these two voyages. It may be that something in the environment had changed. The fact that this difference exists, demonstrates the sensitivity of the experiment. However, Bieber *et al.* (2003) mentioned that the total counting rate of the 3NM64 is normalised to the McMurdo stationary monitor every year.

An encouraging factor is that the two regression lines are fairly parallel. The line for 2002/03 has a slope of -0.238 %/GV, while it is -0.236 %/GV for the 2003/04 measurements. This indicates a more or less constant difference between the two years.

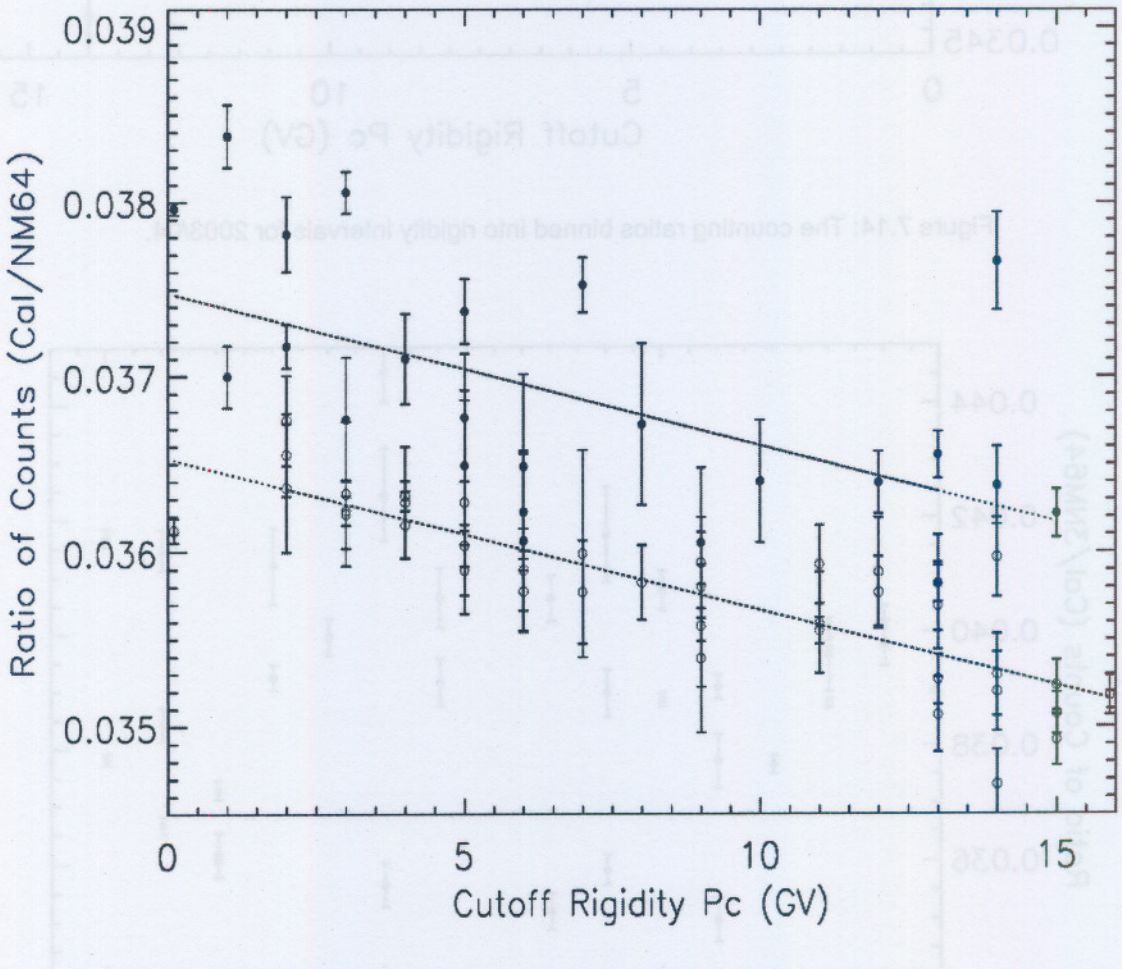

Figure 7.16: The counting ratios binned into rigidity intervals for 2002/03 (filled circles) and 2003/04 (open circles).

A less encouraging factor shown in Figure 7.16 is the difference of ~5% between the two points at 0.1 GV, when the monitors were at and near McMurdo, Antarctica. This difference is twice as large in comparison with the 2.6% difference of the total average measurements of the two years. To look in more detail at these two points, these counting ratios are represented as function of the day number at McMurdo in Figure 7.17. All these values should in principle be the same, since at these low rigidities the counting rate is determined by the atmospheric cutoff, which is ≈ 1.5 GV.

Inspection of Figure 7.17 shows that there are, unfortunately, only 8 data points (open circles) for 2003/04, due to the breakdown of the hard disk of the calibrator mentioned earlier. The average of the 2002/03 and 2003/04 measurements are shown by the dotted lines and are 0.0380 ± 0.0009 and 0.0362 ± 0.0002, respectively. This rather large scatter of 7.7% for 2002/03 and the difference of 5% between the average values of 2002/03 and 2003/04 are of concern, because it is much larger than the desired accuracy and repeatability of < 0.2%.

Figure 7.16 shows more than one data point for most cutoff rigidity intervals. To determine only one point per rigidity interval for the two voyages, the data have to be normalised. The 2002/03 ratios were normalised to those of 2003/04, by dividing the former by 1.026. This normalising factor was calculated by dividing the averages of the two regression lines.

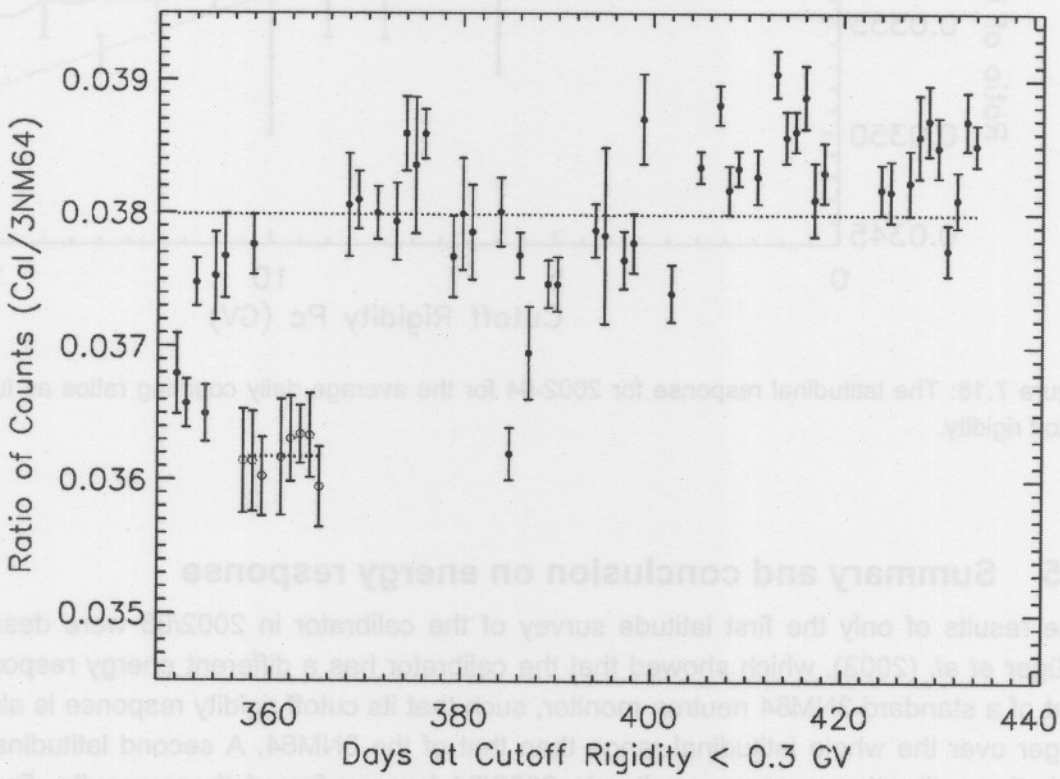

Figure 7.17: The average daily ratios for 2002/03 (see Figure 7.9), indicated by filled circles, and for 2003/04 (see Figure 7.10), indicated by open circles, for the days at cutoff rigidity of less than 0.3 GV.

Thereafter, all the ratios in a given interval were averaged into one single point per rigidity interval, as represented in Figure 7.18. The dotted line represents a linear regression, with a slope of -0.24 %/GV. The continuous curve in this figure indicates the initial calculated ratio for the two monitors, as in Figure 7.6. These calculated values were normalised by the quotient of the average of the regression line and the average of these calculated values, as before, and is determined as 2.416. The regression line lies encouragingly near the Clem calculation (continuous line). The dashed lines show the newest Clem simulations, as described in Section 7.3 and Figure 7.7. There was also a free normalisation of 1.04867.

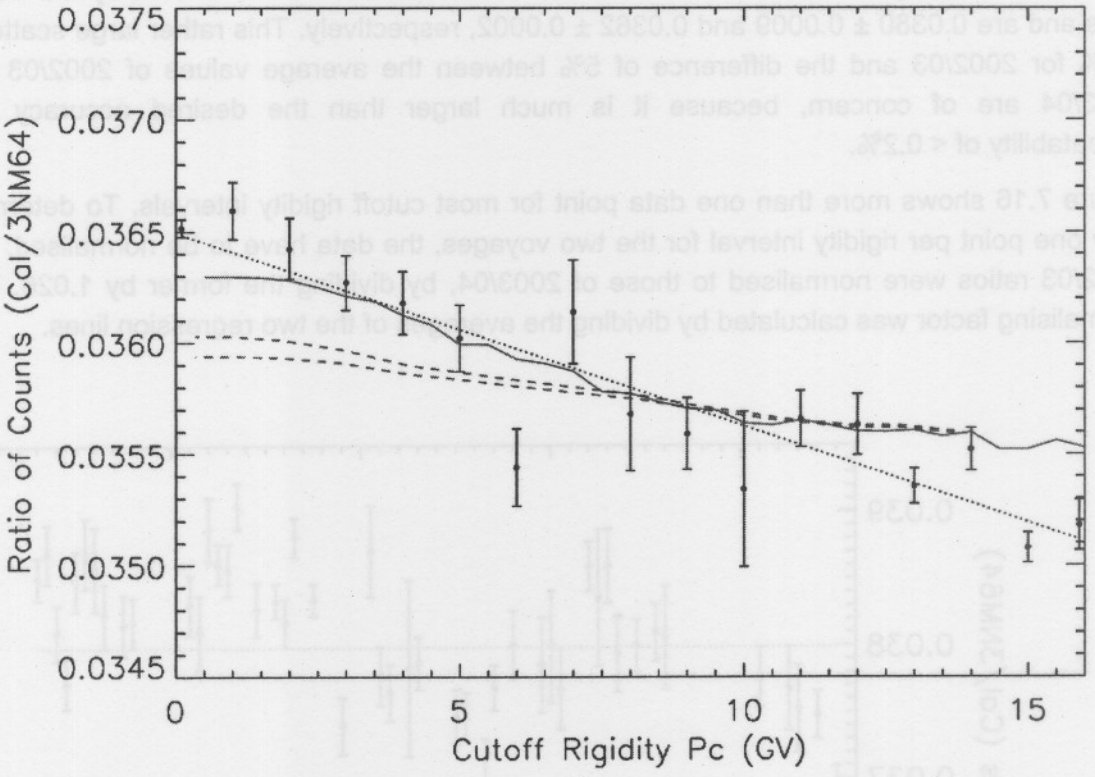

Figure 7.18: The latitudinal response for 2002-04 for the average daily counting ratios as function of cutoff rigidity.

7.5 Summary and conclusion on energy response

The results of only the first latitude survey of the calibrator in 2002/03 were described in Krüger *et al.* (2003), which showed that the calibrator has a different energy response than that of a standard 3NM64 neutron monitor, such that its cutoff rigidity response is almost 4% larger over the whole latitudinal range than that of the 3NM64. A second latitudinal survey with the calibration neutron monitor in 2003/04 has confirmed these results. Due to the relatively large statistical errors for the counting ratio as function of cutoff rigidity, it was decided to send the calibrator on another voyage. During the third one, in 2004/05, there was a problem with the pre-amplifier, which rendered the results unreliable. Due to circumstances with the survey vessels, the next journey planned for 2005/06 did not take place.

When improved measurements are obtained with a next survey, the differential response function of the calibrator can be calculated, such as done in Figure 7.2.

The data measurements obtained during the first two surveys were compared with two sets of simulations done by Clem, as shown in Figure 7.18. These simulations differ significantly from one another. For the one set a conceptual design of the calibrator, different from the final one, was used, and the response for only vertical incident protons and neutrons was calculated. This simulation compares reasonably well with the experimental data. In the case of the second simulation, the actual design of the calibrator was used and the response for most vertical incident particles was calculated, but this simulation agrees much worse with the data.

Therefore, at least one more survey is desired during the 2006/07 season to reduce statistical uncertainties further, while the simulations should also be extended to try to reduce their difference with the observations.

Chapter 8
Statistical and Reliability Considerations for Calibration

8.1 Introduction

In Chapter 5 it was argued that to derive useful differential response functions from the intercalibrated network of neutron monitors, the overall accuracy of counting rates should be within 0.1 – 0.2%. This error margin will evidently be a combination of statistical and systematic errors.

The systematic effects that cause fluctuations in the neutron monitor counting rate are changes in the

- production spectrum and galactic propagation,
- heliospheric propagation,
- atmospheric propagation (pressure variations and temperature effects),
- environmental properties,
- instrumental properties of neutron monitors, and
- production of secondary neutrons in neutron monitors, which causes the counting rates not to be independent of one another, and is called the multiplicity effect.

The work that was done in this project to assess these uncertainties and their origins is discussed in this and the following two chapters. The present chapter focuses mainly on the statistical accuracy of the calibrator, as modified by the multiplicity effect, while Chapters 9 and 10 are devoted to environmental effects, such as temperature sensitivity and the influence of different surfaces, respectively.

8.2 Statistical errors in experiments

There are statistical inaccuracies in the counting rate of a neutron monitor. In an experiment that records N_i counts per time interval, repeated n times (the number of events or experiments), the arithmetic mean (or average), standard deviation, and standard deviation (error) on the mean are, respectively, given by:

$$\bar{N} = \frac{1}{n}\sum_{i=1}^{n} N_i ,$$

$$s = \sqrt{\frac{\sum_{i=1}^{n}(N_i - \bar{N})^2}{n-1}} , \text{ and}$$

$$\bar{s} = \frac{s}{\sqrt{n}} .$$

The coefficient of variation, i.e. the fractional standard deviation in N, measures the standard deviation relative to the mean:

$$s^* = \frac{s}{\bar{N}}. \tag{8.1}$$

When the measurements are statistically independent of each other they are Poisson distributed, according to

$$P(N_i) = \frac{\bar{N}^{N_i}}{N_i!} e^{-\bar{N}}. \tag{8.2}$$

For a Poisson distribution the standard deviation and the coefficient of variation are

$$s_p = \sqrt{\bar{N}} \quad \text{and} \quad s_p^* = \frac{1}{\sqrt{\bar{N}}}. \tag{8.3}$$

According to Hatton (1971), the coefficient of variation of the counting rates is 0.8% on the hourly data for a typical IGY with 12 counters, and 0.16% for a 18NM64 at sea level at high latitudes. The statistical errors per hour registration on currently operating neutron monitors in the worldwide network are listed by Moraal *et al.* (2000) and Dorman (2004).

8.3 Additional factors causing fluctuations of counting rates

Information about the heliosphere and galaxy has to be interpreted from cosmic ray counting rates and intensities. As mentioned in the introduction, apart from statistical fluctuations in cosmic ray intensities, the following fluctuations in the counting rate will cause a variation larger than the Poisson variation: (a) fluctuations in the primary spectrum, (b) atmospheric effects and (c) multiplicity effects in the neutron monitor.

8.3.1 Primary intensity variations

The purpose of cosmic ray measurements is to study the physical processes that influence the primary cosmic ray flux immediately above the atmosphere. Those that are well understood can be corrected for, so that other, usually smaller effects, can be investigated.

Although the generation of cosmic rays in the galaxy is not constant, the production and galactic propagation effects are probably stable over long periods of time in the galaxy, and therefore should have no significant effect on time scales of up to hundreds of years.

The propagation of the particles through the heliosphere depends on many factors. The dominant heliospheric fluctuations are due to the 22-year heliomagnetic and 11-year heliographic cycles (described in Section 2.3.2), which cause intensity variations of ~10% in the equatorial regions, with $P_c \approx 15 - 17$ GV, and as much as 20% in the polar regions, where $P_c << 1$ GV. However, these fluctuations are too slow to have an effect on the evaluation of statistical performance and calibration considerations.

Gil *et al.* (2005) determined that the average amplitudes of the 27-day variation in the galactic cosmic ray primary intensity are ~0.4% for solar minimum periods and ~0.6% for solar maximum periods.

Variations due to Forbush decreases are typically ~10%/day. Large decreases can reach up to ~15% in the polar regions, such as occurred in November 2004, with a decrease of ~14% at Sanae, Antarctica, as shown in Figure 2.8. Similarly, ground level enhancements have large increases, such as the one shown in Figure 2.9 that occurred on 20 January 2005, with an increase of ~200% at Sanae, while it reached up to ~3000% at South Pole. These variations are, however, easily identifiable and can be omitted from reliability analyses.

The cosmic ray intensity also varies on the order of days or even hours. The diurnal variation is ~0.5% per 12 hours, considerably larger than the 0.1 – 0.2% statistical accuracy that is required for the calibrator.

There are even shorter-term variations called interplanetary scintillations. Scattering of the cosmic rays by the random fluctuations in the interplanetary magnetic field causes scintillations in the cosmic ray intensities, as studied and described in detail by Owens (1973). He described these scintillations as temporal fluctuations in the counting rate of a detector pointing in a fixed direction in space. It was found that the fluctuations are much larger than would be expected if there had been only statistical (Poisson) noise.

When these primary intensity variations occur over the time-span of the calibration or less, they may seem to contribute to the statistical fluctuations of the counting rate. In this sense, the diurnal variation and short-term scintillations are the most important.

8.3.2 Atmospheric (pressure and temperature) variations

Atmospheric pressure and temperature effects need to be taken into accounts, since they make similar contributions to the fluctuations. The decay of the primary particles into secondaries occurs in a dynamic atmosphere. Meteorological effects influence the transport of particles through the atmosphere. It is important to understand these effects and, where necessary, corrections have to be made.

8.3.2.1 Pressure variations

The most important meteorological effect is the well-known pressure effect.

The mass of air above a monitor changes and influences particle transport, e.g. through change in absorption of the secondary particles and particle decay. This leads to a change in the counting rate. The barometric pressure recorded at a station is a good measure of this mass of air. The correction factor is known as the attenuation or barometric coefficient and is defined by the relation

$$\frac{dN}{N} = -\beta dP,$$

where dN = change in the counting rate N,

β = barometric coefficient, and

dP = change of the atmospheric pressure.

The counting rate, N, can thus be corrected by the integral expression

$$N = N_0 e^{\beta(P_0 - P)}, \qquad (8.4)$$

where N_0 = the counting rate at a reference pressure P_0.

Typical values of the barometric coefficient are $\beta \approx 1\%$/mm Hg. It is, however, a function of altitude/pressure, latitude and solar activity, as experimentally investigated, for example, by Raubenheimer and Stoker (1974). Clem *et al.* (1997) corrected their data from a sea level latitudinal survey conducted from December 1994 to April 1995, to a standard pressure of 760 mm Hg using a barometric coefficient that varies with cutoff rigidity as $\beta = 0.983515 - 0.00698286\ P_c$. This expression was derived empirically from a fit to pressure coefficients obtained by 11 neutron monitors near sea level with various cutoff rigidities.

Dorman (2004, and references therein) described the variation of β with the solar cycle. This is to be expected, because the decrease of solar activity in the 11-year cycle leads to an increase of cosmic ray intensities (see Chapter 2) and therefore to a softening of the spectrum of observed galactic cosmic rays and, consequently, an increase in β. This variation has been observed, e.g. during the 1954 – 1965 cycle, to vary between 3% and 8% at different venues. Furthermore, this variation was confirmed by determining the barometric coefficients for the same 3NM64 on its latitudinal survey as described by Clem *et al.* (1997), but this time for selected periods during January and February 2003 at McMurdo. The value at this period of higher solar activity was $\beta = 1.03$ %/mm Hg, in comparison to $\beta \approx 0.98$ %/mm Hg, as in the above-mentioned paragraph. For the same data points, the barometric coefficient for the calibrator was $\beta = 1.05$ %/mm Hg, which confirms the result of Figure 7.7 in Section 7.3 that the calibrator measures a softer energy spectrum than the 3NM64.

Dorman (1974) showed that wind speed has to be taken into account when applying the corrections for the barometric effect. Due to the Bernoulli effect, when the wind blows, static pressure measurements are not an accurate measure of the column density of air above the neutron monitor. Malan and Moraal (2002) studied this effect on the Sanae neutron monitor counting rate. Neutron monitors have typical counting rates of ~$10^5 – 10^6$, and thus statistical uncertainties of 0.3% – 0.1%. If $\beta = 1\%$ /mm Hg, this means that atmospheric pressure must be known accurately to about 0.1 – 0.3 mm Hg. The authors showed, however, that pressure-corrected hourly counting rates during windy conditions could have uncertainties up to ≈ 1.5%, which is about 10 times the needed statistical uncertainty.

8.3.2.2 Atmospheric temperature effects

There are two types of temperature effects for neutron monitors, namely atmospheric and instrumental. The atmospheric effect is discussed here, while the latter came to our attention during experiments done in recent years and is described in detail in Chapter 9.

The neutron monitor counting rate depends not only on the mass of the atmosphere above the monitor (pressure effects), but also on the mass distribution in the atmosphere, which varies with temperature changes (Harman and Hatton, 1968). This atmospheric temperature effect on a neutron monitor is caused by unstable secondary particles, muons and pions, with relatively short lifetimes. A change in the air density will change the time of flight of these unstable particles.

According to Hatton (1971), only the temperature close to the monitor is relevant to the number of interacting pions because of their short lifetime. The pions give rise to a negative temperature effect, because an increase in the temperature causes an increase in their

probability of decay, so that the number of pions recorded by the neutron monitor decreases. In addition, they also cause a positive temperature effect due to the increased muon production from pion decay. On the other hand, when the atmosphere warms, it expands and the paths for traversing the same depth of matter increase and fewer muons reach the monitor, giving rise to a negative temperature effect.

Hatton (1971) stated that the negative temperature effect for interacting muons in the neutron monitor exceeds the positive temperature effect due to the increased muon production from pion decay. Thus, an increase in the temperature of a particular level in the atmosphere decreases the counting rate of a neutron monitor.

According to Iucci *et al.* (2000), this atmospheric temperature effect ranges from ~ – 0.037 %/°C at the poles to ~ – 0.066 %/°C at the equator. It also decreases in magnitude with increasing altitude. It is clearly less important than the barometric effect, but it becomes significant in the consideration of calibration accuracies for temperature changes > ~5°C.

8.3.3 Environmental and instrumental noise

Environmental effects were also investigated in this study, but they are described separately in Chapter 10. These effects, as well as instrumental effects, should be avoided as far as possible.

8.3.4 Multiplicity effects

For Poisson statistics to apply, each event has to be completely independent of the other. As Bachelet *et al.* (1964) mentioned, this is valid when the arrival of particles is random in time, but not when there is a multiplicity effect. Due to this effect, Dyring (1962) showed that the multiplicity gives a larger standard deviation than expected from the Poisson distribution.

The multiplicity effect in a standard cosmic ray neutron monitor is described e.g. by Bachelet *et al.* (1964), Hughes *et al.* (1964), Hatton and Carmichael (1964) and Hatton (1971). The evaporation neutrons produced in a neutron monitor can be detected separately by the counters, due to the spread in time of their arrival at the counters. As discussed in Chapter 4, lead produces about 8-10 evaporation neutrons per incident nucleon. The detection efficiency per neutron in the counters is ~6%. Since the typical amplifier dead time for a neutron monitor (~20 μs) is much less than the average lifetime of neutrons (~300 μs), more than one neutron per event may be counted.

Hatton (1971) gave the relation between the total counting rate N, the event rate $R(m)$ in which m neutrons are detected, and the mean detected multiplicity $\bar{m}$, as

$$N = \sum_{1}^{\infty} mR(m),$$

$$R = \sum_{1}^{\infty} R(m), \quad \text{and}$$

$$N = \bar{m}R.$$

Thus, the average detected multiplicity $\bar{m} = N/R$ = number of counts (neutrons) / number of events.

This detected multiplicity is to be distinguished from the produced multiplicity $\bar{\nu}$. Shen (1968) showed that the relationship between the two is

$$\bar{\nu} = \left(\frac{\bar{m} - 1}{\varepsilon f} \right),$$

where ε = neutron detection efficiency of the counters, and

f = the gating efficiency of the electronics, obtained by measuring the time distribution of the detected neutron pulses, as described by Hatton (1971).

Hatton and Carmichael (1964) measured the multiplicity spectrum up to $\bar{\nu}$ =10 electronically with gating circuits, and obtained an average detected multiplicity $\bar{m}$ of 1.41 ± 0.02 for the 6NM64, in comparison with the value of 1.23 for the IGY monitor. Hatton (1971) confirmed these values experimentally. The larger value obtained for the 6NM64 reflects that it has a greater efficiency than the IGY.

Hatton (1971) also summarised the contributions made by various components of the cosmic radiation to the observed multiplicity spectrum in an IGY and a 6NM64 neutron monitor. He concluded from the results that the multiplicity spectrum is dominated by neutron interactions for low multiplicities, but for high multiplicities (> 5 in the IGY and > 7 in the NM64) proton and pion interactions become important. Muon interactions produce low multiplicity events.

According to Hatton (1971), $\bar{m}$ increases slightly with decreasing cosmic ray intensity and the magnitude of this variation at Oulu (Finland) is ~0.05% decrease in the observed counting rate. The value of the average multiplicity has been found to increase with decreasing latitude, being 1.89% larger at the equator (17 GV) than at high latitudes (< 1 GV). He mentioned that it also increases with altitude because of an increase in the average energy of the secondary particles. Dorman (2004) confirmed this latitudinal effect, measuring an average increase of 0.11 %/GV.

Due to these multiplicity effects, the fluctuations in the counting rate will be larger than the Poisson deviation (8.3):

$$s^* = K_m s_p^* = \frac{K_m}{\sqrt{\bar{N}}}. \qquad (8.5)$$

Apart from multiplicities, fluctuations in the primary spectrum, as well as fluctuations due to atmospheric effects, mentioned in Section 8.3.1 and 8.3.2, cause an even higher coefficient of variation, i.e.

$$s^* = K s_p^* = \frac{K}{\sqrt{\bar{N}}}, \text{ with } K > K_m. \qquad (8.6)$$

The essence of the calibration procedure is to compare the counting rate of the calibrator with that of a stationary neutron monitor. In such a procedure the effects of primary intensity variations and atmospheric effects should be entirely eliminated, since the two monitors sample the same cosmic ray population. The only effect that increases the standard deviation above the Poisson value will then be the multiplicity effect, through K_m.

This principle has been employed for many years, starting with Dyring (1962), to test the performance and stability of neutron monitors, simply by analysing the counting ratios of its different sections. If covariance effects between the two sections are negligible, the standard deviation on the ratio of two instruments with counting rates N_1 and N_2 is

$$s\left(\frac{N_1}{N_2}\right) = \sqrt{(s_1)^2 + (s_2)^2}\ . \tag{8.7}$$

In a neutron monitor with two similar sections, where $s_1 \approx s_2$, this reduces to

$$s\left(\frac{N_1}{N_2}\right) = \sqrt{2}K_m s_p\ , \tag{8.8}$$

where s_p = Poisson deviation for either of the sections.

As mentioned, two monitors at the same place measure the same fluctuations in the primary spectrum and are subject to the same atmospheric conditions. The ratio of two such counting rates should therefore only reflect the increase in fluctuation due to the multiplicity effect. Dyring (1962) divided his IGY monitors at Uppsala, Murchison Bay and Mt. Wellington, and Hatton (1971) the IGY and 6NM64 at Leeds, into electronic independent sections. The multiplicity coefficient K_m was determined, using (8.7) and (8.8). Their results are summarised in Table 8.1.

Hatton and Carmichael (1964) measured the value of K_m with an electronic multiplicity meter on their 6NM64 neutron monitor and used these results to calculate the coefficient of variation explicitly. Their value is $K_m = 1.38$, listed in the fourth row of Table 8.1.

Furthermore, Villoresi *et al.* (2000) computed the standard deviation on the 3-hourly intensity data for the latitudinal survey during 1996 – 1997 with a 3NM64. They then computed the value of K defined in (8.6). They did not use the ratio method, but rather the method described in Section 8.4. They contended that this should be equivalent to K_m, because they made corrections for all known primary variations and atmospheric effects.

Table 8.1: Multiplicity coefficient K_m determined experimentally

Venue	Neutron monitor	K_m	Reference
Uppsala-Murchison Bay	IGY	1.18 ± 0.01	Dyring (1962)
Mt. Wellington	IGY	1.25 ± 0.02	Dyring (1962)
Leeds	IGY	1.23 ± 0.02	Hatton (1971)
Deep River	6NM64	1.38	Hatton and Carmichael (1964)
Leeds	6NM64	1.52 ± 0.02	Hatton (1971)
Latitudinal survey: Italy – Antarctica	3NM64	1.1 for $P_c > 6$ GV 1.6 for $P_c < 4$ GV	Villoresi *et al.* (2000)

The K_m values obtained for the three IGY monitors in Table 8.1 are in general agreement. The 6NM64 values are significantly larger because of the higher average multiplicity. The value for the 6NM64 measured at Leeds is significantly larger than the value measured with the multiplicity meter at Deep River. This may be due to three reasons. Firstly, Hatton (1971) mentioned that only multiplicities up to m = 10 were taken into account for the Deep River experiment. Secondly, although the ratio method is designed to eliminate all primary and atmospheric contributions, two sections will still count different nuclei from the same shower, or different evaporation neutrons produced from the same nucleon (in the lead producer). Therefore, it may be that the ratio method measures rather K instead of K_m. Thirdly, according to Hatton and Carmichael (1964), the value of K_m is not constant for one particular neutron monitor, because it probably depends upon latitude, altitude and epoch.

Finally, the values obtained by Villoresi *et al.* (2000) were for a 3NM64. They mentioned that the reason for the difference in values for $P_c > 6$ GV and $P_c < 4$ GV is probably that the variations due to meteorological effects were particularly large at $P_c < 4$ GV and that the correction for primary variations could not be fully applied. The counting rate of a high latitudinal neutron monitor is approximately twice that of an equatorial one. Since physically induced fluctuations are smaller at the equatorial, high cutoff regions, it naturally implies from (8.6) that $K_{eq} > K_{pole}$.

In the next sections, K is measured for the calibrator and the 6NM64 at Sanae, and then, under different conditions, for the calibrator, a 1NM64 and the 15-tube IGY in Potchefstroom.

8.4 Measurement of standard deviations at Sanae

The first intercalibration with one of the two calibrators was done at Sanae, Antarctica, in December 2002 and January 2003 (Moraal *et al.*, 2003). The full procedure and measurements for 9 separate runs are described in greater detail in Chapter 9.

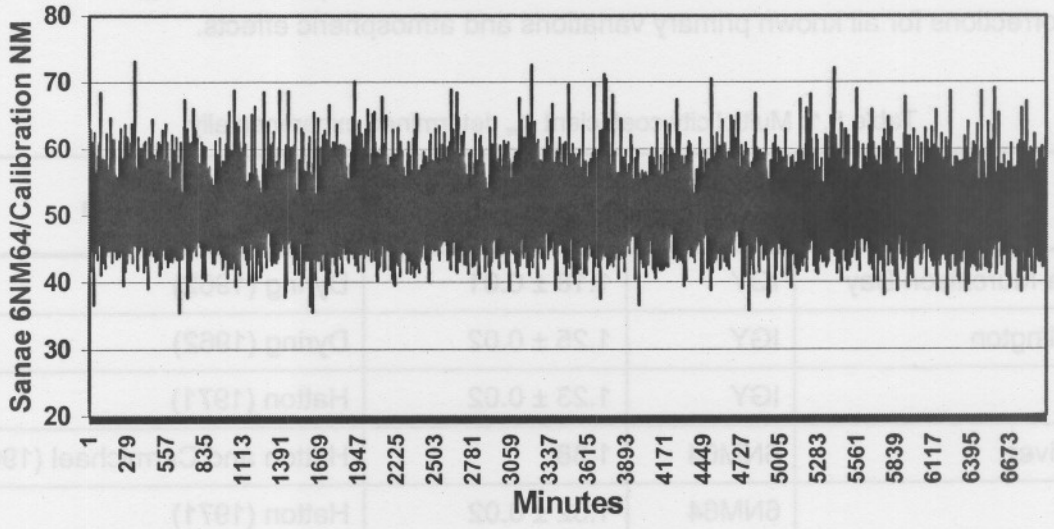

Figure 8.1: The counting ratio of the 6NM64 and calibrator, for run #2, at Sanae, Antarctica, for day 360-365 of year 2002.

A typical example of a run at Sanae is shown in Figure 8.1. In this figure the ratio of the counting rates of the 6NM64 and calibrator is plotted as function of time (in minutes). The total number of counts of the calibrator for this period was 1 131 111, with an average counting rate of ≈ 160 counts per minute and an average ratio of 50.846.

Each of the 9 runs contained ~10^6 counts, so that, according to (8.3), the coefficient of variation on each set should be 0.1% if the counts were independent of one another, i.e. distributed according to the Poisson distribution.

The average $\bar{N}$, and the range $\bar{N} \pm s$ that contains 68% of the 1-minute counts, were determined. This range is noted for each of the 9 runs in Table 8.2 as a multiple of the Poisson deviation of 0.1%, i.e. the value K in (8.6). The same procedure was followed for the 6NM64. This procedure was done for both uncorrected and pressure corrected counting rates (see Section 8.3.2.1). No temperature corrections were made, because its influence was not significant.

Table 8.2: Measured standard deviation / Poisson deviation (K) at Sanae
Adapted from Moraal *et al.* (2003)

Calibration Number	Pressure Difference	K uncorrected		K corrected	
		Calibrator	6NM64	Calibrator	6NM64
1	18 mb	1.34	3.93	1.23	1.79
5	15 mb	1.28	3.34	1.26	1.72
7	15 mb	1.27	2.97	1.24	1.74
8	12 mb	1.26	3.31	1.23	1.70
3	11 mb	1.26	2.94	1.22	1.54
6	10 mb	1.27	2.83	1.27	1.63
9	6 mb	1.23	2.22	1.17	1.89
4	6 mb	1.25	2.04	1.25	1.61
2	4 mb	1.25	1.78	1.26	1.97
Average		**1.268±0.031**	**2.82±0.69**	**1.237±0.030**	**1.73±0.14**

The deviation ranges in the two middle columns vary considerably from one run to the next, especially for the 6NM64. This variation is mainly due to the different pressure variations during each of the runs. Therefore, the 9 runs (experiments) are arranged in the table according to the spread of the pressure variation. It can be clearly seen that the size of the deviation correlates with this pressure variation during each experiment. The deviation of the 6NM64 is much larger than that of the calibrator, because the counting rate of the 6NM64 is about 50 times that of the calibrator. Therefore, the size of the systematic variations, relative to the Poisson variations, should be much more pronounced on the 6NM64.

The above argument is substantiated when the counting rates are corrected with (8.4) for these pressure variations. The last two columns of Table 8.2 now show that (1) both the deviation ranges are reduced, (2) these ranges are not correlated with the pressure ranges anymore, and (3) the average value of the 6NM64 (1.73 ± 0.14) is still significantly larger

than the average value (1.237 ± 0.030) of the calibrator. The first two points indicate that the procedure works properly, while the value for the 6NM64 is only marginally larger than the value of 1.52 ± 0.02 obtained by Hatton (1971) in Table 8.1.

Finally, the coefficient of variation of the counting ratios, s^*, was determined from these K-values. From (8.3) the coefficient of variation of a Poisson distribution is 0.1% on 10^6 counts, and the 6NM64 counts 50 times more than the calibrator. Thus, using (8.7):

$$s^* = \sqrt{1.237^2 + (1.732/\sqrt{50})^2} * 0.1\% = 0.14\%.$$

Therefore, with 10^6 counts the calibration accuracy will be ± 0.14%.

8.5 Reliability tests at Potchefstroom

8.5.1 Coefficient of variation

The entire procedure was repeated in Potchefstroom in 2003 to test the method and its assumptions.

Here, the calibration monitor was placed in two different positions, one in the monitor hut together with the IGY, on the roof of the Physics building of the Potchefstroom campus of the North-West University. It is a building of 4 storeys. The other position, called the Sanae room, is inside the building, but on the same level as the monitor hut. The total amount of counts was again approximately 10^6 for each run.

Firstly, the K-values were obtained in the same way as for the calibrator and 6NM64 at Sanae, to determine the reliability of the counting rate of the calibrator and IGY. The same arguments apply as for the Sanae calculations.

Table 8.3: K-values for calibrator and IGY at Potchefstroom

Calibration Number	Days of 2003	Location	Pressure Difference	K Uncorrected		K Corrected	
				Calibrator	IGY	Calibrator	IGY
1	237-241	Inside hut	15 mb	1.28	1.99	1.23	1.53
2	242-246a	Inside hut	8 mb	1.26	1.67	1.24	1.53
3	246b-251	Inside hut	11 mb	1.22	1.79	1.24	1.51
4	253-259	Sanae room	11 mb	1.23	1.77	1.20	1.54
Average				**1.251±0.028**	**1.80±0.14**	**1.226±0.019**	**1.526±0.012**

As for Sanae, the one-second recordings of the calibrator's counts were binned into 1-minute intervals; yielding $N_i \approx 150$ counts per minute, with a total of $\approx 10^6$ counts for each run. The average $\bar{N}$, and the range $\bar{N} \pm s$ that contains 68% of the 1-minute counts, were determined. This range is noted for each of 4 runs in Table 8.3 as a multiple of the Poisson deviation of 0.1%. The same procedure was followed for the IGY.

The corrected value, K = 1.226 ± 0.019, for the calibrator agrees with the value measured at Sanae in Table 8.2. Also, the IGY value of 1.526 ± 0.012 is significantly larger than the three K_m-values of Table 8.1, as expected.

The coefficient of variation of the counting ratios was determined in the same way as for the calibrator and 6NM64 in Sanae. The IGY counts about 16 times more than the calibrator. By using the pressure corrected average coefficient of variation of the counting rates of the calibrator and IGY, as shown in Table 8.3, the coefficient of variation of the counting ratios is

$$s^* = \sqrt{1.226^2 + (1.526/\sqrt{16})^2} * 0.1\% = 0.13\%.$$

Thus, with 10^6 counts the calibration accuracy will be ± 0.13%. Although the K-value of the Potchefstroom IGY is very different from that of the Sanae 6NM64, the two statistical accuracy numbers are similar, which demonstrates that the method works correctly.

Outside, on the roof, just north of the monitor hut, a 1NM64 counter also records cosmic rays. Its K- value was also calculated, in the same way as for the calibrator and IGY, as being 1.36.

In conclusion, the results of the K-values calculated for the neutron monitors are shown in Table 8.4, and in Figure 8.2, together with the counting rates relative to those of the calibrator. As expected, the K-values increase with the counting rate, because the systematic variations are then more pronounced relative to the Poisson fluctuations.

Table 8.4: Comparison of K-values

	Calibrator	1NM64	IGY	6NM64 (Sanae)
Counting ratio	1	7	16	50
K-value	1.23	1.36	1.53	1.73

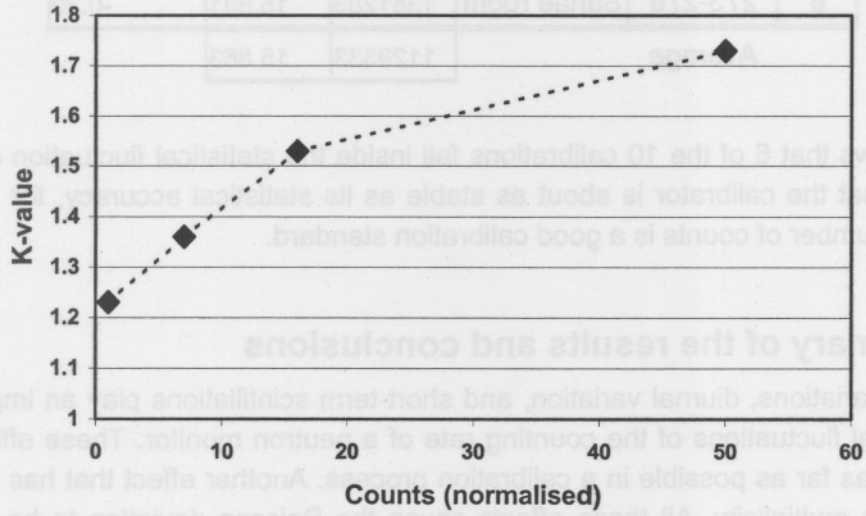

Figure 8.2: The experimental K-values, obtained at Potchefstroom and Sanae, as function of the counting rates relative to those of the calibrator.

8.5.2 Stability of the calibrator

Having established that the statistical fluctuations on a calibration with 10^6 counts for the calibrator should be in the range of ± 0.13% to 0.14%, several tests were done to test the repeatability. The reason was to determine the stability or consistency of the calibration neutron monitor. Ten runs, with a total of ~10^6 counts each, were done with the calibrator either inside the monitor hut or in the Sanae room, at a constant temperature. For each of these two positions the counting ratio (IGY/Calibrator), and also the average value of this ratio, were determined five times. The deviation of each individual value was then compared with the average, as shown in Table 8.5.

Table 8.5

Cal. Nr	Days of 2003	Location	Total Counts	Ratio	% Deviation
			Cal	IGY/Cal	IGY/Cal
1	237-241	Inside hut	955896	16.459	-0.83
2	242-246a	Inside hut	981447	16.582	-0.09
3	246b-251	Inside hut	975990	16.589	-0.05
9	279-284	Inside hut	1164467	16.778	1.09
10	285-289a	Inside hut	946901	16.578	-0.12
	Average		1004940	16.597	
4	253-257	Sanae room	1028493	15.884	0.13
5	258-262	Sanae room	1047115	15.906	0.27
6	263-267	Sanae room	1055252	15.841	-0.14
7	268-272	Sanae room	1134520	15.853	-0.06
8	273-278	Sanae room	1381283	15.831	-0.20
	Average		1129333	15.863	

Table 8.5 shows that 6 of the 10 calibrations fall inside the statistical fluctuation of ≈ 0.13%. This implies that the calibrator is about as stable as its statistical accuracy, for 10^6 counts, and that this number of counts is a good calibration standard.

8.6 Summary of the results and conclusions

Atmospheric variations, diurnal variation, and short-term scintillations play an important part in the statistical fluctuations of the counting rate of a neutron monitor. These effects should be eliminated as far as possible in a calibration process. Another effect that has to be taken into account is multiplicity. All these effects cause the Poisson deviation to be larger than expected.

After the counting rates of the 6NM64 and the calibrator at Sanae had been corrected for pressure, the average K-values calculated are (1.73 ± 0.14) and (1.24 ± 0.03), respectively. In the case of the IGY and calibrator at Potchefstroom, the average K-values obtained are (1.53 ± 0.01) and (1.23 ± 0.02), respectively. As shown in Table 8.4, the K-values increase with the counting rates of the monitors. These values also correspond well with the K_m-values obtained for other monitors, shown in Table 8.1.

When all the effects are taken into consideration, the coefficient of variation is given by (8.6). When all effects are eliminated except the multiplicity effect, the coefficient of variation is given by (8.5). The coefficient of variation determined for the calibrator at Sanae is 0.14% for 10^6 counts, and 0.13% at Potchefstroom, i.e. 30 – 40% larger than that of the Poisson distribution of 0.10%.

The stability of the calibrator as tested in Potchefstroom, shows that almost ⅔ of the calibrations of 10^6 counts each, fall inside the statistical fluctuation of 0.13%. This means that a calibration with 10^6 counts gives optimal calibration accuracy.

Further experiments with this calibration neutron monitor at Sanae and Potchefstroom are described in Chapters 9 and 10.

Chapter 9
The Temperature Sensitivity of Neutron Monitors

9.1 Introduction

As mentioned in Chapter 8, the second calibration monitor was taken to Sanae, Antarctica, between 19 December 2002 and 2 February 2003. The intention was to calibrate the Sanae monitor, but in the course of this execution, an unexpected large instrumental temperature sensitivity was discovered, as reported by Moraal *et al.* (2003). This temperature effect with a magnitude of 0.13 %/^{o}C, where a statistically accuracy of 0.1 – 0.2% is wanted, necessitated a detailed investigation. This effect was subsequently artificially induced at the Potchefstroom campus.

Quite coincidentally, Evenson *et al.* (2005) discovered the same effect, as described in Section 9.8, due to experiences with runaway thermostats at a station.

In this chapter, the measured temperature sensitivities of the calibrator, NM64 and IGY neutron monitors are compared with one another, and with the sensitivities calculated by Clem (2004, private communication).

9.2 Measurements at Sanae

The stationary neutron monitor at Sanae is a standard 6NM64, with $^{10}BF_3$ counters. It was built inside the Sanae-base of the South African National Antarctic Programme, at Vesleskarvet, Antarctica, in 1997. It is 856 m above sea level, at geographic coordinates of 71^{0}40' S and 2^{0}50' W. The cutoff rigidity is 0.75 GV.

9.2.1 Recording of counting rates

The procedure and measurements at Sanae were described in Moraal *et al.* (2003), and are repeated here. H. Moraal conducted the Sanae measurements.

The calibration neutron monitor was placed in three different positions, each repeated 3 times. Approximately 10^6 counts were obtained for each run, as described in Chapter 8. The three positions, with the corresponding runs, are summarised in Table 9.1. The runs were numbered according to consecutive execution. Each run took about 5 days to obtain $\approx 10^6$ counts. The reason for repeating the measurements in the three positions was to test reproducability. In two of the three positions the calibrator was placed inside the same room as the 6NM64, and in the third position it was placed outside the base. The reason for the outside calibration was to determine the effect of the roof, a honeycomb structure of thin fibreglass and pink aerolite.

Table 9.1: Position of calibrator in Sanae

Position number	Number of runs	Description of position of calibrator
1. Inside the base Landing	#1, #4, #9	The centre of the calibration monitor was about 1.5 m south-east of the south-east corner of the stationary 6NM64 and 1.7 m lower than the middle of the counters of the 6NM64 monitor, in the same room. The electronics display faced towards the south.
2. Inside the base High	#2, #6, #7	The centre of the calibration monitor was about 1.6 m south of the western side of the 6NM64 and 0.45 m higher than the centre of the 6NM64, in the same room. The electronics display faced towards the west.
3. Outside the base Outside	#3, #5, #8	The calilbrator stood on the western balloon launching platform, about 2 m from the wall of the base, on the same level as the 6NM64. The electronics head faced east towards the base.

The one-second recordings of the calibrator and 6NM64 were binned into one-minute intervals. The counting ratio, 6NM64/calibrator, was calculated for each minute. No corrections were made for pressure or atmospheric temperature, because the two monitors had the same atmosphere above them. A summary of the average recorded counting ratios for the 9 runs is given in Table 9.2.

Table 9.2: Counting ratios, 6NM64/Calibrator

Position	Round 1	Round 2	Round 3	Average
1 (landing)	53.523 (-0.51%)	53.660 (-0.23%)	54.151 (+0.74%)	53.778
2 (high)	50.846 (+0.22%)	50.719 (-0.03%)	50.638 (-0.19%)	50.734
3 (outside)	50.848 (+0.06%)	50.768 (-0.30%)	50.919 (+0.15%)	50.845

The average ratio for all three rounds at that specific position was calculated, and is shown in the last column of Table 9.2. The percentage deviation of the individual ratio of each round from the average ratio at each position is shown in brackets in each column. In Chapter 8 the statistical and systematic variations for a calibration was determined to be ≈ 0.14%. Consequently, the calibration at position 1, where all three deviations differ much more than 0.14% from the average, was unsuccessful. Moraal *et al.* (2003) gave as probable reason for these large deviations, that position 1 was in the shadow cast by a moving, heavy crane, which caused a varying environment. Furthermore, the counting rate of the calibrator at position 1 is about 6% lower than in position 2, because of the shadow of the 6NM64 cast in position 1. In position 2, where the calibrator was slightly higher than the 6NM64, this

shadow effect was not present. In positions 2 and 3, only 2 of the 6 runs deviate less than 0.14% from the average.

When comparing the ratios of the counting rates of positions 2 and 3, it can be seen that the ratios outside the base at position 3 were, ironically, larger than inside at position 2, for each round. This means that the calibrator counted less outside (denominator larger) than inside. This cannot be, because the roof will absorb some particles.

The explanation for these unsatisfactory and contradictory results was found in the temperature difference between the calibrator and the 6NM64, as will be described in the following section.

9.2.2 Correction for temperature effect

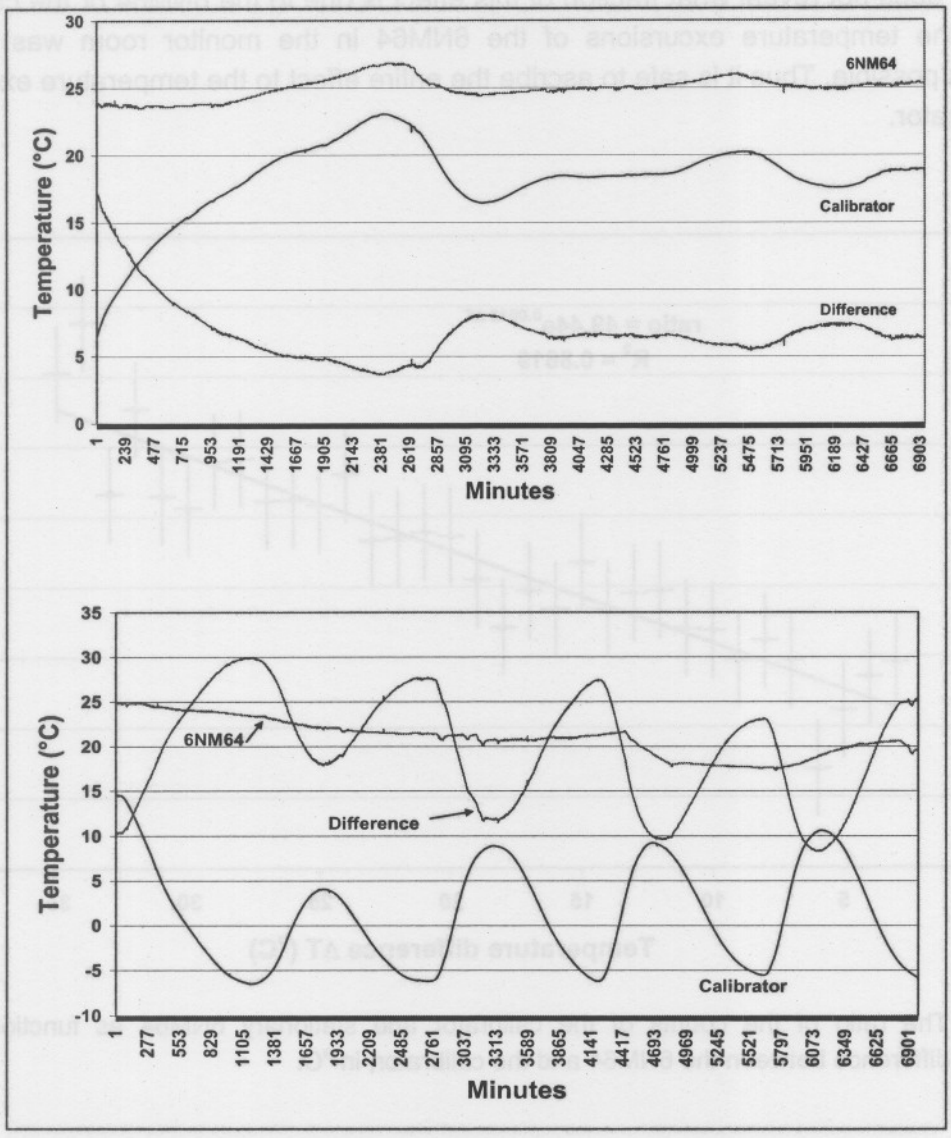

Figure 9.1: The temperatures of the calibrator and the 6NM64, as well as the difference in temperature between these two monitors, for each minute of run numbers 6 and 3. The top panel shows the temperature while the calibrator was stationed with the 6NM64 in the monitor hut (run 6). The bottom panel shows the temperature with the calibrator outside (run 3).

Figure 9.1 shows the temperatures of the 6NM64 in the monitor room, the temperature of the calibrator, as well as the difference in temperature between the two monitors. In the top panel it can be seen that the temperature of the calibrator increased to room temperature and then remained more or less constant. In the bottom panel, when the calibrator stood outside, the temperature varied with a diurnal variation of ± 8 degrees. Temperatures were similarly recorded for all seven other runs.

The ratio of the counts of the calibrator and stationary 6NM64 as function of the temperature difference between the monitors was obtained, for all 9 runs, as shown in Figure 9.2. This figure shows an amazingly large effect that cannot be ignored. The regression line indicates that the ratio changes with (0.13 ± 0.02) %/°C. Such a large temperature coefficient is a problem, because calibration data must be accurate to within 0.1 – 0.2% (Chapter 5). This experiment does not reveal what fraction of this effect is due to the 6NM64 or the calibrator. However, the temperature excursions of the 6NM64 in the monitor room was kept as constant as possible. Thus it is safe to ascribe the entire effect to the temperature excursions of the calibrator.

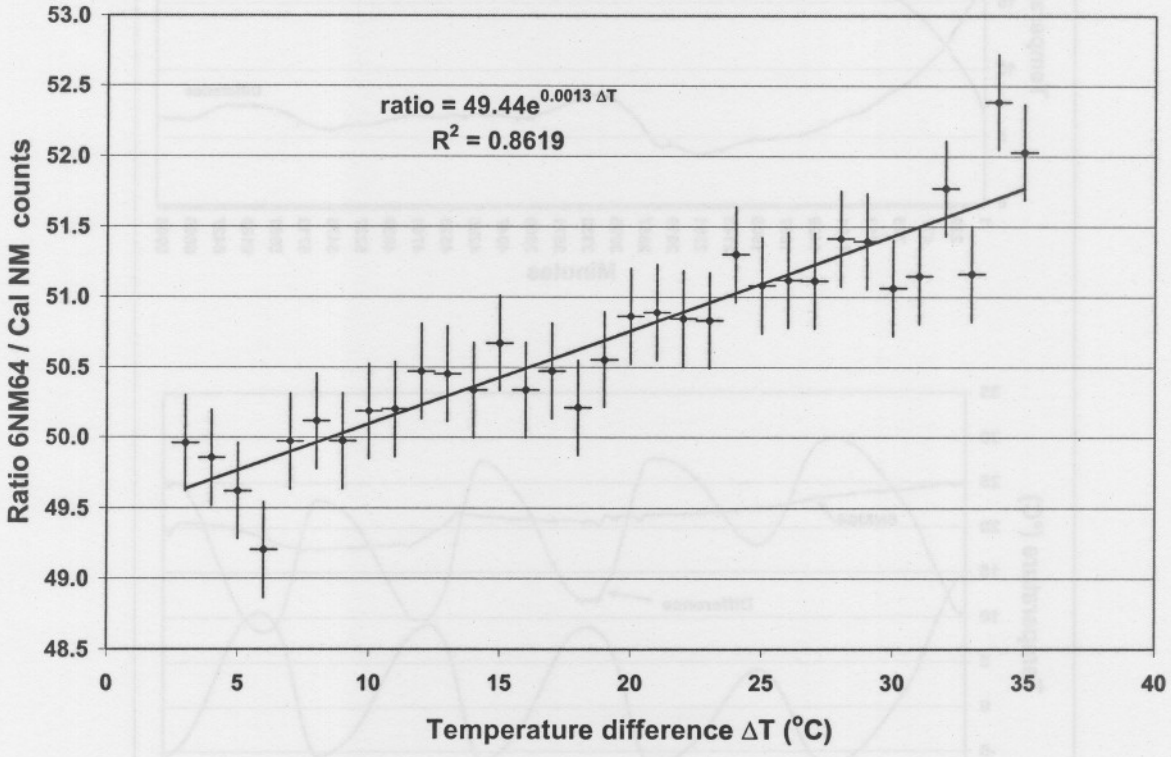

Figure 9.2: The ratio of the counts of the calibrator and stationary 6NM64 as function of the temperature difference between the 6NM64 and the calibrator, in °C.

For the most part, the temperature effect for neutron monitors has been neglected compared to the atmospheric pressure effect (see Chapter 8). It seems that not only pressure corrections have to be made to data measurements, but also temperature corrections, if the monitor is not kept at constant temperature.

As stated in Chapter 8, the atmospheric temperature effect is about – 0.03 %/°C at the poles (Iucci *et al.*, 2000). In the present experiment the atmospheric temperature has the same effect on both monitors, because they are close to each other with the same atmosphere above them. The conclusion is therefore that this must be an instrumental temperature effect, which is about four times larger than the atmospheric effect and in the opposite sense.

With this information, temperature corrections of 0.13 %/°C were made for every 1-minute ratio. The averages were then recalculated, in the same way as before (Table 9.2), and are shown in Table 9.3.

Table 9.3: Temperature corrected ratios

Position	Round 1	Round 2	Round 3	Average
1 (landing)	53.107 (-0.27%)	53.087 (-0.31%)	53.534 (+0.58%)	53.242
2 (high)	50.484 (+0.26%)	50.274 (-0.15%)	50.294 (-0.11%)	50.351
3 (outside)	49.554 (+0.28%)	49.223 (-0.38%)	49.468 (+0.10%)	49.415

When comparing the ratios of the counting rates in Table 9.3 of positions 2 and 3, it can be seen that the ratios outside the base at position 3 are now smaller than inside at position 2, for each round, in contrast with Table 9.2. This means that the calibrator counts more outside (denominator smaller) than inside, as it should be. From the averages (last column) of positions 2 and 3, it follows that about 1.9% of the intensity is absorbed by the roof.

Furthermore, when comparing Table 9.3 with Table 9.2, again only 2 of the 9 ratios lie inside the acceptable statistical limit of 0.14%. Therefore, the number of ratios inside this range does not necessarily decrease. Six of the 9 measurements have a deviation within ± 0.28%, which seems to be a more practical range.

This was, however, a new type of experiment, which was done for the first time and with no experience. It was therefore repeated in Potchefstroom in more detail.

9.3 Measurements in Potchefstroom

During 2003 to 2005, an extensive range of experiments was executed in Potchefstroom to test the calibration neutron monitor: (1) the stability part was described in Section 8.5.2. In this case much better statistics were achieved, with 6 out of 10 measurements within a range of ± 0.13%, in comparison with the 2 out of 9 obtained at Sanae; (2) the influence of environmental effects will be discussed in the following chapter; and (3) its temperature sensitivity will be described in the following section.

9.3.1 Temperature sensitivity of the calibrator

The purpose of the following experiment was to confirm the temperature coefficient obtained at Sanae.

The calibrator was placed in the so-called Sanae room, about 18 m from the IGY neutron monitor, on the same level. The electronics head faced towards the north, 1 m from the northern wall. The temperature of this room was varied gradually with an air-conditioner and

heaters, letting the calibrator's temperature to change over a range of 25 degrees, while the IGY was kept at a constant temperature in the monitor hut. The average room temperature of (23 ± 1)°C (see Figure 9.5) was accepted for the temperature of the IGY, because it does not have a built-in sensor like the calibrator.

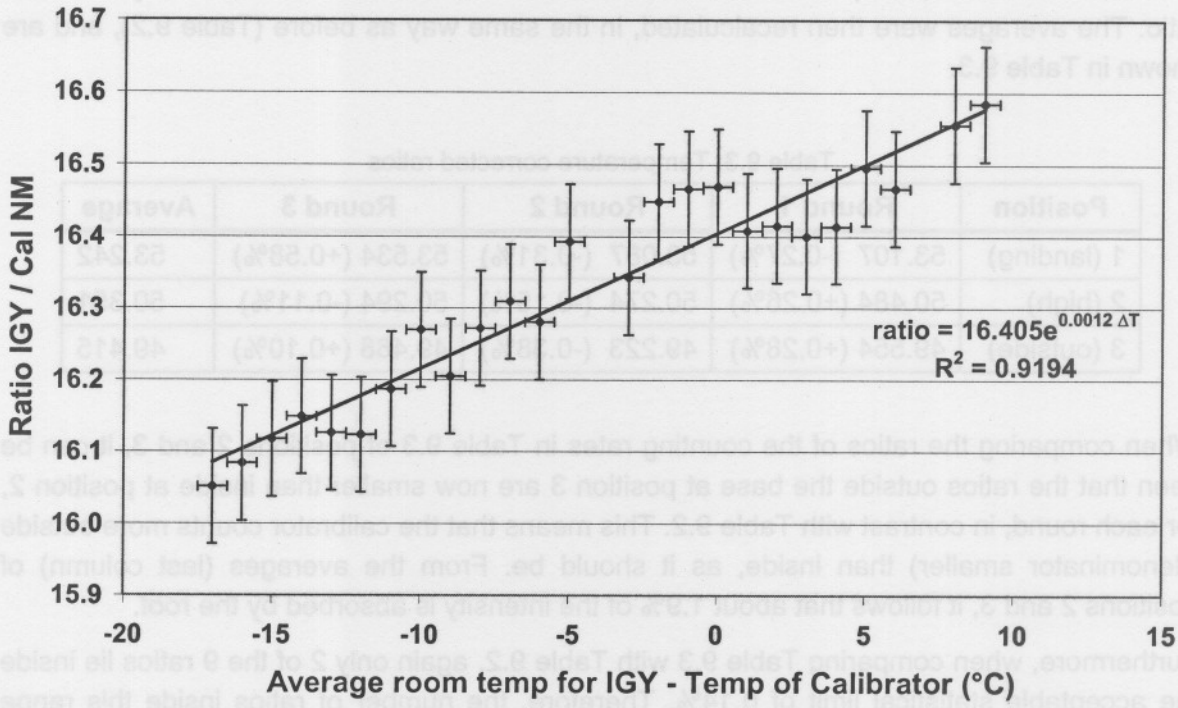

Figure 9.3: The temperature effect of the calibrator, obtained from day 289-322 of year 2003.

The ratios of the counting rates of the IGY to the calibrator as function of the difference in temperature between the two monitors are shown in Figure 9.3. The regression line gives a positive slope of (0.12 ± 0.01) %/°C. This agrees well with the value (0.13 ± 0.02) %/°C, determined by Moraal *et al.* (2003) at Sanae, as described in the previous section.

This experiment was repeated, with the calibrator in a small room on the same level as the Sanae room and the monitor hut, but closer to the monitor hut as the Sanae room. The centre of the calibration monitor was about 10 m west of the monitor hut. The electronics display faced north. The same coefficient of (0.12 ± 0.02) %/°C was found, as shown in Figure 9.4. Thus, these two experiments, together with the one at Sanae, demonstrate the reliability of the method.

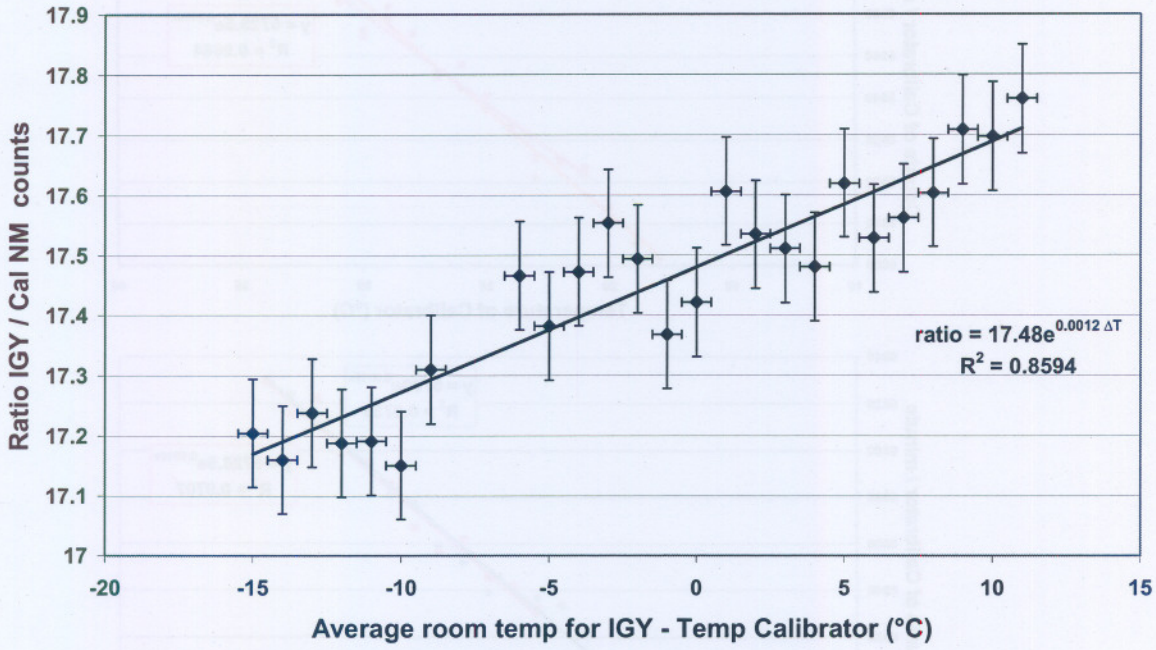

Figure 9.4: The temperature effect of the calibrator, obtained from day 162-180 in 2004.

The temperature of the calibrator and the average room temperature accepted for the IGY are shown in Figure 9.5. It can be clearly seen that the temperature used for the IGY was constant within ± 1°C, while that of the calibrator was varying. The 'spikes' seen in the room temperature is due to the air-conditioner.

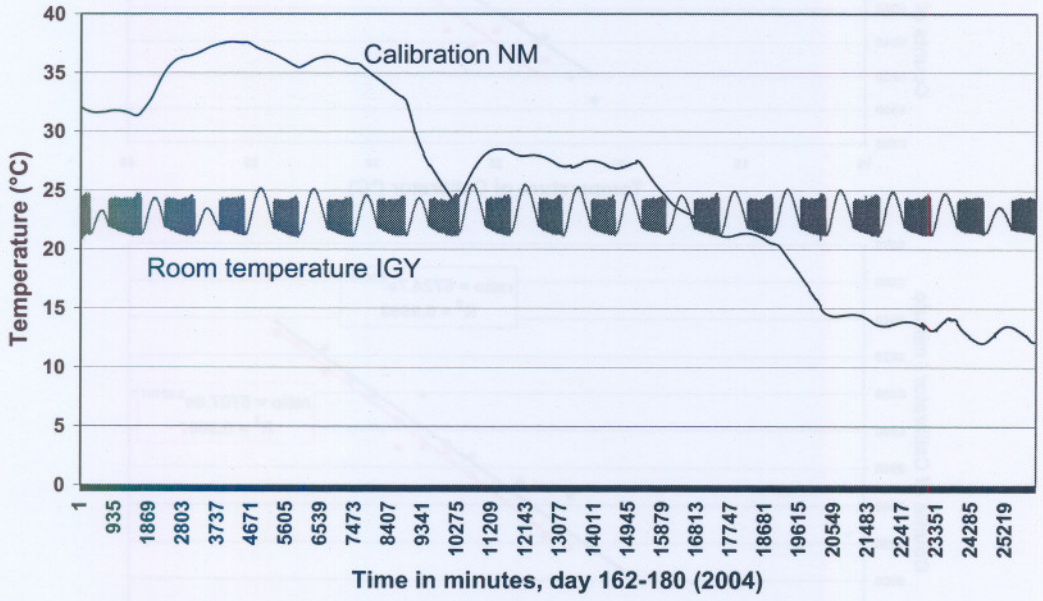

Figure 9.5: The temperature of the calibrator in comparison with the temperature used for the IGY, obtained from day 162-180 in 2004.

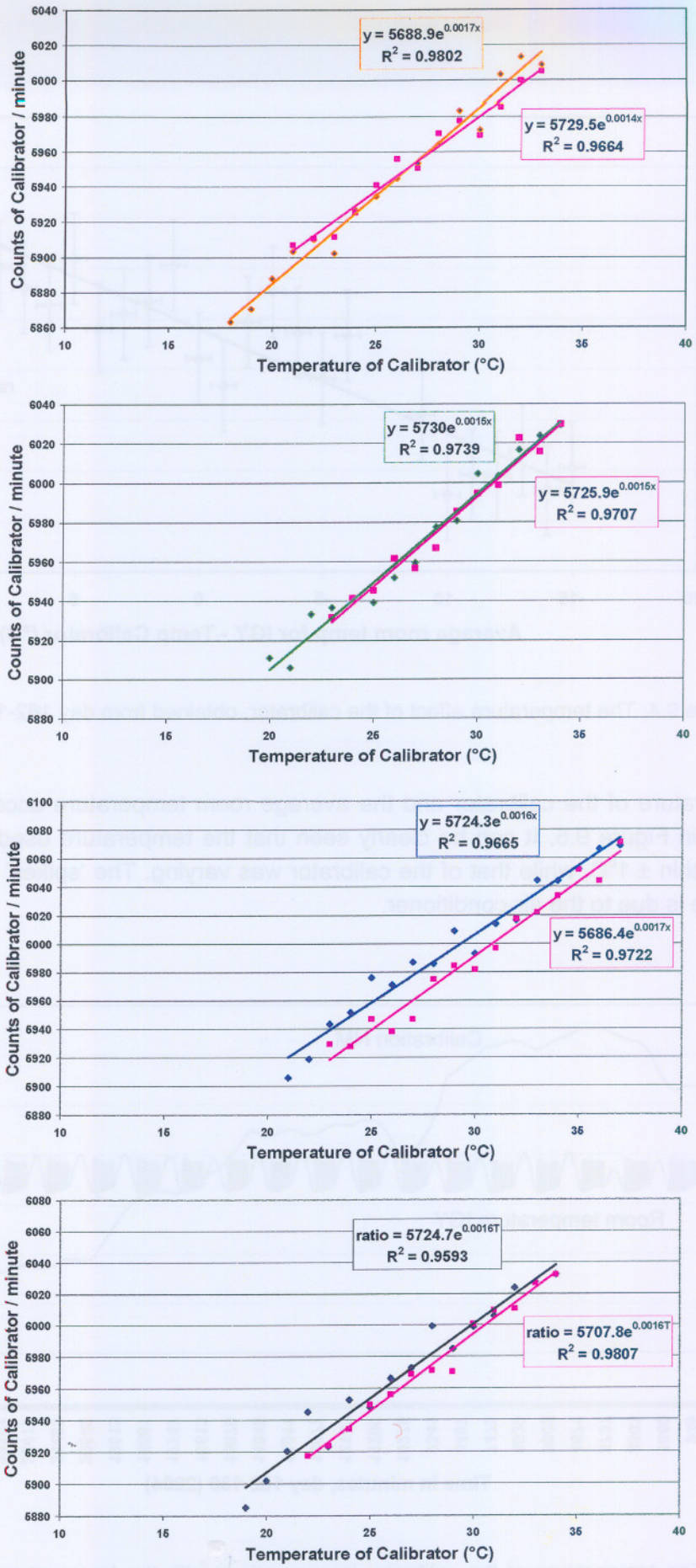

Figure 9.6: The temperature effects were determined for four spare pre-amplifiers. For each one, the temperature was increased (diamonds) and then decreased again (pink squares) in order to obtain two regression lines.

9.3.2 Temperature sensitivity of pre-amplifiers and of neutron source

Some inaccuracies were experienced with the data of the calibrator at the end of 2003. A problem with the pre-amplifier was suspected. In addition, the pre-amplifier may have been sensitive to temperature changes. For these reasons, the stability and temperature measurements were repeated with four new pre-amplifiers.

The temperature effect of the calibrator with every individual pre-amplifier was determined, with the calibrator in the smaller room west of the monitor hut. This time, a neutron source of 1 curie Americium-Beryllium was placed on the floor, ~0.20 m behind the calibrator, to speed up the experiment. The counting rate was ~40 times that of the background cosmic radiation. Approximately 600 000 counts were collected per individual measurement, and therefore atmospheric or primary intensity variation caused fluctuations << 0.1%.

The results are shown in Figure 9.6. For each run, the temperature was raised to ~35°C with the aid of heaters, and then dropped to room temperature again. These figures show that the temperature coefficients of the four pre-amplifiers are of the same order, namely (0.16 ± 0.02) %/°C, which is marginally larger than (0.12 ± 0.02) %/°C, obtained in the previous section. It seems as if this increase was not due to the pre-amplifiers, but rather due to the neutron source.

In the following experiment, the Am-Be neutron source was used to try to standardise the calibrator. This neutron source was placed in the middle on top of the calibrator to get the highest possible counting rate. To determine the influence of statistical or any other fluctuation defined in Chapter 8, the measured standard deviation / Poisson deviation, i.e. the K-value, was measured. As expected, a value of 1.00 was obtained, because no fluctuations should have any influence on this high counting rate of more than 20 000 counts / minute.
The temperature was then varied again, to test if there were any temperature effect. A large effect of (0.297 ± 0.006) %/°C was obtained, as shown in Figure 9.7. This is 2.5 times larger than the effect without the neutron source. The probable reason for this is that the energy spectrum of the source neutrons is much steeper than that of atmospherically produced ones.

The conclusion is that the slightly larger temperature coefficient measured with the four new pre-amplifiers was indeed due to the neutron source. Furthermore, when such a source is eventually used to monitor the absolute stability of the calibrator, this very large temperature effect must be carefully taken into account.

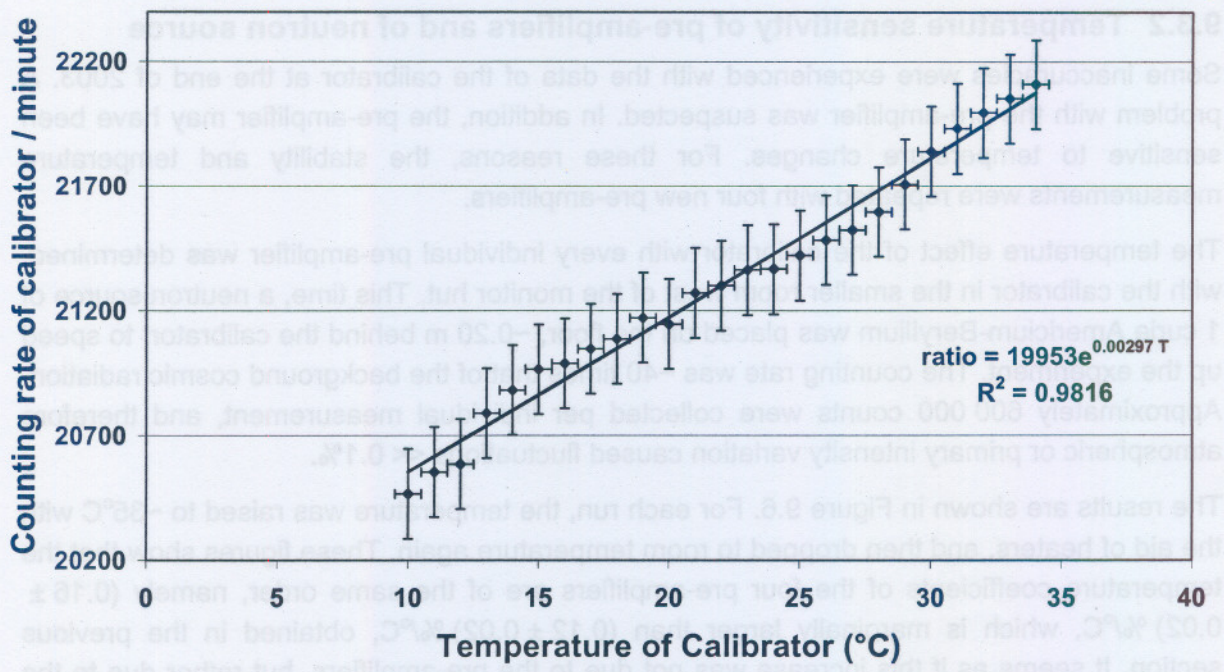

Figure 9.7: The temperature effect of the calibrator with a neutron source on top, obtained from day 156-159 in 2004.

9.3.3 Temperature sensitivity of the IGY

After the temperature sensitivity of the calibrator (with a ^{3}He counter) had been determined, the next step was to compare this with the sensitivity of stationary neutron monitors, namely the IGY (with $^{10}BF_3$ counters) and NM64 (with both types of counters).

The temperature coefficient of the Potchefstroom 15-tube IGY can be determined in two ways:

- One method is to keep the temperature of the calibrator constant, while the temperature of the IGY varies.
- Another method is to keep both monitors inside the monitor hut at different fixed temperatures for several days each. Because the temperature coefficient of the calibrator is known, that of the IGY can then easily be calculated.

The calibrator has a built-in temperature sensor, while the IGY does not. Therefore it was not easy to obtain the reliable temperatures of the IGY. For that reason it was decided to use the second method only.

The temperature coefficient of the IGY was obtained by placing the calibrator inside the monitor hut, just north of the IGY. The electronics head faced north. It was about 0.45 m above the centre of the IGY, because it stood on top of its cradle. The temperature of the hut was varied: first cooled down as cold as possible for several days, then the temperature was increased and kept at another fixed temperature for several days. This was done for four different fixed temperatures.

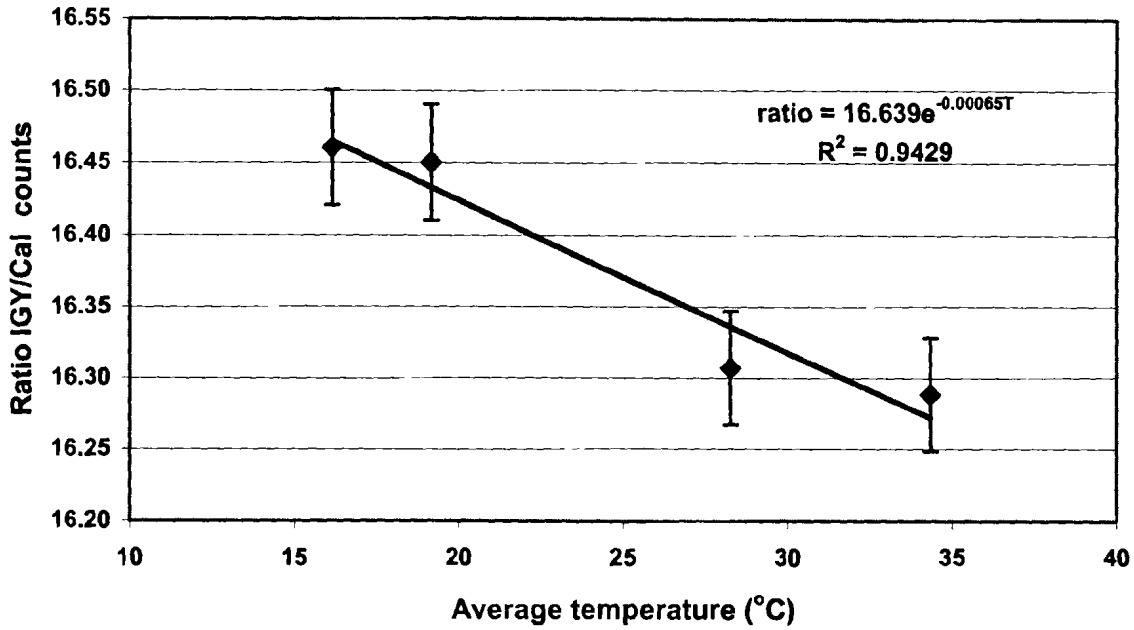

Figure 9.8: The temperature effect determined for the IGY, obtained from day 197-247 in 2004.

Figure 9.8 presents the ratios of the counts of the IGY and calibrator as function of temperature. The regression line gives a negative slope of – (0.065 ± 0.004) %/°C. Since the temperature coefficient of the calibrator is (0.12 ± 0.02) %/°C, that was used to calculate the coefficient of the IGY, as follows:

$$N_{cal} = N_{c0} e^{(0.0012 \pm 0.0002)\Delta T}$$

$$\frac{N_{IGY}}{N_{cal}} = \frac{N_{I0}}{N_{c0}} e^{-(0.00065 \pm 0.00004)\Delta T}$$

$$\Rightarrow N_{IGY} = N_{I0} e^{(0.0012 \pm 0.0002)\Delta T} e^{-(0.00065 \pm 0.00002)\Delta T}$$

$$\Rightarrow N_{IGY} = N_{I0} e^{(0.0006 \pm 0.0002)\Delta T}.$$

Thus, the temperature coefficient of the IGY is (0.06 ± 0.02) %/°C.

9.4 Temperature coefficients obtained at McMurdo

To determine the temperature coefficient of the other calibrator on the US / Australian 2004/05 sea-voyage to McMurdo, a proposal was made to the Bartol-group to switch off the air-conditioning for some time while the ship stayed around McMurdo. This was to be a repetition of the Potchefstroom IGY experiment, as described in Section 9.3, but for the other calibrator. As stated in Chapter 7, some failure occurred in this calibrator, and therefore no results were obtained.

9.5 Other temperature coefficients obtained

The Bartol-group of the University of Delaware, USA, operates six stations, which are part of the Spaceship Earth project (see Chapter 3). This neutron monitor network consists of a combination of $^{10}BF_3$ and ^3He counters. Evenson *et al.* (2005) described how they found it necessary to apply temperature corrections to their data, even before applying pressure corrections. Some of their results will be described here, first some simulations done by J.M. Clem, and thereafter experimental results.

9.5.1 Simulation of temperature effects

Clem (2004, private communication) simulated the temperature sensitivity of a 3NM64 neutron monitor, using the FLUKA simulation program. This simulation generates primary particles, obtained from the solar modulated spectrum, that propagate through the atmosphere. Sea-level particles are used as input to a second simulation, where the particles are propagated through a typical NM64 structure. This simulation was done for both the BP28 ($^{10}BF_3$) and LND ^3He counters.

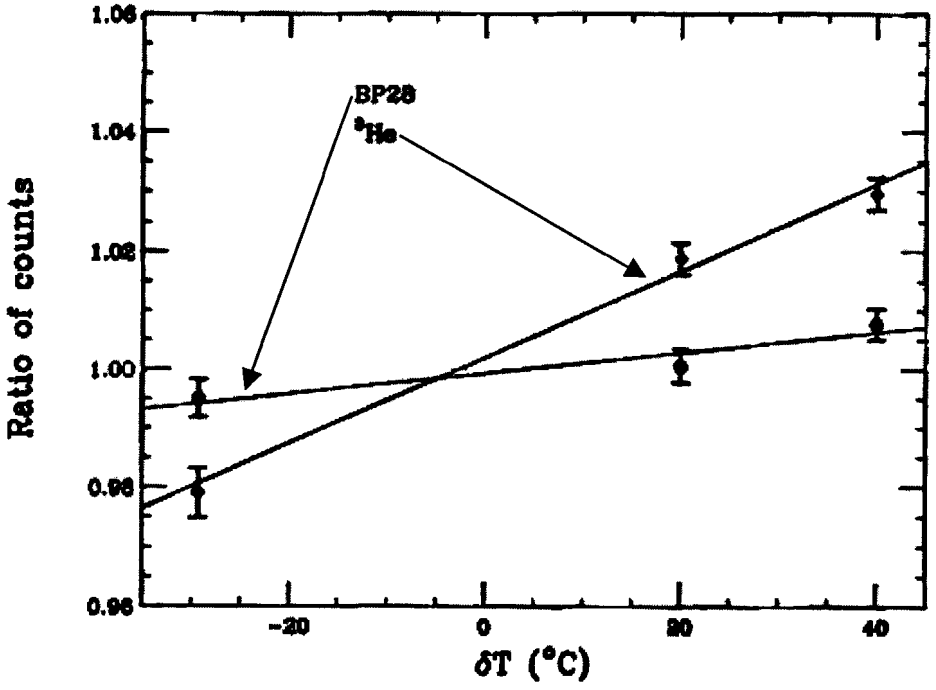

Figure 9.9: Calculated temperature effects on 3NM64 for BP28 ($^{10}BF_3$) and LND ^3He counters. From J.M. Clem (2004, private communication).

Figure 9.9 shows the ratio of neutron monitor counts as function of the temperature difference. The reference temperature is 20°C. Thus, a temperature of 60°C is shown as δT = 40°. The regression line for the ^3He counter indicates a temperature coefficient of (0.073 ± 0.007) %/°C, and that of the $^{10}BF_3$ is (0.0176 ± 0.0060) %/°C. This simulation therefore indicates that a ^3He neutron monitor is about four times more sensitive to temperature changes than a $^{10}BF_3$ neutron monitor.

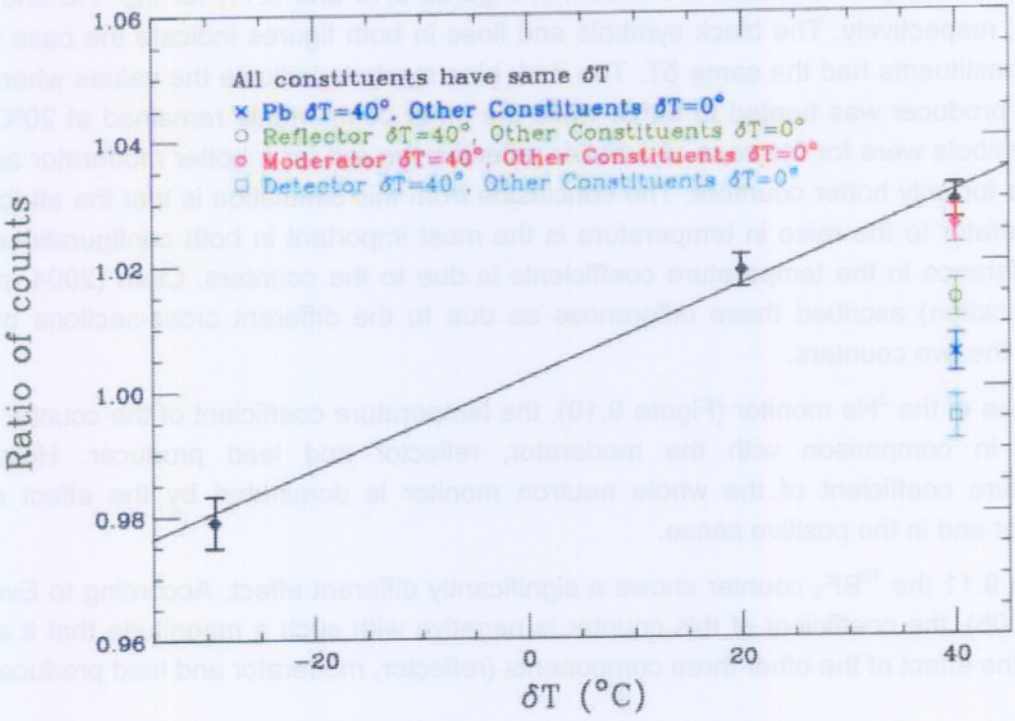

Figure 9.10: Calculated temperature effects on individual components of ^{3}He 3NM64. From J.M. Clem (2004, private communication).

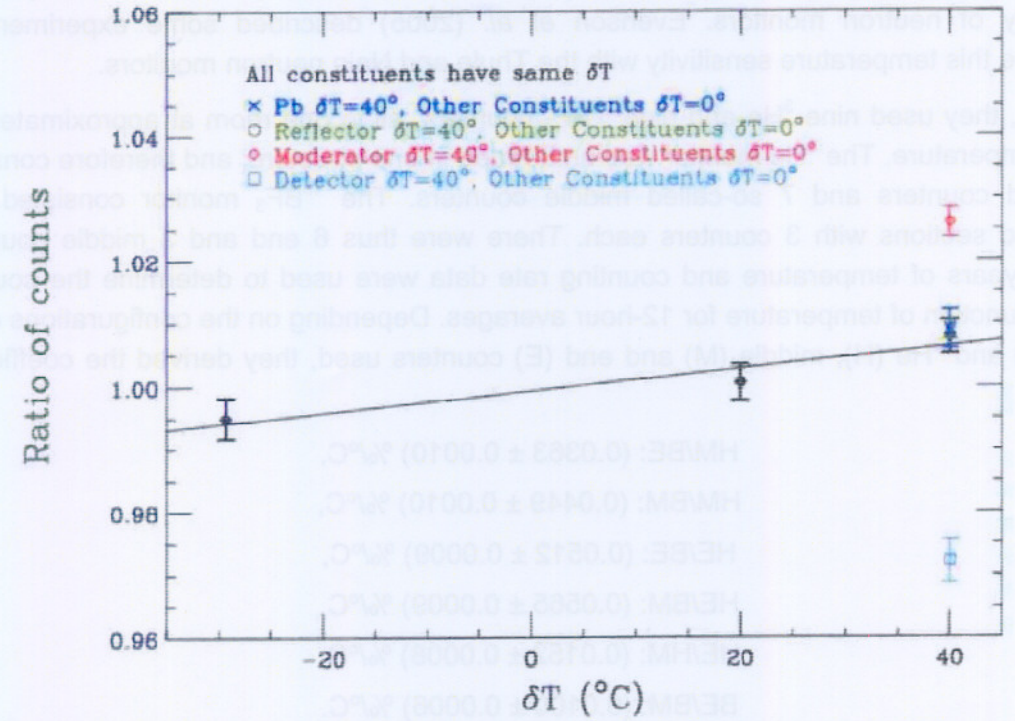

Fig 9.11: Calculated temperature effects on individual components of $^{10}BF_3$ 3NM64. From J.M. Clem (2004, private communication).

The reason for this large difference was found by heating the components of the neutron monitor separately. The results are shown in Figures 9.10 and 9.11, for the ^{3}He and $^{10}BF_3$ 3NM64s, respectively. The black symbols and lines in both figures indicate the case where all the constituents had the same δT. The dark blue symbols indicate the values where only the lead producer was heated to 60°C, while the other components remained at 20°C. The green symbols were for the case of a hotter reflector, the red for a hotter moderator and the light blue for only hotter counters. The conclusion from this simulation is that the attribute of the moderator to the raise in temperature is the most important in both configurations. The main difference in the temperature coefficients is due to the counters. Clem (2004, private communication) ascribed these differences as due to the different cross-sections of both gases in the two counters.

In the case of the ^{3}He monitor (Figure 9.10), the temperature coefficient of the counter is the smallest in comparison with the moderator, reflector and lead producer. Here, the temperature coefficient of the whole neutron monitor is dominated by the effect of the moderator and in the positive sense.

In Figure 9.11 the $^{10}BF_3$ counter shows a significantly different effect. According to Evenson *et al.* (2005), the coefficient of this counter is negative with such a magnitude that it almost cancels the effect of the other three components (reflector, moderator and lead producer).

9.5.2 Experimental temperature effects of the Bartol-group

As mentioned in the introduction, the Bartol Research Institute experienced some problems with runaway temperatures, which led to an independent investigation of the temperature sensitivity of neutron monitors. Evenson *et al.* (2005) described some experiments to determine this temperature sensitivity with the Thule and Nain neutron monitors.

At Thule, they used nine ^{3}He and nine $^{10}BF_3$ counters, all in one room at approximately the same temperature. The ^{3}He monitor was embedded in one structure, and therefore consisted of 2 end counters and 7 so-called middle counters. The $^{10}BF_3$ monitor consisted of 3 separated sections with 3 counters each. There were thus 6 end and 3 middle counters. Several years of temperature and counting rate data were used to determine the counting ratio as function of temperature for 12-hour averages. Depending on the configurations of the $^{10}BF_3$ (B) and ^{3}He (H), middle (M) and end (E) counters used, they derived the coefficients as:

HM/BE: (0.0363 ± 0.0010) %/°C,

HM/BM: (0.0449 ± 0.0010) %/°C,

HE/BE: (0.0512 ± 0.0009) %/°C,

HE/BM: (0.0565 ± 0.0009) %/°C,

HE/HM: (0.0152 ± 0.0008) %/°C,

BE/BM: (0.0100 ± 0.0006) %/°C.

Here the notation HM/BE, for instance, means the ratio from a ^{3}He counter in a **m**iddle position to a $^{10}BF_3$ counter at an **e**nd position. This experiment is similar to the IGY/calibrator experiment described in Section 9.3.3.

At Nain, six ^{3}He counters in two 3NM64 sections were placed in three independently heated shipping containers (vans). Each set contained four end and two middle counters. Each container was kept at a different fixed temperature for several weeks. This experiment is equivalent to the Sanae and the calibrator/IGY experiments, as described in Sections 9.2 and 9.3.1. The coefficients determined at Nain are:

Middle counters: (0.0839 ± 0.0028) %/°C and (0.0828 ± 0.0060) %/°C.

End counters: (0.0938 ± 0.0025) %/°C and (0.0959 ± 0.0054) %/°C.

The Nain experiment allowed the authors to calculate the ^{3}He coefficients. Using these in the Thule experiment allowed them to derive the $^{10}BF_3$ coefficients as well. The average temperature coefficients (averaged over middle or end counters) are (0.091 ± 0.002) %/°C for the ^{3}He counters and (0.044 ± 0.002) %/°C for the NM64 with $^{10}BF_3$ counters.

9.6 Summary and conclusion

In this chapter it was shown that the calibration neutron monitor has an unexpectedly large temperature sensitivity. Parallel to this discovery, the Bartol-group found a similar temperature effect for the NM64-type. Temperature coefficients were determined for the calibrator and the IGY monitor at Potchefstroom. A summary of the temperature coefficients obtained, is shown in Table 9.4, ranging from large to small.

Table 9.4: Temperature coefficients

^{3}He Calibrator:	0.12 ± 0.02 %/°C
^{3}He 3NM64 (Thule/Nain):	0.091 ± 0.002 %/°C
^{3}He 3NM64 (Simulation):	0.073 ± 0.007 %/°C
$^{10}BF_3$ IGY (Potchefstroom):	0.06 ± 0.02 %/°C
$^{10}BF_3$ 3NM64 (Thule):	0.044 ± 0.002 %/°C
$^{10}BF_3$ 3NM64 (Simulation):	0.018 ± 0.006 %/°C

The calibrator has the largest sensitivity, followed by the ^{3}He 3NM64, the IGY and the $^{10}BF_3$ 3NM64. According to the Clem simulations, the low coefficients obtained for the $^{10}BF_3$ NM64 are due to positive coefficients in the lead and polyethylene that are offset by a negative coefficient of the counter.

The coefficients of both the ^{3}He and BF_3 measurements are considerably larger than those of the simulations, and that is not understood. Evenson *et al.* (2005) planned to conduct more simulations, in order to see why coefficients obtained by simulation are significantly lower than the measured ones.

This experiment has demonstrated that the temperature effect is large with respect to the desired calibraton accuracy of 0.1 – 0.2% and has to be taken into account. This means that all neutron monitors have to be kept at a fixed temperature or that the counting rates have to be normalised to a standard temperature. This effect will be included in the planned calibration technique for neutron monitors.

Chapter 10
The Environmental Sensitivity of the Calibrator

10.1 Introduction

The stability of neutron monitors depends on several factors, such as changing of the absorbing material around the monitor and variations in the environmental background. Hatton (1971), for instance, described the effect of snow on the counting rate of a monitor. The accumulation of snow on the ground surrounding the high latitude Deep River Canadian monitor station caused a decrease in the counting rate, due to the moderation of the neutrons produced in the ground surrounding the monitor. For such reasons, the sensitivity of the calibrator to different ground surfaces was investigated and is described in this chapter.

In principle, such effects can be avoided with a sufficiently thick reflector. As the name suggests, it will reflect the neutrons produced inside the neutron monitor back towards the counters, but those produced outside the monitor away from them. To introduce the subject, some classical calculations about the reflector performance of Hatton and Carmichael (1964) are presented.

10.2 Experiments with the thickness of the reflector

Hatton and Carmichael (1964) conducted experiments with different thicknesses of the reflector, using a 2NM64, to investigate the effect of environmental neutrons.

The thickness of the reflector of a standard NM64 is 7.5 cm of polyethylene, in comparison with 30.5 cm of paraffin wax for an IGY. According to Hatton and Carmichael (1964), the main reason for using this smaller thickness of polyethylene for the standard NM64 is due to its relatively high cost. They showed experimentally that a thickness of 7.5 cm (3 inches) of polyethylene is adequate, by determining the variation of the counting rate with thickness of the reflector. They kept the polyethylene underneath the monitor at a constant thickness of 6 inches (15 cm), while the thickness of the polyethylene on the sides and the top was increased from 0 to 15 inches (38 cm).

Firstly, they executed an experiment with the inner moderator around the counters and then without it. Figure 10.1 shows the variation of the counting rate as function of reflector thickness, for the complete monitor with the inner moderator. It shows that the counting rate is a maximum when the reflector thickness is about 2 inches (5 cm). The increase in counting rate between 0 and 2 inches is due to the increased thermalisation of neutrons produced in the lead. Beyond 3 inches the decrease is due to increasing absorption of the evaporation neutrons, produced both in the lead and outside the monitor.

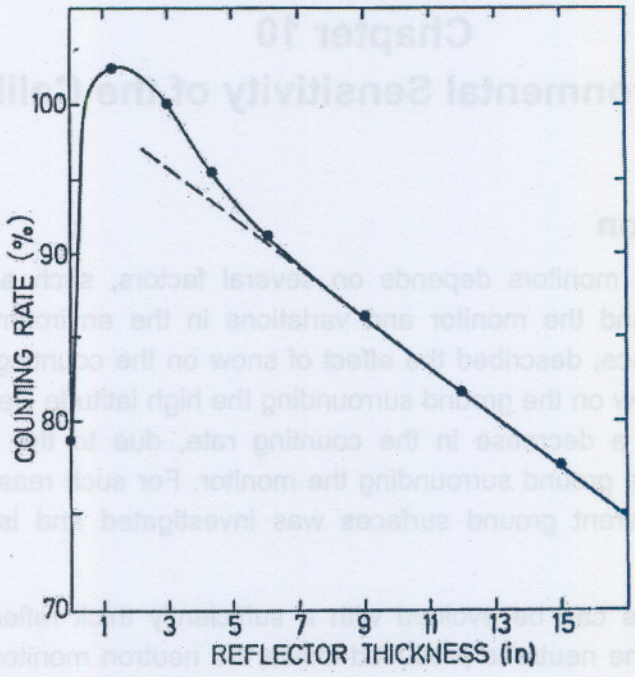

Figure 10.1: The variation of the counting rate of a 2NM64 with change of thickness of the reflector. Adapted from Hatton (1971).

The decrease of the counting rate with reflector thickness > 9 inches (22 cm) is only due to absorption of the nucleonic component of secondary cosmic rays, i.e. all the evaporation neutrons from the environment are absorbed. This decreasing component was extended to 3 inches (7.6 cm) with the dashed line. Thus, with a thickness of 3 inches, ~5% of the counting rate is due to neutrons produced in the environment.

For the sake of completeness, a related experiment is also described, where the authors determined the variation of the counting rate of this 2NM64 monitor without the lead producers as the thickness of the reflector was varied, as shown in Figure 10.2. The counting rate is expressed as a percentage of the rate of a normal neutron monitor with the lead producer and a reflector of 3 inches (7.6 cm) thick. The continuous line gives the variation of the experimental counting rate of the 2NM64 without the lead producer as a function of the thickness of the reflector. This figure shows that the counting rate decreases rapidly with increasing reflector thickness, from about 1 inch (2.5 cm) to about 6 inches (15 cm). Thereafter the rate decreases more slowly.

The flat dashed line in Figure 10.2 shows the relative counting rate due to evaporation neutrons from within, caused by primary cosmic rays. The authors obtained this curve by using the interpolated line of Figure 10.1. The steep dashed curve indicates the relative counting rates due to environmental neutrons from outside the monitor. This curve was obtained by subtracting the values of the flat dashed line from those of the continuous line.

Thus, in a normal monitor with a reflector of 3 inches (7.6 cm) thick, about 7% of the counting rate is produced by evaporation neutrons produced in the polyethylene and in the counters.

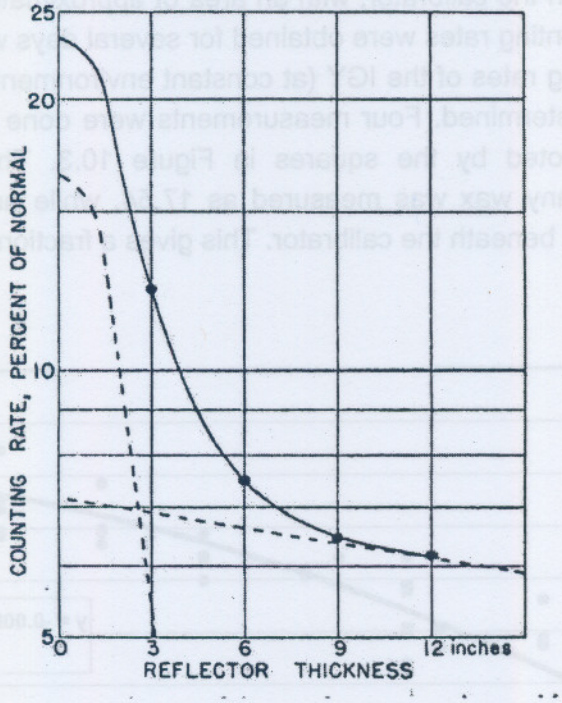

Figure 10.2: The variation of the counting rate of the same 2NM64 used in Figure 10.1 with no lead producer inside with change of thickness of the reflector. Adapted from Hatton and Carmichael (1964).

The final conclusion of Hatton and Carmichael (1964) about the thickness of the reflector and the effect of evaporation neutrons produced in the vicinity of the monitor is that 3 inches (7.6 cm) of polyethylene does not fully attenuate the fast evaporation neutrons. Therefore, changing of the environment close to the monitor should be avoided, such as moving heavy apparatus around. They found, however, that about 4000 pounds (1800 kg) of lead at a distance of about 10 inches (25 cm) increased the counting rate by approximately 4%, and their conclusion is that the effect of most movable pieces of equipment can probably be neglected.

10.3 Experimental observations

In order to achieve calibration accuracies of 0.1 – 0.2%, the environmental factors must be known to within this limit. The calibrator has a 7.8 cm (3 inches) reflector. According to Figure 10.1, it may therefore be subject to neutrons produced outside the neutron monitor to the level of ≈ 2 – 4%. Krüger and Moraal (2005) stated that, in general, the effects of the roof and walls can be avoided by placing the calibrator in the open. The limiting factor then seems to be its sensitivity to different ground surfaces. These surfaces will have different effects due to their different neutron production and moderation characteristics. If this production differs significantly from one type of ground surface (soil, concrete, wood, etc.) to the next, it can easily cause changes in counting rate outside the required uncertainty of 0.1 – 0.2%. Therefore, this sensitivity of the calibrator to different ground surfaces was investigated.

Initially, the calibrator on its cradle was kept in the small room on the same level as the IGY in the monitor hut, as described in Chapter 9. For the first experiment, large blocks of paraffin

wax were placed beneath the calibrator, with an area of approximately 2.5 m^2. The height of the wax was 15 cm. Counting rates were obtained for several days with and without the wax. The ratios of the counting rates of the IGY (at constant environmental conditions) and those of the calibrator were determined. Four measurements were done with 15 cm of wax, and eight without wax, denoted by the squares in Figure 10.3. The average temperature corrected ratio without any wax was measured as 17.54, while an average of 17.84 was obtained with 15 cm wax beneath the calibrator. This gives a fractional difference of 1.7% per 15 cm of wax.

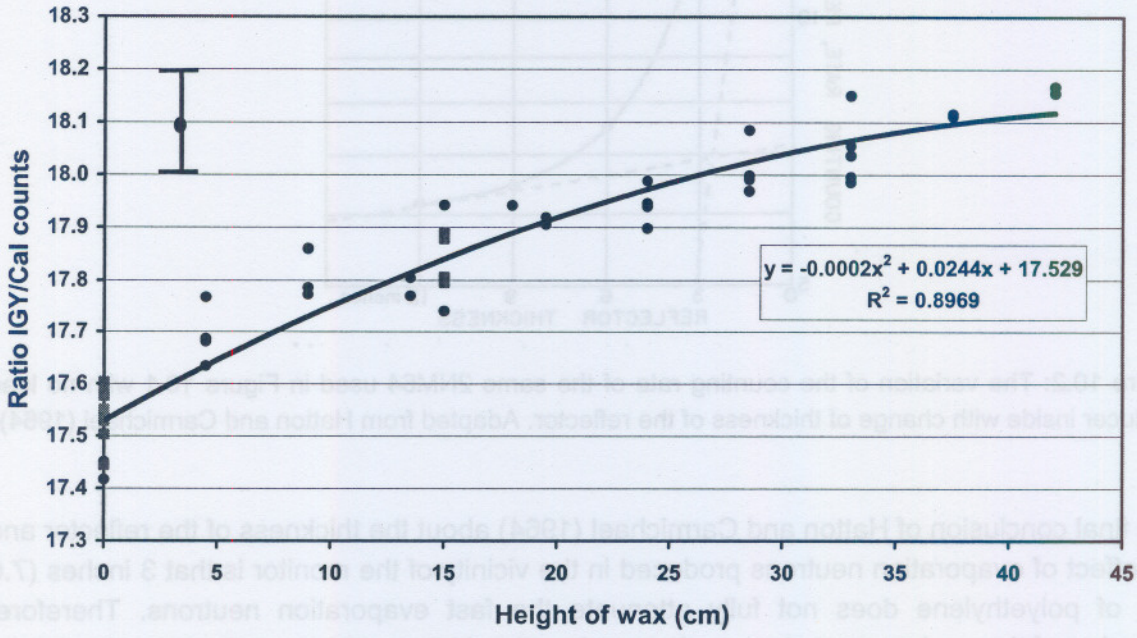

Figure 10.3: The ratio of the counting rates of the IGY and calibration neutron monitor as function of the height of the wax underneath the calibration neutron monitor. The squares indicate the ratios of the initial arrangement of wax, while the dots indicate those of the second experiment.

To investigate this quite large effect further, more and thinner blocks of wax were used. The experiment was repeated in a somewhat different layout than before. The cradle with the calibrator was lifted 27 cm above the surface, with two bricks below each wheel. In doing this, the bottom of the reflector cylinder of the calibrator was positioned about 77 cm above the surface. An area of approximately 3.0 m^2 beneath it was filled up in steps of 5 cm with wax layers. While the stationary IGY was kept at constant environmental conditions, the counting rates of the calibrator could be compared with those of the IGY.

The dots in Figure 10.3 represent the measurements of the second experiment. It can be seen that the counts of the calibrator decrease with increasing amount of layers. When fitting a regression line, it seems as if the curve will eventually flatten off at a height of > 40 cm. The average of the calibration counts recorded for each individual measurement is about 40 000 per data point, which gives a statistical error of ± 0.5%, denoted in the top left corner of the figure.

The difference is about 3.6% between the counting ratios with a wax height of about 40 cm and without wax. Due to this fairly large difference, the experiment was repeated yet another time with the calibrator in a totally different environment, while the IGY remained at constant environmental conditions. This time the sensitivity to different ground surfaces was also investigated.

The calibrator was placed in a garage on ground level, with a cement floor. Again, it was positioned about 77 cm above floor level. An area of approximately 3.0 m^2 beneath it was filled up in steps with the blocks of wax, then with water and finally with bricks. One million counts were recorded for every individual measurement, giving a Poisson accuracy of 0.1%. All calibration counts were temperature corrected. Figure 10.5 shows the calibrator with wax layers underneath it, and also with the portable plastic pool that was used for the water measurements.

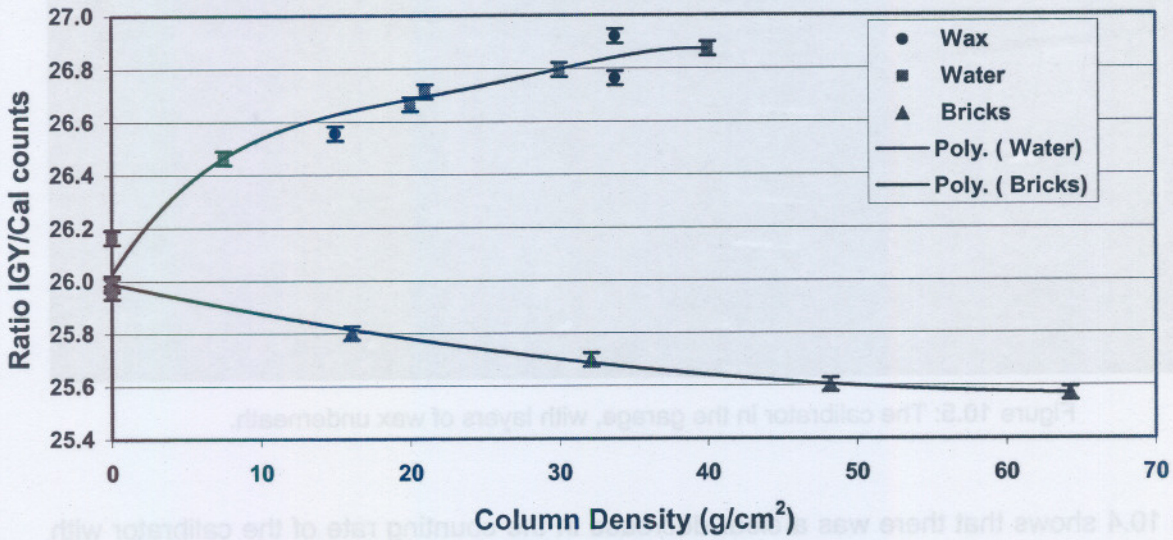

Figure 10.4: The ratio of the counting rates of the IGY and calibration neutron monitor as function of layers of wax, water and layers of bricks underneath the calibration neutron monitor. The dots indicate the ratios for the wax layers, the squares for the water depth, while the triangles indicate the different layers of bricks. Adapted from Krüger and Moraal (2005).

Figure 10.4 shows the ratio of the counting rates (IGY/calibrator) as function of column density of material underneath the calibrator. The dots represent the ratios for the wax layers. The two values at 34 g/cm^2 were obtained in two consecutive weeks, where the first week's data measurements were used for the one data point, and the second week's for the other one.

The square symbols in Figure 10.4 indicate the ratios obtained for different water depths, while the triangles show the variation of the ratios with different layers of bricks underneath the calibrator. The curve through the water/wax points is a fourth order polynomial fit, while the regression line for the bricks is a second order one. The density of the bricks was calculated as 2.2 g/cm^3, and the thickness of each brick is 7.3 cm. The wax has a density of 0.75 g/cm^3.

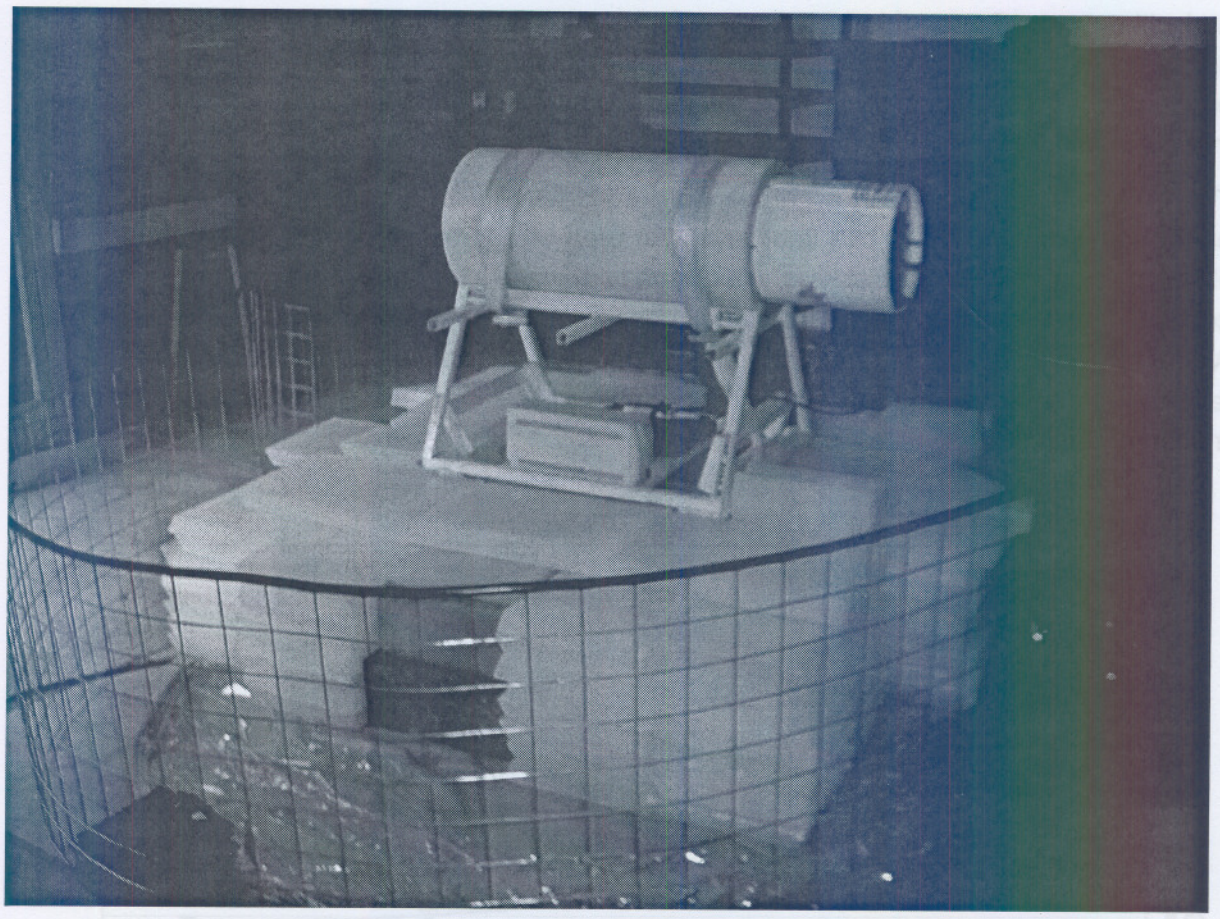

Figure 10.5: The calibrator in the garage, with layers of wax underneath.

Figure 10.4 shows that there was a clear decrease in the counting rate of the calibrator with increase in the amount of water and wax layers beneath the calibrator, up to about 3% per 40 g/cm^2. This effect seems to flatten off at about 40 g/cm^2. However, the opposite was observed for the brick surface: the counting rate of the calibrator increases with increasing layers of bricks.

The experiment was repeated once more with a deeper level of water to see what happens with the flattening beyond 40 g/cm^2. A maximum depth of nearly 76 cm was obtained. The ratio was expected to flatten off at about 26.8 – 26.9 in Figure 10.4, but it surprisingly increased with another 2 – 3% to 27.5, as shown in Figure 10.6. The reason for this sharp decrease of the counts of the calibrator for depths from ~60 – 80 g/cm^2 is unknown, but the decrease of the distance between the calibrator and the water surface is a probable cause. Since Hatton and Carmichael (1964) estimated that 9 inches of polyethylene, i.e. equivalent to 17 cm of water, should absorb virtually all the evaporation neutrons produced in the environment (see Section 10.2), this cannot explain the effect. It must therefore be concluded that this surface effect was not measured sufficiently accurate and must be repeated.

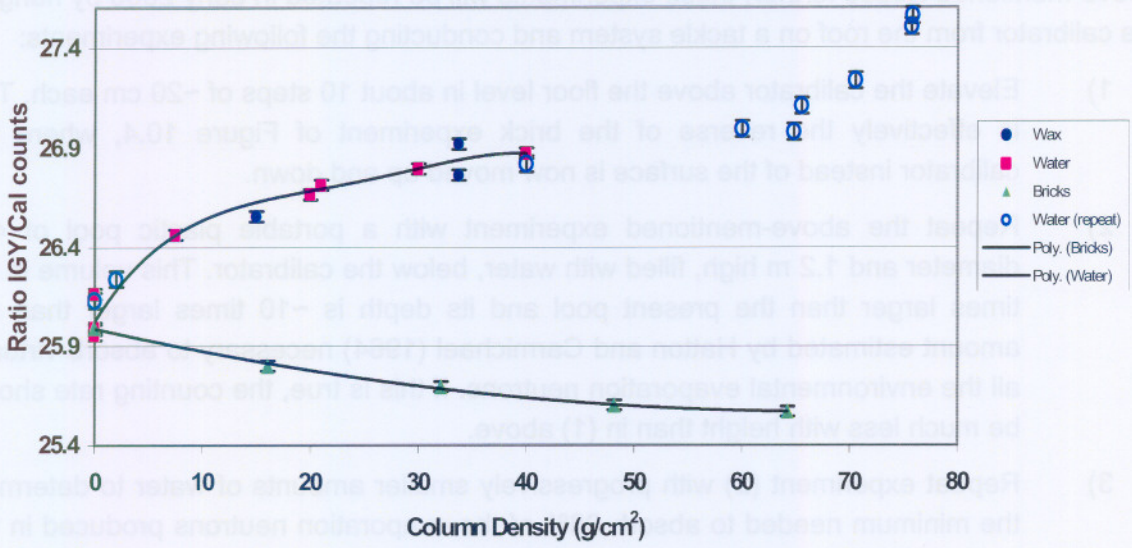

Figure 10.6: The same as Figure 10.4, except for additional water measurements, indicated by the blue open circles.

10.4 Conclusion

These experiments show that the calibrator has a very large sensitivity to the ground surface in terms of the desired 0.14% statistical accuracy.

Paraffin wax has a clearly defined polymer structure. This CH_2-polymer comprises mainly of straight chain hydrocarbons with 80 – 90% normal paraffin content and a small amount of branched paraffin (iso-paraffin) and cycloparaffin.

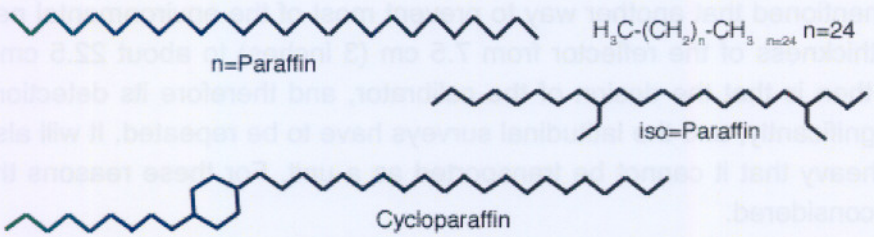

Although water does not have this polymer structure, the molecular structure and molecular mass is very similar to that of wax. The results from Figure 10.4 confirm that the molecular structures of water and wax are so similar that their neutron absorbing properties are almost identical.

The increase in the counting rate of the calibrator with the addition of layers of brick indicates that this higher atomic number material is an effective neutron producer with quite different properties than the absorbers such as water and wax.

The present results, as represented in Figure 10.6, are inconclusive. In order to address the above-mentioned issues further, these experiments will be repeated in early 2006 by hanging the calibrator from the roof on a tackle system and conducting the following experiments:

1) Elevate the calibrator above the floor level in about 10 steps of ~20 cm each. This is effectively the reverse of the brick experiment of Figure 10.4, where the calibrator instead of the surface is now moved up and down.

2) Repeat the above-mentioned experiment with a portable plastic pool of 4 m diameter and 1.2 m high, filled with water, below the calibrator. This volume is 3.5 times larger than the present pool and its depth is ~10 times larger than the amount estimated by Hatton and Carmichael (1964) necessary to absorb virtually all the environmental evaporation neutrons. If this is true, the counting rate should be much less with height than in (1) above.

3) Repeat experiment (2) with progressively smaller amounts of water to determine the minimum needed to absorb 98% of the evaporation neutrons produced in the ground (if the contribution of the evaporation neutrons is 5%, and if 2% of these remain, then the contribution to the counting rate is 0.05 x 0.02 = 0.1%).

4) Confirm the results of (3) with a different surface type, such as a large amount of bricks on the cement floor, and then repeating (3).

5) Use the optimal height of water determined in (3) and varies the water temperature, in order to determine if the temperature plays any role in the absorption of the evaporation neutrons.

The purpose is to try to determine the level, preferably of water, for which the calibrator becomes independent of the different ground surfaces below the water. If that can be achieved, the calibrations should be done by placing the calibrator at a specified distance above that thickness of water (or wax).

It should be mentioned that another way to prevent most of the environmental neutrons is to increase the thickness of the reflector from 7.5 cm (3 inches) to about 22.5 cm (9 inches). The problem then is that the design of the calibrator, and therefore its detection efficiency, will change significantly, and the latitudinal surveys have to be repeated. It will also make the calibrator so heavy that it cannot be transported as a unit. For these reasons this option is not presently considered.

Chapter 11
Conclusions and Recommendations for Calibration

To calibrate the worldwide network of stationary neutron monitors, in order to derive energy spectra from their counting rates, two calibrators were built and tested in Potchefstroom. The properties of these calibrators, viz. their (1) energy response as measured by their latitudinal or cutoff rigidity dependence, (2) statistical accuracy and reliability, (3) temperature sensitivity, and (4) sensitivity to ground/surface effects, were investigated to determine whether an overall accuracy of < 0.2% can be obtained, which is the maximum that can be tolerated for useful spectra. The results of these experiments are summarised as follows:

1. The calibrator has a difference of almost 4% in its energy response over the cutoff rigidity range from 0 – 16 GV in comparison to a standard 3NM64 neutron monitor. However, another survey is recommended, in order to achieve better statistical accuracy. When this is achieved, it will effectively establish the differential response function of the calibrator at sea level, similar to the procedure described with Figure 7.2.

   Simulations of this energy response done by J.M. Clem are so far inconclusive, because the two sets of calculations differ significantly from each other. The set that was supposed to correspond closest with the measured energy response deviates significantly from it, as shown in Figure 7.18. Therefore, improved simulations by Clem are still awaited.

2. Effects such as atmospheric pressure variations, diurnal variations, and short-term scintillations seem to increase the random fluctuations of the counting rate of a neutron monitor. These effects should be eliminated as far as possible in a calibration process. Multiplicity is another effect that has to be taken into account. Due to these effects, it was found that the coefficient of variation for 10^6 counts is approximately 0.14%, instead of the Poisson deviation of 0.10%.

   When the stability of the calibrator was tested by doing several repeated calibrations with 10^6 counts each, it was found that almost ⅔ of the results fall inside the effective fluctuation of ≈ 0.14%. This means that 10^6 counts will give optimal calibration accuracy. This implies that it will take ≈ 12 and ≈ 20 days at high and equatorial latitudes, respectively, to complete one calibration at sea level.

3. It was determined that not only the calibrator, but also the NM64 and IGY monitors, have fairly large instrumental temperature sensitivity, with that of the calibrator the largest, namely (0.12 ± 0.02) %/°C. These temperature effects must be taken into account and be corrected for, and/or neutron monitors have to be kept as near as possible at a fixed temperature during the calibration.

4. The calibrator has a very large sensitivity to the type of surface beneath it. When the surface beneath the calibrator is varied with different amounts of water and wax, its counting rate decreases by as much as 5%, while with bricks it increases up to nearly 2%. The present results are inconclusive and therefore a more detailed

investigation of this surface sensitivity is recommended, such as to (1) elevate the calibrator above the floor level in several steps, (2) use a four times larger portable plastic pool filled with water beneath the calibrator to repeat the first experiment, (3) repeat the second experiment with progressively smaller amounts of water in the pool, in order to determine the optimum amount, (4) confirm these results with a different surface type, such as bricks, and (5) determine whether the temperature of the water in the pool has a significant effect.

The purpose of these experiments is to determine the amount of water necessary for which only an insignificant number (< 2%) of environmental evaporation neutrons will contribute to the counting rate of the calibrator, irrespective of the type of ground surface. At present it seems that this sensitivity to different surface types may be the greatest challenge for the intercalibration of the neutron monitor network.

It is estimated that about 40 experiments of ~6 days each will be needed to perform these tests. This means that the calibrator will only be ready for calibration towards the end of 2006.

To start with the calibration, it is proposed to calibrate our own monitors first, viz. at Potchefstroom (P_c = 6.9 GV), Sanae (P_c = 0.8 GV), Hermanus (P_c = 4.5 GV), and Tsumeb (P_c = 9.1 GV). Thereafter, arrangements have to be made to send the calibrator to neutron monitors, such as Oulu, Finland (P_c = 0.8 GV), Kiel, Germany (P_c = 2.4 GV), Athens, Greece (P_c = 8.6 GV), Izmiran, Moscow, Russia (P_c = 2.3 GV), and Lomnicky Stit, Slovakia (P_c = 3.9 GV), whose principal investigators have expressed an interest in this (the cutoff rigidity values were calculated by Shea and Smart, 2001).

One of the neutron monitors in the Canadian network operated by the Bartol Research Institude should also be calibrated. The monitors in the polar regions are effectively self-calibrated, because the geomagnetic cutoff rigidities are less than the atmospheric cutoff. Thus, two neutron monitors at the same atmospheric depth measure the same spectrum of secondary cosmic rays. A second calibration or the Oulu calibration mentioned above can be considered as a check. A third experiment at high latitudes to test the atmospheric absorption as function of high altitudes at Sanae and South Pole is also considered.

The calibration process should consist of the following steps. First, if possible, the calibrator should stand inside the monitor hut, next to the neutron monitor. During this phase, stability and repeatability tests should be done. Thereafter, the calibrator will be moved outside, positioned above the portable plastic pool filled up to a certain height with water, for several days, to obtain ~10^6 counts. To calibrate a stationary neutron monitor, a normalisation factor of the counting rate will then be determined for each one, to obtain an equivalent counting rate with regard to the calibrator at that cutoff rigidity.

When calibrations of several of the worldwide stationary neutron monitors have thus be done accurately, the calibrated neutron monitors can be used to derive intensity spectra and differential response functions from their counting rates. This will then provide experimental data to study the modulation process in greater detail at high rigidities above 1 GV.

BIBLIOGRAPHY

Allkofer, O.C., Andresen, R.D., Bagge, E., Dau, W.D., and Funk, H., Cosmic rays latitude survey at solar minimum, *Tellus, 21*, 443-446, 1969.

Bachelet, F., Balata, P., Dyring, E., and Iucci, N., On the multiplicity effect in a standard cosmic ray neutron monitor, *Il Nuovo Cimento, 31*, no 5, 1126-1130, 1964.

Bachelet, F., Iucci, N., Villoresi, G., and Sporre, B., The cosmic ray spectral modulation above 2 GV during the descending phase of solar cycle number 19. I: A comprehensive treatment of the neutron monitor data from the worldwide station network and latitude surveys, *Il Nuovo Cimento, 7B*, no 1, 17-33, 1972.

Bieber, J.W., Clem, J., Duldig, M.L., Evenson, P., Humble, J.E., and Pyle, R., A continuing yearly neutron monitor latitude survey: Preliminary results from 1994-2001, *Proc. 27th Int. Cosmic Ray Conf., Hamburg*, 4087-4090, 2001a.

Bieber, J.W., Clem, J., Duldig, M.L., Evenson, P., Humble, J.E., and Pyle, R., Cosmic ray spectra and the solar magnetic polarity: Preliminary results from 1994-2002, *Solar wind ten: Proceedings of the Tenth International Solar Wind Conference. AIP Conference Proceedings, 679*, 628-631, 2003.

Bieber, J.W., Clem, J., and Evenson, P., Efficient computation of apparent cutoffs, *Proc. 25th Int. Cosmic Ray Conf., Durban,* 389-392, 1997.

Bieber, J.W., Clem, J., Evenson, P., Duldig, M.L., Humble, J.E., and Pyle, R., New method of observing neutron monitor multiplicities, *Proc. 27th Int. Cosmic Ray Conf., Hamburg,* 4091-4094, 2001b.

Bieber, J.W., Clem, J., Evenson, P., Pyle, R., Ruffolo, D., and Sáiz, A., Relativistic solar neutrons and protons on 28 October 2003, *Geophysical Research Letters, 32*, L03S02, 2005.

Bieber, J.W., Dröge, W., Evenson, P.A., Pyle, R., Ruffolo, D., Pinsook, U.,Tooprakai, P., Rujiwarodom, M., Khumlumlert, T., and Krucker, S., Energetic particle observations during the 2000 July 14 solar event, *The Astrophysical Journal, 567*, 622-634, 2002.

Bieber, J.W., Eroshenko, E., Evenson, P., Flückiger, and E.O., Kallenbach, R., Cosmic rays and earth, Kluwer Academic Publishers, 2000.

Bieber, J.W., and Evenson, P., Spaceship earth – an optimised network of neutron monitors, *Proc. 24th Int. Cosmic Ray Conf., Romey, 4*, 1316-1319, 1995.

Bieber, J.W., Evenson, P.A., Dröge, W., Pyle, R., Ruffolo, D., Rujiwarodom, M., Tooprakai, P., and Khumlumlert, T., Spaceship earth observations of the easter 2001 solar particle event, *The Astrophysical Journal, 601*, L103-L106, 2004.

Biehl, A.T., and Neher, H.V., The latitude and longitude effects in cosmic rays over the United States and Canada at 30 000 feet, *Physical Revue, Letters to the Editor, 78*, 172-173, 1950.

Biehl, A.T., Neher, H.V., and Roesch, W.C., Cosmic-ray experiments at high altitudes over a wide range of latitudes, *Physical Review, 76*, 914-932, 1949.

Bütikofer, R., Flückiger, E.O., Smart, D.F., and Shea, M.A., Effects of the magnetosheath on cosmic ray particle propagation in near-earth space, *Proc. 24th Int. Cosmic Ray Conf., Romey, 4*, 1070-1073, 1995.

Bütikofer, R., Flückiger, E.O., Smart, D.F., and Shea, M.A., Effects of the magnetosheath magnetic field on cosmic ray propagation near earth, *Proc. 25th Int. Cosmic Ray Conf., Durban,* 377-380, 1997.

Cane, H.V., Coronal mass ejections and Forbush decreases, *Space Science Reviews, 93*, 79-105, 2000.

Carmichael, H., and Bercovitch, M., V. Analysis of IQSY cosmic-ray survey measurements, *Canadian Journal of Physics, 47*, 2073-2093, 1969a.

Carmichael, H., Bercovitch, M., Steljes, J.F., and Magidin, M., I. Cosmic-ray latitude survey in North America in summer, 1965, *Canadian Journal of Physics, 47*, 2038-2050, 1969b.

Clem, J.M., Atmospheric yield functions and the response to secondary particles of neutron monitors, *Proc. 26th Int. Cosmic Ray Conf., Salt Lake City, 7*, 317-320, 1999.

Clem, J.M., Bieber, J.W., Evenson, P., Hall, D., Humble, J.E., and Duldig, M.L., Contribution of obliquely incident particles to neutron monitor counting rate, *Journal of Geophysical Research, 102*, no A12, 26919-26926, 1997.

Clem, J.M., and Dorman, L.I., Neutron monitor response functions, *Space Science Reviews, 93*, 335-359, 2000.

Compton, A.H., and Turner, R.N., Cosmic rays on the Pacific Ocean, *Physical Review, 52*, 799-814, 1937.

Cooke, D.J., Humble, J.E., Shea, M.A., Smart, D.F., Lund, N., Rasmussen, I.L., Byrnak, B., Goret, P., and Petrou, N., On cosmic ray cut-off terminology, *Il Nuovo Cimento, 14C*, no 3, 213-234, 1991.

Coxell, H., Pomerantz, M.A., and Agarwal, S.P., Survey of cosmic ray intensity in the lower atmosphere, *Journal of Geophysical Research, 71*, no 1, 143-154, 1965.

De Villiers, D., Calibration neutron monitor, 2003.

Dorman, L.I., Cosmic rays, North-Holland Publishing Company, 1974.

Dorman, L.I., Cosmic rays in the earth's atmosphere and underground, Kluwer Academic Publishers, 2004.

Dorman, L.I., Fedchenko, S.G., Granitsky, L.V., and Rishe, G.A., Coupling and barometer coefficients for measurements of cosmic ray variations at altitudes of 260-400 mb, *Proc. 11th Int. Cosmic Ray Conf.,* 233-236, 1969.

Dyring, E., Statistical studies of the performance of cosmic ray recording instruments, *Tellus, 14*, 33-43, 1962.

Egelstaff, P.A., Thermal neutron scattering, Academic Press, 1965.

Evenson, P., Bieber, J.W., Clem, J., and Pyle, R., Neutron monitor temperature coefficients: measurements for BF_3 and ^3He counter tubes, *Proc. 29th Int. Cosmic Ray Conf., Pune,* in press, 2005.

Fisk, L.A., Motion of the footpoints of heliospheric magnetic field lines at the sun: implications for recurrent energetic particle events at high heliographic latitudes, *Journal of Geophysical Research, 101*, no A7, 15547-15553, 1996.

Fisk, L.A., An overview of the transport of galactic and anomalous cosmic rays in the heliosphere: theory, *Advanced Space Reviews, 23*, no 3, 415-423, 1999.

Fisk, L.A., Zurbuchen, T.H., and Schwadron, N.A., On the coronal magnetic field: consequences of large-scale motions, *The Astrophysical Journal, 521*, 868-877, 1999.

Flückiger, E.O., Kobel, E., Smart, D.F., and Shea, M.A., A new concept for the simulation and visualization of cosmic ray particle transport in the earth's magnetosphere, *Proc. 22th Int. Cosmic Ray Conf., Dublin, Ireland, 3*, 648-651, 1991.

Forbush, S.E., World-wide cosmic-ray variations, 1937-1952, *Journal of Geophysical Research, 59*, 525, 1954.

Friedlander, M.W., Cosmic rays, Harvard University Press, 1989.

Friedlander, M.W., A thin cosmic rain, Harvard University Press, 2000.

Fukushima, S., Kodama, M., Makino, T., and Miyazaki, Y., Results of cosmic-ray surveys between Japan and the Antarctic, *Report of the Japanese Antarctic Research Expedition, Antarctic Record, 20*, 1701-1732, 1963.

Gall, R., Jimenez, J., and Orozco, A., Directions of approach of cosmic rays for high latitude stations, *Journal of Geophysical Research, 74*, no 14, 3529-3540, 1969.

Gil, A., Iskra, K., Modzelewska, R., and Alania, M.V., On the 27-day variations of the galactic cosmic ray anisotropy and intensity for different periods of solar magnetic cycle, *Advances in Space Research, 35*, no 4, 687-690, 2005.

Gleeson, L.J., and Axford, W.I., Cosmic rays in the interplanetary medium, *The Astrophysical Journal, 149*, L115-L118, 1967.

Gombosi, T.I., Physics of the space environment, Cambridge University Press, 1998.

Hargreaves, J.K., The solar-terrestrial environment, Cambridge University Press, 1992.

Harman, C.V., and Hatton, C.J., Contributions to the counting rate and the temperature dependence of neutron monitors, *Canadian Journal of Physics, 46*, S1052-1056, 1968.

Harrison, A.W., Intermediate atomic and nuclear physics, Macmillan, 1966.

Hattingh, M., The modulation of galactic cosmic rays in a three-dimensional heliosphere, Ph.D. thesis, Potchefstroom University for CHE, South Africa, 1998.

Hatton, C.J., and Carmichael, H., Experimental investigation of the NM-64 neutron monitor, *Canadian Journal of Physics, 42*, 2443-2472, 1964.

Hatton, C.J., The neutron monitor, *Progress in elementary particle and cosmic-ray physics,* vol X, Ed J.G. Wilson en S.A. Wouthuysen, North Holland Publishing Co., Amsterdam, 1971.

Hayakawa, S., Cosmic ray physics – Nuclear and astrophysical aspects, John Wiley & Sons, 1969.

Hofmann, D.J., and Sauer, H.H., Magnetosperic cosmic-ray cutoffs and their variations, *Space Science Reviews, 8*, 750-803, 1968.

Hughes, E.B., Marsden, P.L. Brooke, M.A., and Wolfendale, A.W., Neutron production by cosmic ray protons in lead, *Proceedings of the Physical Society, 83*, 239-251, 1964.

Humble, J.E., Shea, M.A., and Smart, D.F., Sensitivity of cosmic ray trajectory calculations to geomagnetic field model representations, *Physics of the Earth and Planetary Interiors, 37*, 12-19, 1985.

Iucci, N., Villoresi, G., Dorman, L.I, and Parisi, M., Cosmic ray survey to Antarctica and coupling functions for neutron component near solar minimum (1996-1997), 2. Determination of meteorological effects, *Journal of Geophysical Research, 105*, no A9, 21035-21045, 2000.

Jokipii, J.R., Levy, E.H., and Hubbard, W.B., Effects of particle drift on cosmic-ray transport. I. General properties, application to solar modulation, *The Astrophysical Journal, 213*, 861-868, 1977.

Kallenrode, M.B., Galactic cosmic rays, In: The outer heliosphere: beyond the planets, Editors: Scherer, K., Fichtner, H., and Marsch, E., Katlenburg-Lindau, 2000.

Kent, D.W., Coxell, H., and Pomerantz, M.A., *Canadian Journal of Physics, 46*, 1082-1086, 1968.

Kobel, E., and Flückiger, E.O., A model of the steady state magnetic field in the magnetosheath, *Journal of Geophysical Research, 99*, no A12, 23617-23622, 1994.

Kóta, J., and Jokipii, J.R., Effects of drift on the transport of cosmic rays. VI. A three-dimensional model including diffusion, *The Astrophysical Journal, 265*, 573-581, 1983.

Krane, K.S., Introductory nuclear physics, John Wiley & sons, 1988.

Krüger, H., and Moraal, H., Environmental effects on neutron monitors, *Proc. 29th Int. Cosmic Ray Conf., Pune*, in press, 2005.

Krüger, H., Moraal, H., Bieber, J.W., Clem, J.M., Evenson, P.A., Pyle, K.R., Duldig, M.L., and Humble, J.E., First results of a mobile neutron monitor to intercalibrate the worldwide network, *Proc. 28th Int. Cosmic Ray Conf., Tsukuba, Japan, 7*, 3441-3444, 2003.

Le Couteur, K.J., The evaporation theory of nuclear disintegrations, *Proceedings of the Physical Society, 63*, 259-282, 1949.

Le Roux, J.A., Die toepassing van Stormerteorie vir die berekening van afsnystyfhede van kosmiese strale in die geomagnetiese veld, M.Sc. dissertation, Potchefstroom University for CHE, South Africa, 1986.

Lockwood, J.A., Forbush decreases in the cosmic radiation, *Space Science Reviews, 12*, 658-715, 1971.

Lockwood, J.A., and Debrunner, H., Solar flare particle measurements with neutron monitors, *Space Science Reviews, 88*, 483-500, 1999.

Malan, D, and Moraal, H., The effect of wind on pressure correction of the SANAE neutron monitor counting rate, *South African Journal of Science, 98*, 278-281, 2002.

McCracken, K.G., Rao, U.R., and Shea, M.A., The trajectories of cosmic rays in a high degree simulation of the geomagnetic field, *Massachusetts Institute of Technology, Technical Report*, no 77, 1962.

McDonald, F. B., Integration of neutron monitor data with spacecraft observations: a historical perspective, *Space Science Reviews, 93*, 263-284, 2000.

Merrill, R.T., and McElhinny, M.W., The earth's magnetic field, Academic Press, 1983.

Meyer, P., and Simpson, J.A., Changes in the low-energy particle cutoff and primary spectrum of cosmic radiation, *Physical Review*, *99*, no 5, 1517-1523, 1955.

Miyake, S., and Yanagita, S., Effects of the tilted and wavy current sheet on the solar modulation of galactic cosmic rays, *Proc. 29th Int. Cosmic Ray Conf., Pune*, in press, 2005.

Moraal, H., Cosmic ray modulation studies in the outer heliosphere, *Nuclear Physics B (Proc. Suppl.)*, *33*, 161-178, 1993.

Moraal, H., Belov, A., and Clem, J.M., Design and co-ordination of multi-station international neutron monitor networks, *Space Science Reviews*, *93*, 283-303, 2000.

Moraal, H., Krüger, H., Benadie, A., and De Villiers, D., Calibration of the Sanae and Hermanus neutron monitors, *Proc. 28th Int. Cosmic Ray Conf., Tsukuba, Japan, 7*, 3453-3456, 2003.

Moraal, H., McCracken, K.G., Schoeman, C.C., and Stoker, P.H., The ground level enhancements of 20 January 2005 and 28 October 2003, *Proc. 29th Int. Cosmic Ray Conf., Pune*, in press, 2005.

Moraal, H., Potgieter, M.S., Stoker, P.H., and Van der Walt, A.J., Neutron monitor latitude survey of cosmic ray intensity during the 1986/1987 solar minimum, *Journal of Geophysical Research*, *94*, no A2, 1459-1464, 1989.

Nagashima, K., and Morishita, I., Twenty-two year modulation of cosmic rays associated with reversal of polar magnetic field of the sun, *Planetary and Space Science*, *28*, 195-205, 1980.

Nagashima, K., Sakakibara, S., Murakami, K., and Morishita, I., Response and yield functions of neutron monitor, galactic cosmic-ray spectrum and its solar modulation, derived from all the available world-wide surveys, *Il Nuovo Cimento*, *12C*, no 2, 173-209, 1989.

Neher, H.V., Peterson, V.Z., and Stern, E.A., Fluctuations and latitude effect of cosmic rays at high altitudes and latitudes, *Physical Review*, *90*, no 4, 655-674, 1953.

Owens, A.J., Cosmic-ray scintillations, Ph.D. thesis, California Institute of Technology, Pasadena, California, 1973.

Parker, E.N., The formation of sunspots from the solar toroidal field, *The Astrophysical Journal*, *121*, 491-507, 1955.

Parker, E.N., Dynamics of the interplanetary gas and magnetic fields, *The Astrophysical Journal*, *128*, 664-676, 1958a.

Parker, E.N., Cosmic-ray modulation by solar wind, *Physical Review*, *110*, no 6, 1445-1449,1958b.

Parker, E.N., Sudden expansion of the corona following a large solar flare and the attendant magnetic field and cosmic-ray effects, *The Astrophysical Journal*, *133*, 1014-1033, 1961.

Pomerantz, M.A., Cosmic-ray investigations with a shipboard neutron monitor, *National Geographic Society research reports, 1964 projects*, 171-177, 1969.

Pomerantz, M.A., Cosmic rays, Van Nostrand Reinhold Company, 1971.

Potgieter, M.S., Raubenheimer, B.C., Stoker, P.H., and Van der Walt, A.J., Modulation of cosmic rays during solar minimum. Part 2. Cosmic ray latitude distribution at sea-level during 1976, *South African Journal of Physics*, *3*, no 3-4, 77-89, 1980.

Pyle, K.R., The Haleakala cosmic ray neutron monitor station: intercalibration with the Huancayo station, *Proc. 23th Int. Cosmic Ray Conf., Calgary, 3*, 609-612, 1993.

Pyle, R., Evenson, P., Bieber, J.W., Clem, J.M., Humble, J.E., and Duldig, M.L., The use of ^{3}He tubes in a neutron monitor latitude survey, *Proc. 26th Int. Cosmic Ray Conf., Salt Lake City, 7*, 386-389, 1999.

Rao, U.R., Solar modulation of galactic cosmic radiation, *Space Science Reviews*, *12*, 719-809, 1972.

Rao, U.R., McCracken, K.G., and Venkatesan, D., Asymptotic cones of acceptance and their use in the study of the daily variation of cosmic radiation, *Journal of Geophysical Research*, *68*, no 2, 345-369, 1963.

Raubenheimer, B.C., Flückiger, E., Mischke, C.F.W., and Potgieter, M.S., Comparison between the experimental and theoretical responses of neutron monitors, *South African Journal of Physics*, *3*, no 2, 29-35, 1980.

Raubenheimer, B.C., and Stoker, P.H., Various aspects of the attenuation coefficient of a neutron monitor, *Journal of Geophysical Research*, *79*, no 34, 5069-5076, 1974.

Reinecke, J.P.L., Moraal, H., and McDonald, F.B., The cosmic radiation in the heliosphere at successive solar minima: 2. Steady state no-drift solutions of the transport equation, *Journal of Geophysical Research*, *98*, no A6, 9417-9431, 1993.

Reinecke, J.P.L., Steenberg, C.D., Moraal, H., and McDonald, F.B., An alternative approach to the modelling of galactic cosmic ray intensities in the heliosphere, *Advanced Space Reviews*, *19*, no 6, 901-904, 1997.

Rose, D.C., Fenton, K.B., Katzman, J, and Simpson, J.A., Latitude effect of the cosmic ray nucleon and meson components at sea level from the arctic to the antarctic, *Canadian Journal of Physics*, *34*, 968-984, 1956.

Rossi, B., High-energy particles, Prentice-Hall, 1952.

Ryan, M.R., Lockwood, J.A., and Debrunner, H., Solar energetic particles, *Space Science Reviews*, *93*, 35-53, 2000.

Sandström, A.E., Pomerantz, M.A., and Grönkvist, B., Latitude effect and atmospheric attenuation of the cosmic ray nucleon component, *Tellus*, *14*, 356-362, 1962.

Schlaepfer, H., Cosmic rays, *Spatium*, 3-15, 2003.

Schlickeiser, R., Cosmic ray astrophysics, Springer, 2002.

Shea, M.A., and Smart, D.F., Worldwide trajectory-derived vertical cutoff rigidities and their application to experimental measurements, *Journal of Geophysical Research*, *72*, no 7, 2021-2027, 1967.

Shea, M.A., and Smart, D.F., A world grid of calculated cosmic ray vertical cutoff rigidities for 1980.0, *Proc. 18th Int. Cosmic Ray Conf., Bangalore, 3*, 415-416, 1983.

Shea, M.A., and Smart, D.F., Fifty years of cosmic radiation data, *Space Science Reviews*, *93*, 229-262, 2000.

Shea, M.A., and Smart, D.F., Vertical cutoff rigidities for cosmic ray stations since 1955, *Proc. 27th Int. Cosmic Ray Conf., Hamburg, 10*, 4063-4066, 2001.

Shea, M.A., Smart, D.F., and Gentile, L.C., Vertical cutoff rigidities for selected cosmic ray stations for epoch 1980.0, *Proc. 18th Int. Cosmic Ray Conf., Bangalore, 3*, 411-414, 1983.

Shea, M.A., Smart, D.F., and Gentile, L.C., Recomputed 1980 cosmic ray cutoff rigidities, *Proc. 21th Int. Cosmic Ray Conf., Adelaide, 7*, 1-5, 1990.

Shea, M.A., Smart, D.F., and McCracken, K.G., A study of vertical cutoff rigidities using sixth degree simulations of the geomagnetic field, *Journal of Geophysical Research, 70*, no 17, 4117-4130, 1965.

Shea, M.A., Smart, D.F., Stozhkov, Yu.I., Svirzhevsky, N.S., Svirzhevskaya, A.K., Bazilevskaya, P.N., and Charackchyan, T.N., Cosmic ray latitude surveys in the Atlantic ocean area, *Proc. 20th Int. Cosmic Ray Conf., Moscow,* SH 8.1-4, 201-203, 1987.

Shen, M., Neutron production in lead and energy response of a neutron monitor, *Supplemento al Nuovo Cimento, 6*, no 4, 1177-1224, 1968.

Simpson, J.A., Neutrons produced in the atmosphere by the cosmic radiations, *Physical Review, 83*, no 6, 1175-1188, 1951.

Simpson, J.A., Cosmic-radiation intensity-time variations and their origin. III. The origin of 27-day variations, *Physical Review, 94*, no 2, 426-440, 1954.

Simpson, J.A., The cosmic ray nucleonic component: The invention and scientific uses of the neutron monitor, *Space Science Reviews, 93*, 11-32, 2000.

Smart, D.F., and Shea, M.A., World grid of calculated cosmic ray vertical cutoff rigidities for epoch 1990.0, *Proc. 25th Int. Cosmic Ray Conf.*, 401-404, 1997.

Smart, D.F., Shea, M.A., and Flückiger, E.O., Magnetospheric models and trajectory computations, *Space Science Reviews, 93*, 305-333, 2000.

Smart, D.F., Shea, M.A., and Gall, R., The daily variation of trajectory-derived high-latitude cutoff rigidities in a model magnetosphere, *Journal of Geophysical Research, 74*, no 19, 4731-4738, 1969.

Stoker, P.H., Relativistic solar proton events, *Space Science Reviews, 73*, 327-385, 1994.

Stoker, P.H., Clem, J.M., Bieber, J.W., and Evenson, P., 'Apparent' geomagnetic cutoffs and the cosmic ray anomaly in the Cape Town region, *Proc. 25th Int. Cosmic Ray Conf.*, Durban, 37-39, 1997.

Stoker, P.H., Dorman, L.I., and Clem, J.M., Neutron monitor design improvements, *Space Science Reviews, 93*, 361-380, 2000.

Stoker, P.H., and Moraal, H., Neutron monitor surveys at aircraft altitudes, *Astrophysics and Space Science, 230*, 365-373, 1995.

Stoker, P.H., Van der Walt, A.J., and Potgieter, M.S., Modulation of cosmic rays during solar minimum. Part 1. Cosmic ray intensity survey at sea-level during 1976: experimental details, *South African Journal of Physics, 3*, no 3-4, 73-76, 1980.

Stone, E.C., Cummings, A.C., McDonald, F.B., Heikkila, B.C., Lal, N., and Webber, W.R., Appearance of a third episode of enhanced particle intensities at 94 AU: Voyager 1 in the heliosheath, *Proc. 29th Int. Cosmic Ray Conf., Pune*, in press, 2005.

Tongiorgi, V.A., On the mechanism of production of the neutron component of the cosmic radiation, *Physical Review*, *76*, no 4, 517-526, 1949.

Tsyganenko, N.A., A magnetospheric magnetic field model with a warped tail current sheet, *Planetary Space Science*, *37*, no 1, 5-20, 1989.

Usoskin, I.G., Kovaltson, G.A., Kananen, H., and Tanskanen, P., The world neutron monitor netwerk as a tool for the study of solar neutrons, *Annales Geophysicae*, *15*, 375-386, 1997.

Van der Walt, A.J., and Stoker, P.H., The 1976 cosmic ray latitude distribution at sea level, *Proc. 15th Int. Cosmic Ray Conf., Plovdiv*, *4*, 178-183, 1977.

Villoresi, G., Dorman, L.I., Iucci, N., and Ptitsyna, N.G., Cosmic ray survey to Antarctica and coupling functions for neutron component near solar minimum (1996-1997), 1. Methodology and data quality assurance, *Journal of Geophysical Research*, *105*, no A9, 21025-21034, 2000.

Wilson, J.G., Cosmic rays, Wykeham Publications, 1976.

ACKNOWLEDGEMENTS

- It was a privilege to study under the able supervision of professor Harm Moraal. Apart from the usual effort of doctoral study, I also had to catch up with recent developments in this field of study after some twenty years outside academia. With patience my promoter guided me to do that.
- It was not always easy for a hardworking husband to have a wife busy with studies and research. Paul, thank you for all your love and for this opportunity.
- Thank you very much to our 6 children, Paulus, Pieter, Tjaart, Arina, Hendrik en Schalk-Willem, for all your love and help with household tasks.
- To my parents, Pieter en Arina Stoker: I really appreciate your love and your encouragement for this study.
- I want to thank my family and friends for continuous support.
- In spite of a busy programme, Huegene Venter evaluated the grammar and spelling.
- I am thankful to the School of Physics at the Potchefstroom Campus of the North-West University for this study opportunity, and the use of their facilities.
- Without the financial support by the South African National Antarctic Program (SANAP) this study would not have been possible.
- All the honour and praise belongs to our Heavenly Father that we as human beings may investigate his creation.

H. Krüger

May 2006

DANKBETUIGINGS

- Dit was 'n voorreg om onder professor Harm Moraal se bekwame leiding te kon studeer. Met geduld moes meer as twintig jaar se verroesing afgekrap word om op datum te kom met hierdie voorste navorsingsveld.
- Dit was nie altyd maklik vir 'n hardwerkende man om nog 'n studerende vrou te hê nie. Paul, dankie vir al jou liefde en dat jy my hierdie studie gegun het.
- Baie dankie aan ons 6 kinders, Paulus, Pieter, Tjaart, Arina, Hendrik en Schalk-Willem, vir julle liefde en hulp in die huis, al was van julle met tye ook self baie besig met studies.
- 'n Groot dank gaan aan my ouers, Pieter en Arina Stoker, vir julle liefde en julle aanmoediging vir die studie.
- Dankie vir alle familie en vriende vir julle voortdurende ondersteuning.
- Al was sy self besig, het Huegene Venter tyd gemaak vir keurige taalversorging.
- Ek is dankbaar teenoor die Skool vir Fisika van die Potchefstroom-kampus van die Noordwes-Universiteit, wat die geleentheid gegee het vir hierdie studie, asook die gebruik van hulle fasiliteite.
- Sonder die finansiële ondersteuning van die Suid-Afrikaanse Nasionale Antarktiese Program (SANAP) sou hierdie studie nie moontlik gewees het nie.
- Ons Hemelse Vader kom alle eer en lof toe dat ons as mense sy wonderlike skepping kan verken.

H. Krüger

Mei 2006